LBNL-40429
UC-401

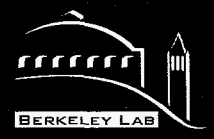

ERNEST ORLANDO LAWRENCE
BERKELEY NATIONAL LABORATORY

Femtosecond Raman Induced Polarization Spectroscopy Studies of Coherent Rotational Dynamics in Molecular Fluids

RECEIVED
JUL 22 1997
OSTI

Michael M. Morgen

Chemical Sciences Division

May 1997
Ph.D. Thesis

MASTER

DISTRIBUTION OF THIS DOCUMENT IS UNLIMITED

DISCLAIMER

This document was prepared as an account of work sponsored by the United States Government. While this document is believed to contain correct information, neither the United States Government nor any agency thereof, nor The Regents of the University of California, nor any of their employees, makes any warranty, express or implied, or assumes any legal responsibility for the accuracy, completeness, or usefulness of any information, apparatus, product, or process disclosed, or represents that its use would not infringe privately owned rights. Reference herein to any specific commercial product, process, or service by its trade name, trademark, manufacturer, or otherwise, does not necessarily constitute or imply its endorsement, recommendation, or favoring by the United States Government or any agency thereof, or The Regents of the University of California. The views and opinions of authors expressed herein do not necessarily state or reflect those of the United States Government or any agency thereof, or The Regents of the University of California.

Ernest Orlando Lawrence Berkeley National Laboratory
is an equal opportunity employer.

LBNL-40429
UC-401

Femtosecond Raman Induced Polarization Spectroscopy Studies of Coherent Rotational Dynamics in Molecular Fluids

Michael Mark Morgen
Ph.D. Thesis

Department of Chemistry
University of California, Berkeley

and

Chemical Sciences Division
Ernest Orlando Lawrence Berkeley National Laboratory
University of California
Berkeley, CA 94720

May 1997

This work was supported by the Director, Office of Energy Research, Office of Basic Energy Sciences, Chemical Sciences Division, of the U.S. Department of Energy under Contract No. DE-AC03-76SF00098.

DISTRIBUTION OF THIS DOCUMENT IS UNLIMITED

Recycled Paper

DISCLAIMER

Portions of this document may be illegible in electronic image products. Images are produced from the best available original document.

Femtosecond Raman Induced Polarization Spectroscopy Studies of Coherent Rotational Dynamics in Molecular Fluids

by

Michael Mark Morgen

B.S. (University of California, Santa Barbara) 1991

A dissertation submitted in partial satisfaction of the

requirements for the degree of

Doctor of Philosophy

in

Chemistry

in the

GRADUATE DIVISION

of the

UNIVERSITY OF CALIFORNIA, BERKELEY

Committee in charge:

Professor Yongqin Chen
Professor Herbert L. Strauss
Professor Kenneth T. Gustafson

Spring 1997

Femtosecond Raman Induced Polarization Spectroscopy Studies of Coherent Rotational Dynamics in Molecular Fluids

Copyright © 1997

by

Michael M. Morgen

The Government reserves for itself and others acting on its behalf a royalty free, nonexclusive, irrevocable, world-wide license for governmental purposes to publish, distribute, translate, duplicate, exhibit, and perform any such data copyrighted by the contractor.

The U.S. Department of Energy has the right to use this document for any purpose whatsoever including the right to reproduce all or any part thereof

Abstract

Femtosecond Raman Induced Polarization Spectroscopy Studies of Coherent Rotational Dynamics in Molecular Fluids

by

Michael Mark Morgen

Doctor of Philosophy in Chemistry

University of California, Berkeley

Professor Yongqin Chen, Chair

We develop a polarization-sensitive femtosecond pump probe technique, Raman induced polarization spectroscopy (RIPS), to study coherent rotation in molecular fluids. By observing the collisional dephasing of the coherently prepared rotational states, we are able to extract information concerning the effects of molecular interactions on the rotational motion. The technique is quite sensitive because of the zero background detection method, and is also versitile due to its nonresonant nature. The RIPS technique and the apparatus used to perform the experiments is described in the second chapter of this dissertation.

In Chapter 3 the RIPS molecular response is derived from basic nonlinear optics principles in the perturbation limit. A tensor analysis, based on an angular momentrum formalism, demonstrates how the observable is related both to the molecular properties, as well as to the experimental configuration and parameters. The relation of the RIPS technique to other time and frequency domain experiments is also discussed. From the general theory, expressions for the response of symmetric and asymmetric tops are obtained and compared to experiments for low pressure O_2, N_2 and CO_2 gases.

The last chapter presents experimental and simulated results for high pressure CO_2 gas and liquid. The data suggest that the rate of rotational energy changing collisions and the rate of reorienting collisions can both be measured independently in the experiments.

The energy changing collisions are found to occur significantly more often than the reorienting interactions. Two simple models are used to attempt to simulate the reorientational motion--a damped free rotor model and Gordon's J diffusion model. The former fits the low pressure gas data well, while the latter is more appropriate at liquid densities. In the high pressure gas neither model accurately describes the rotational dynamics, however, the experimental data at these intermediate densities contain a number of characteristic features that provide a stringent test for alternate models for the reorientational motion.

To my mother

Dorothy Maxine Morgen

Table of Contents

Acknowledgments

It is with great relief and a little disappointment that I write this thesis, which concludes my work at Berkeley. When I began my graduate career here almost six years ago, I had hopes of making many revolutionary scientific discoveries. I now leave a sadder and a wiser man, as the research project I undertook turned out to be a great deal more challenging than I had first imagined. Although my research results are more modest than what I had hoped to achieve, I nevertheless learned much more during my stay than I ever thought possible. I obtained not only an extensive knowledge of science, but also learned a lot about lasers, optics, machining, circuit design, computer programming, and the ubiquitous power of the Fourier transform.

I need to thank a large number of people for helping me complete my degree. First and foremost I would like to thank my advisor Professor Yong Chen, who allowed me to work on a new and exciting research project in his group. Yong taught me a great many things about lasers and about physical chemistry in general. Over the years we had many stimulating scientific discussions, which usually inspired me to throw myself back into my project with renewed enthusiasm and dedication. His insight and encouragement was a valuable resource to me whenever I became stuck on a problem.

I am also deeply indebted to my coworkers in the group, Lukas Hunziker, Pete Ludowise, Matt Blackwell, and Bill Price. I was lucky to have the chance to work with such an outstanding group of people. Not only was their collaboration vital for completion of this work, but their comradeship kept my spirits up through many difficult times. I especially need to acknowledge Bill, who worked closely with me for two years on this project. He did many of the initial high pressure experiments and designed the high pressure sample cell. I won't soon forget our marathon late night (beer in the beam!) scanning sessions. I thank Pete for spending many hours helping me try to get the dye laser working, and also for getting married so that we could have a great bachelor party in

Capitola. If Luke had not generously allowed me to use his Ti:sapphire laser and shown me how to use it, I still wouldn't have any decent high pressure data. I must thank Matt for patiently answering my naive computer software and programming questions.

I have found the chemistry department at Berkeley to be a stimulating and interesting environment in which to study science. I have been inspired by several of Professor Alex Pines' wonderful seminars, and amused and bewildered by Professor Bob Harris' lectures on quantum mechanics. I am grateful to Professor Herb Strauss and Professor David Chandler for enlightening discussions on Raman scattering and correlation functions, respectively.

I'd like to thank the guys in Bona Fido, Ryan (half staff) Powers, Chris Tagge, and Mark (that's with an "a") Aubart for providing a much needed outlet for stress relief. Not every chemist gets to play in a great rock and roll band. I especially thank Ryan and Chris for being great roommates.

The support of my parents and brother has been very important to me during the course of my graduate years. I especially thank my parents for encouraging my education all these years. In addition, their financial support through college allowed me the opportunity to excel academically and to get into Berkeley for graduate school.

Finally, and most importantly, I would like to thank Cheryl Longfellow for her unwavering love and support throughout these difficult several years. Her companionship has given me the determination to overcome the many hardships of graduate school and has made the effort worth while.

Chapter 1

Introduction

Several types of rotational coherent spectroscopy (RCS) have been developed in the last ten or twelve years.[1-10] RCS techniques are picosecond or femtosecond time domain methods that have proven useful in obtaining structural, and more recently, dynamical information of molecular gases. In an RCS experiment a short, polarized laser pulse is used to coherently excite gas-phase molecules into rotational superposition states in either the ground or an excited vibronic manifold. The excitation results in a quantum beat, which has a frequency that depends on the energy differences of the rotational levels involved in the superposition state. The excitation pulse usually has a sufficient bandwidth to transfer molecules from the entire rotational manifold into such coherent states. The beats of the various superposition states that are formed interfere with one another, causing the gas to exhibit quasi-periodic alignment transients whose positions in time depend upon the rotational constants of the molecule. These transients are then observed using a coherent[10,11] or incoherent[1,3,4,6] time resolved detection scheme.

Because the positions of the transients in an RCS experiment depend upon the rotational constants of the molecule, these techniques have been used extensively to help deduce the structure of gas-phase species.[1-9] Many experiments have focused on large organic molecules in supersonic beams.[2-7] However, since the coherent rotational states prepared in an RCS experiment experience a dephasing due to various intra- and intermolecular processes, one can also obtain information about the molecular interactions by observing changes in the alignment transients over time. For example, Harde and Grischkowsky excited N_2O vapor with terahertz radiation and monitored the free-induction

decay.[10] In addition to obtaining the spectroscopic constants, they were able to measure the coherent relaxation time.

In our laboratory we have developed a new variant of the femtosecond RCS techniques, which we term Raman induced polarization spectroscopy (RIPS).[12,13] The experimental technique is analogous to that pioneered by Heritage et. al. in the 1970s, and subsequently used by others for time resolved coherent polarization studies,[14-16] such as Raman induced Kerr effect spectroscopy (RIKES). In RIPS a linearly polarized pump pulse prepares coherent rotational superposition states in the ground vibronic manifold via a nonresonant stimulated Raman interaction (Fig. 1). The alignment of the molecules is then probed with a second, delayed femtosecond pulse using a coherent polarization technique.

Experimental results for O_2, N_2, CO_2 and O_3 at low pressures[12] demonstrate that RIPS can be used for precise measurement of spectroscopic constants in molecular gases. Also, since the initial rotational state distribution in the gas affects the shape of the recurrence transients, one can use the technique to measure the temperature of a gas. Preliminary experiments towards this application have been done in our laboratory. In the following chapters, however, we will focus on our work in using RIPS to understand how collisions affect molecular motion and orientation. We are especially interested in how the reorientational motion depends on density. Accordingly, we have obtained RIPS spectra for CO_2 over a very wide density range, from the low pressure gas to the liquid state. The well-characterized evolution of the experimental spectrum as the density is increased provides a rigorous test of models for the rotational motion.

There are, of course, various other spectroscopic techniques that also offer insight into molecular rotational dynamics. For example, collision cross sections can often be obtained from spin rotation relaxation times in NMR experiments.[17,18] Frequency domain techniques such as absorption,[19,20] Raman and Rayleigh spectroscopy[18,21-24] can also provide information about collisions. We should point out that RIPS offers several advantages over some of these other techniques. First, RIPS is quite versatile because it is

a nonresonant technique that can be used to study any non isotropic molecule. RIPS also offers very high sensitivity due to the nature of the essentially zero background polarization detection method employed in the experiments. Additionally, as a femtosecond spectroscopy method, RIPS is ideally suited to observing the molecular dynamics of fluids at mid to high densities directly in real time, where the molecular motions occur on the time scale of hundreds of femtoseconds to several picoseconds. Such dynamics lead to sharp, well defined peaks in time domain spectra. Conversely, it can be more difficult to extract these dynamics from analogous frequency domain experiments, since in the frequency domain the dynamics manifest themselves in a very broad, low intensity signal that cannot be easily distinguished from the background or baseline.

This work is organized as follows. Chapter 2 describes the experimental apparatus and techniques used to obtain the data. Chapter 3 provides a theoretical foundation for the RIPS technique, which is used to generate simulated spectra that are then compared to experimental data for several di- and triatomic gases at low (<1 atm) pressure. Chapter 4 discusses theoretical and experimental results for high pressure CO_2 gas and liquid. Computer programs used to create the simulated spectra are given in the appendix.

References

1. P.M. Felker, J. Chem. Phys. **96**, 7844 (1992).

2. L.L. Connell, T.C. Corcoran, P.W. Joireman, and P.M. Felker, Chem. Phys. Lett. **166**, 510 (1990).

3. L.L. Connell, T.C. Corcoran, P.W. Joireman, and P.M. Felker, J. Chem. Phys. **94**, 1229 (1990).

4. N.F. Scherer, L.R. Khundkar, T.S. Rose, and A.H. Zewail, J. Phys. Chem. **91**, 6478 (1987).

5. P.W. Joireman, L.L. Connell, S.M. Ohline, and P.M. Felker, J. Chem. Phys. **96**, 4118 (1992).

6. P.M. Felker, J.S. Baskin, and A.H. Zewail, J. Phys. Chem. **90**, 724 (1986).

7. T.C. Corcoran, L.L. Connell, G.V. Hartland, P.W. Joireman, R.A. Hertz, and P.M. Felker, Chem. Phys. Lett. **170**, 139 (1990).

8. J.F. Kauffman, M.J. Côté, P.G. Smith, and J.D. McDonald, J. Chem. Phys. **90**, 2874 (1989).

9. S.M. Ohline, P.W. Joireman, L.L. Connell, and P.M. Felker, Chem. Phys. Lett. **191**, 362 (1992).

10. H. Harde and D. Grischkowsky, J. Opt. Soc. Am. B **8**, 1642 (1991).

11. A.B. Myers and R.M. Hochstrasser, J. Chem. Phys. **85**, 6301 (1986).

12. M.M. Morgen, W.D. Price, L.E. Hunziker, P.D. Ludowise, M. Blackwell, and Y. Chen, Chem. Phys. Lett. **209**, 1 (1993).

13. M.M. Morgen, W.D. Price, P.D. Ludowise, and Y. Chen, J. Chem. Phys. **102**, 8780 (1995).

14. E.P. Ippen and C.V. Shank, Appl. Phys. Letters **26**, 92 (1975).

15. D. Waldeck, A.J. Cross, Jr., D.B. McDonald, and G.R. Fleming, J. Chem. Phys. **74**, 3381 (1981).

16. C. Kalpouzos, W.T. Lotshaw, D. McMorrow, and G.A. Kenney-Wallace, J. Phys. Chem. **91**, 2028 (1987); D.M. Morrow, W.T. Lotshaw, and G.A. Kenney-Wallace, IEEE J. Quantum Electron. **QE-24**, 443 (1988).

17. C.J. Jameson, A.K. Jameson, and K. Jackowski, J. Chem. Phys. **86**, 2717 (1987).

18. W.B. Neilsen and R.G. Gordon, J. Chem. Phys. **58**, 4131 (1973).

19. P.W. Anderson, Phys. Rev. **76**, 647 (1949).

20. see H. Van Houten, L.J.F. Hermans and J.J.M. Beenakker, Physica A **131**, 64 (1985), and references therein.

21. K.S. Jammu, G.E. St. John, and H.L. Welsh, Can. J. Phys. **44**, 797 (1966).

22. V.G. Cooper, A.D. May, E.H. Hara, and H.F.P. Knaap, Phys. Lett. **27A**, 52 (1968).

23. H. Versmold, Mol. Phys. **43**, 383 (1980).

24. J.P. Boquillon, SPIE *Pulsed Single Freq. Lasers: Technology and Applications* **912**, 160 (1988).

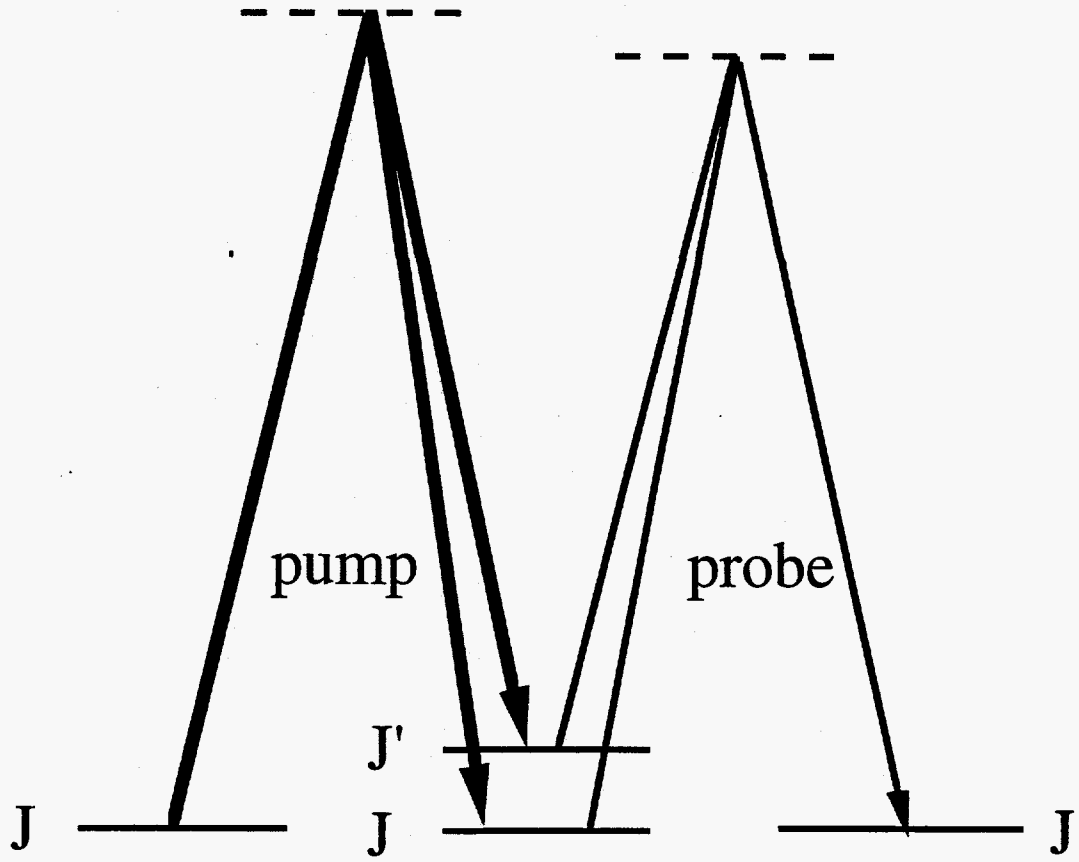

Fig. 1.1. Energy level diagram for the RIPS process. The femtosecond pump laser pulse creates coherent rotational states between J and J' via a nonresonant stimulated Raman process. The coherent states are then probed by a delayed femtosecond probe laser during a second nonresonant stimulated Raman interaction.

Chapter 2
Experimental Apparatus

The experiments reported here were performed using two different home-built femtosecond laser systems. The low pressure (<1 atm) experiments on O_2, CO_2, N_2, and O_3 were done using an amplified colliding pulse mode locked (CPM) ring dye laser. The high pressure CO_2 data was taken using a Ti:sapphire laser system built by Lukas Hunziker. The first section of this chapter describes in some detail the low pressure experimental apparatus, while the second section deals with the high pressure experiments. Only the basic operating characteristics of the Ti:sapphire system will be given here. For a more complete discussion of the system, refer to Lukas Hunziker's Ph.D. thesis.

2.1 Low Pressure Experiments

A schematic of the amplified CPM dye amplifier system used for the low pressure experiments is shown in Fig. 2.1. It consisted of a CPM oscillator, pulsed dye amplifier, optics for generation of pump and probe (including a variable delay line for the pump), sample interaction region, and a detection apparatus.

2.11 CPM Oscillator

The CPM oscillator was built after the seven mirror design of Valdmanis et. al.[1] Gain was provided by a jet of Rhodamine 6G in ethylene glycol pumped by 4-5 W from a multiline argon ion laser (Coherent 310 Series). A jet of diethyloxadicarbocyanine iodide (DODCI) in ethylene glycol was used as the absorber. Four intracavity prisms compensated for group velocity dispersion. The oscillator had two output beams of 20 mW at 100 MHz, centered at 620 nm. The typical pulse duration was 50 fs (FWHM

measured by second harmonic generation on a Potassium Dihydrogen Phosphate (KDP) crystal). One output beam was split and used to obtain the pulse autocorrelation and to trigger a Nd:YAG laser for pulse amplification. The second output beam was sent to a five stage pulsed dye amplifier.

2.12 Pulsed Dye Amplifier (PDA)

The PDA (Fig. 2.2) utilized Bethune type cells[2] transversely pumped by the 532 nm second harmonic of a Nd:YAG laser (Spectra Physics GCR-4) operated at 30 Hz in the short pulse mode (2.5 ns). The cells had orifice diameters of 1, 3, 3, 6, 6 mm and lengths of 2, 3, 3, 6, 6 cm, respectively. The face of each cell was 3 cm high. Kiton Red in a mixture of 10% Ammonyx LO® and 90% water was used as the gain medium in the first stage. The last four stages used Sulforhodamine 640 in methanol at concentrations on the order of 10^{-4} M. Concentrations were adjusted to maximize amplification without creating a large amount of amplified stimulated emission (ASE).

Various beamsplitters were used to reflect portions of the Nd:YAG beam to the Bethune cells. The pump beam was focused into each cell using a plano-concave lens in conjunction with a cylindrical lens (both from Melles Griot), creating an elliptically shaped beam that fully illuminated the face of each cell. Pump energies for the five stages were 8, 8, 11, 20, and 70 mJ per pulse, respectively. The pulses were correspondingly amplified by factors of 200, 80, 12, 5, and 2, for an overall gain of 2×10^6.

Several steps were taken to minimize ASE in the amplifier. First, the femtosecond pulses were focused through apertures after stages one (homemade, 200 μm stainless steel) and three (Bird Precision Jewels, 50 μm sapphire) using a Galilean telescope. The first telescope consisted of a 15 cm focal length glass focusing lens (Newport) and a 30 cm focal length collimating lens. The second used a 6.79 focal length focusing lens and a 12.5 cm focal length collimating lens (both from Newport). Aside from eliminating ASE the

telescopes served to expand the beam diameter to fill the successively larger cell apertures at stages two and four.

An adjustable iris was used to control the YAG pump beam intensity for the second cell in order to reduce ASE from this stage. ASE from the first two stages was further reduced by focusing the pulses after stage two onto a 1 mm thick colored glass filter (Schott RG630) used as a saturable absorber. Finally, the pump power into the last two amplifier stages could be adjusted by use of a half wave plate (CVI Laser Corp.), since the percentage of the beam reflected by the beamsplitters was polarization dependent. The ASE from the last two cells was therefore reduced by optimizing the pump power into these stages. In the end ASE was usually limited to 5% of the energy of the final amplified pulses.

After the second cell the femtosecond pulses were retroreflected through a pair of glass prisms (Esco Products Inc.) to compensate for group velocity dispersion in the first two stages. The pulse width at this point was 50 fs. A second set of prisms was used for compression after the last amplifier stage, giving 80 fs pulses with a 10 nm (FWHM) bandwidth centered between 623 and 630 nm. The final amplified pulses had energies of 400-500 μJ per pulse.

2.13 Generation of Pump and Probe

Approximately 70% of the amplified beam was split off and used as the pump beam, which was spatially filtered and collimated by focusing through a 400 μm stainless steel aperture. The pump beam was then sent through a variable optical delay line provided by a microcontrolled translation stage (Aerotech #50SMB2-HM). The remaining 30% of the beam was used to create white light by focusing it just outside of a $\approx$1 mm thick jet of ethylene glycol using a 38.1 mm focal length glass lens (Newport). The plane of the jet was set at an angle of approximately 45° to the direction of beam propagation. For best

results the flow of the jet was adjusted so that its two surfaces were parallel at the point of beam intersection, as evidenced by a clean diffraction pattern of concentric circles formed by the beam reflections off these surfaces. The white light was recollimated using a 10 cm focal length glass lens and sent through an interference filter (Edmund Scientific) to create a probe beam centered at 670 nm and having a pulse width of 150-200 fs.

2.14 Sample Interaction and Polarization Detection

The polarization of the probe beam was established by passing it through a Glan-Thompson polarizer (Karl-Lambrecht Co.) oriented at 45° with respect to the pump polarization. The pump and probe were sent through the sample cell at a small relative angle ($\approx 1°$) in order to avoid spatial overlap of the beams on the cell windows (Fig. 2.3). After the cell the pump beam was blocked with an iris, while the probe beam was sent through a second Glan-Thompson polarizer, aligned perpendicularly to the first one. The two polarizers were a matched pair with a measured extinction ratio of 10^{-7}.

A wave plate designed and built by Bill Price was used to minimize the leakage of the probe beam through the second polarizer by compensating for the birefringence of the optics between the polarizers. This "compensator" could be used to introduce birefringence of adjustable magnitude and sign. It consisted of a 1" square piece of fused silica cut from a cell window and mounted in a rotatable square aluminum housing. Two micrometer screws mounted along adjacent sides of the housing pushed springs against Teflon seats that applied pressure to either of two edges of the silica window. The magnitude of the induced birefringence was determined by the amount of pressure applied on the window in either the x or y direction (beam propagation through the window was in the z direction) and by the amount of rotation of the window around the z axis from the minimum birefringence position. The sign of the birefringence was controlled by the direction of rotation of the window from the minimum birefringence position. By inserting the

compensator into the probe beam path just before the second polarizer, the spurious birefringent probe leakage could be drastically reduced.

The signal passing through the second polarizer was sent through a long pass filter (Corning 2-64), dispersed by a monochromator (Mcpherson #218), and detected by a photomultiplier tube (PMT, Hamamatsu R1477) wired for short pulse detection (see schematic diagram Fig. 2.4). Since frequency resolution was not required, the monochromator was unnecessary, but provided a convenient mounting location for the PMT. The PMT output consisted of a 15 ns pulse, which was sent through a preamplifier (schematic Fig. 2.5), collected by a gated integrator (Stanford Research #SR250) and digitized shot to shot using a 386 PC computer. Pump and probe powers were monitored by photodiodes using back reflections from optics. These signals were also integrated and stored by computer. Typically, 30 shots were averaged at each pump-probe delay, which was stepped at 15-20 fs intervals.

The compensator was used during the experiment to obtain an optically heterodyned signal. The compensator was first rotated away from the minimum leakage position such that the birefringent leakage was equal to about 25% of the maximum homodyne signal of interest. Several scans were taken in this position. The compensator was then rotated in the opposite direction to get leakage of the same magnitude but opposite sign, and the scans repeated. The two sets of scans were then subtracted to obtain the pure heterodyne spectrum.

2.15 Low Pressure Sample Cell

For low pressure experiments the sample cell consisted of a glass tube 1.5 m long and 2.5 cm in diameter having several inlets (Fig. 2.6). One inlet was used to fill the cell from a gas cylinder, another to evacuate the cell via a mechanical pump, and a third was fitted with a gauge for measuring the pressure. Flat fused silica windows 3.75 cm in

diameter and 9.53 mm thick (Esco Products Inc.) capped the ends of the cell. The partial vacuum inside the cell sealed the windows against o-rings on the ends of the tube. Fixing the windows to the cell by any mechanical means was avoided, as it created stress on the windows, leading to a large birefringent leakage of the probe field through the analyzing polarizer.

2.2 High Pressure Experiments

2.21 Ti:sapphire Oscillator and Regenerative Amplifier

The oscillator, built after the design of Murnane and coworkers,[3] was pumped with 4-5 W from a multiline argon ion laser (Coherent 310 series). Typical output was 300 mW at about 80 MHz. The 30 fs pulses were centered between 780 and 800 nm.

Seed pulses from the oscillator were stretched with a grating, amplified at 3.3 KHz during 10-15 passes through a Nd:YAG pumped Ti:sapphire crystal, then recompressed using the same grating. The resulting 50 fs pulses were centered near 800 nm and contained 330 μJ per pulse.

2.22 Generation of Pump and Probe

Two types of experiments were done, single color and two color. For the single color experiments, the amplified Ti:sapphire fundamental was split and used for the pump and probe beams. The two color experiments were done using a portion of the fundamental for the pump and frequency doubling the remainder of the beam for use as the probe.

A. Single Color Experiments

A beamsplitter (Melles Griot #03BTF013) was used to divide the amplified Ti:sapphire fundamental into two. The transmitted portion, 82.5%, was attenuated by taking the reflection off the front surface of a glass prism ($\approx$5%) and used as the probe beam. The remaining 17.5% was sent to a translation stage (Aerotech #50SMB2-HM), attenuated by a factor of 200 with neutral density filters (Melles Griot), and used for the pump. Typical cross correlations, found using the Kerr effect on a 1 mm thick microscope slide, were 75-100 fs.

B. Two Color Experiments

The Ti:sapphire fundamental was split as above. The transmitted portion was attenuated by a factor of 100 and used as the pump. The reflected beam was frequency doubled to 400 nm using a heated (30-40° C) 0.5 mm thick BBO crystal for type I second harmonic generation. The doubling efficiency was approximately 30%. This beam was sent to the translation stage, attenuated by about a factor of 200, and used as the probe. Since the UV beam was particularly susceptible to group velocity dispersion upon traveling through neutral density filters, part of the probe attenuation was accomplished by reflecting the beam off the front surface of a quartz wedge (16% reflection). Cross correlations obtained with the Kerr effect as above were $\approx$200 fs.

2.23 Interaction and Detection Regions (One and Two Color)

The polarization detection scheme was similar to that employed in the low pressure experiments. In particular, the compensator and a similar pair of matched polarizers were used. Since the high pressure cell was much shorter than that used at low pressures, the beams had to be focused in order to have them separated at the entrance and exit windows.

The pump beam was focused at the center of the sample cell using a 25 cm focal length glass lens (Newport). Longer focal length lenses generated white light on the cell

windows. Even with a shorter focus the beam had to be attenuated as described above to avoid generating white light either on the windows or in the sample. In addition, for the one color experiments lower pump powers were used in order to minimize the amount of pump light scattered from the cell windows and other optics into the detector. Great care had to be taken in this regard, since there was no way to spectrally filter the pump beam from the signal. Higher pump powers could be used for the two color experiments, since the PMTs used in these experiments were not sensitive to the 800 nm fundamental.

The probe pulse was focused at the same point as the pump using a 50 cm focal length glass lens (Newport) placed just before the first polarizer. This relatively long focal length was used so that the probe was essentially collimated as it passed through the polarizers. Shorter focusing and recollimation could have been done between the polarizers, but this was found to create excessive birefringent leakage of the probe. The signal transmitted through the second polarizer was partially recollimated with a lens before it was sent to a PMT wired as above (one color-Hamamatsu R1477, two color-Hamamatsu 1P28).

The laser power was monitored during the experiment by sending the reflection of the probe off the front surface of the analyzing polarizer to a second PMT (one color-R636, two color-Hamamatsu 1P28). The outputs from the PMTs were amplified, digitized, and stored as in the low pressure experiments. Generally, 1500-1800 shots were averaged at each pump-probe delay.

2.24 High Pressure Sample Cell

The original sample cell used for pressures greater than one atmosphere was a stainless steel tube 25 cm long and 2.5 cm in diameter. This cell was abandoned, however, due to problems associated with its excessive size. At pressures greater than about 300 psi, the large volume of the cell allowed large scale density fluctuations in the sample, which

persisted for several hours after filling or moving the cell. These fluctuations destroyed the polarization of the probe pulse, thus preventing detection of the experimental signal while they were present. Even after equilibrium was finally established, the sample bent the beam downward, apparently due to a gravity-induced vertical density gradient. Additionally, the long optical path length through the cell at sample pressures greater than 100-200 psi caused significant broadening of the pump and probe laser pulses.

A shorter cell, designed by Bill Price and built in the Chemistry Department Machine Shop, avoided these problems. This cell was a 2.5" stainless steel cube containing a central cavity (Figs. 2.7 and 2.8). Holes on the top and bottom were threaded for attachment of a pressure gauge and a valve used for filling the cell. The remaining four sides of the cube had holes bored for windows. Two opposing sides were bored deeper than the other two, so that the cell had two different path lengths of 1 cm and 3.375 cm, respectively.

The windows were held onto the cell by flanges secured to the cube by 1/4" 20 bolts (Fig. 2.9). As in the low pressure experiments, it was important that the pressure on the windows was isotropically distributed to avoid induced birefringence. Therefore, the cell was designed so that the flanges did not press against the windows to seal the cell from the outside. Rather the holes were bored to a depth that allowed clearance of the windows from the flanges. The initially loose windows were then sealed *from the inside* against o-rings on the flanges when the cell was filled with fluid.

For experiments involving liquid CO_2, the cell had to be filled to about 1000 psi. Timoshenko and Lessel's formula[4,5] was used to determine the window thickness required to withstand this pressure:

$$T = r\sqrt{\frac{3P(3+\mu)}{8s}}, \qquad (2.1)$$

where T is the thickness of the window needed, r is the radius of the open aperture covered by the window (0.5"), P is the maximum pressure, μ is Poisson's Ratio for fused silica (0.17)[6] and s is the bending strength of fused silica (6.7×10^7 N/m^2).[6] According to this formula the 0.635 cm thick window (ESCO Products, Inc.) used in the experiment had a safely factor of 1.4 at 1000 psi. The window thickness was kept to a minimum in order to avoid group velocity dispersion of the pulse in the window.

2.25 High Pressure Manifold

A manifold (Fig. 2.10) was built in order to allow filling of the stainless steel cell to pressures up to 1000 psi. The manifold consisted of 1/4" stainless steel tubing connected to a 300 c.c. stainless steel cylinder (Whitey), with several lines available for inputting gas or evacuating the system. Each line terminated in a valve that could be closed when the line was not in use. The stainless steel sample cell was attached to the manifold via a Swagelok® connection.

Before filling the cell, both the cell and manifold were purged of air. This was accomplished by filling the system with the sample gas of interest from a cylinder, then partially evacuating the system by briefly opening a line to a mechanical pump. During this evacuation, enough pressure was left in the system so that the cell windows maintained their seal. The filling and evacuation procedure was repeated approximately thirty times to assure the system was free of air. A typical mass spectrum of the cell contents after this procedure showed that the concentration of air was <0.2%.

After removal of air from the system, gas from a large external cylinder was condensed in the manifold's small sample cylinder by immersing the latter in a dewar of liquid nitrogen. A drying tube and hydrocarbon trap (both from Supelco Inc.) were used at the input to remove impurities from the sample gas as it entered the manifold. The valve to the external cylinder was then closed and the sample cylinder allowed to warm until the cell

was filled to the desired pressure. The sample cell valve was closed and the cell removed from the manifold.

The excess gas in the manifold was either vented upon removal of the cell, or else recondensed and sealed in the sample cylinder for later use before removing the cell. It should be noted that the cylinder valve was fitted with a rupture disk (Whitey, burst pressure 3000 psi) to avoid an explosion of the cylinder at 5000 psi in the event too much condensed gas was allowed to warm. This turned out to be a wise precaution, as several rupture discs were blown out during the course of this research.

References

1. J. A. Valdmanis, R. L. Fork, and J. P. Gordon, Opt. Lett. **10**, 135 (1985).

2. D. S. Bethune, Appl. Opt. **20**, 1897 (1981).

3. M. T. Asaki, C. P. Huang, D. Garvey, J. P. Zhou, H. C. Kapteyn, and M. M. Murnane, Opt. Lett. **18**, 977 (1993).

4. E. N. Ganic and T. G. Hicks, *The McGraw-Hill Handbook of Essential Engineering Information and Data*, (McGraw Hill, Inc, New York, 1991), p. 6.15.

5. K. Siemon, *Manual for the Design of Ferrous and Non-Ferous Pressure Vessels and Tanks*, (Distributed by Edwards Brothers, Inc., Ann Arbor, Michigan, 1958), p. 54.

6. *Optical Materials and Components Handbook*, (ESCO Products, Inc.).

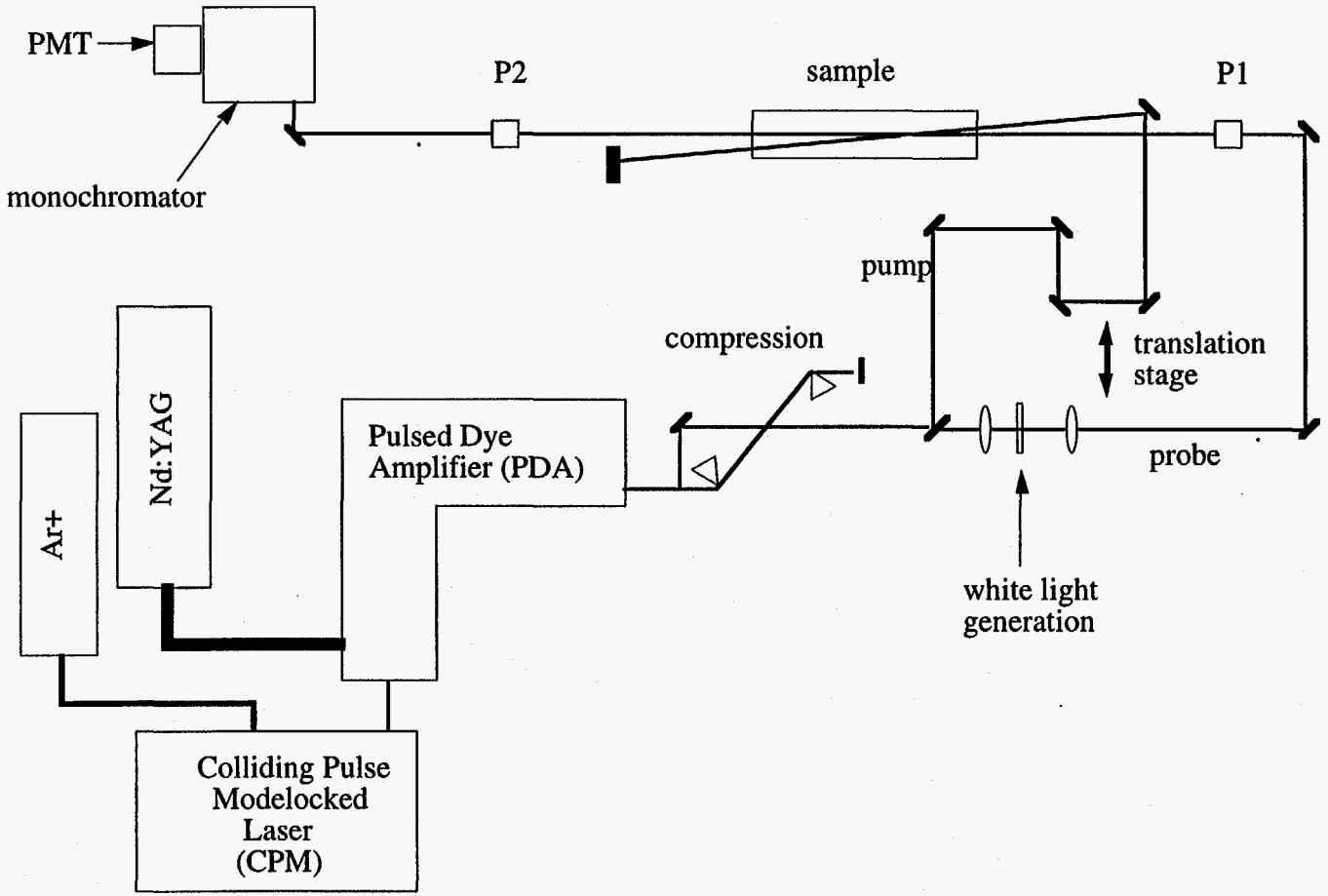

Fig. 2.1. Amplified CPM Femtosecond Laser System

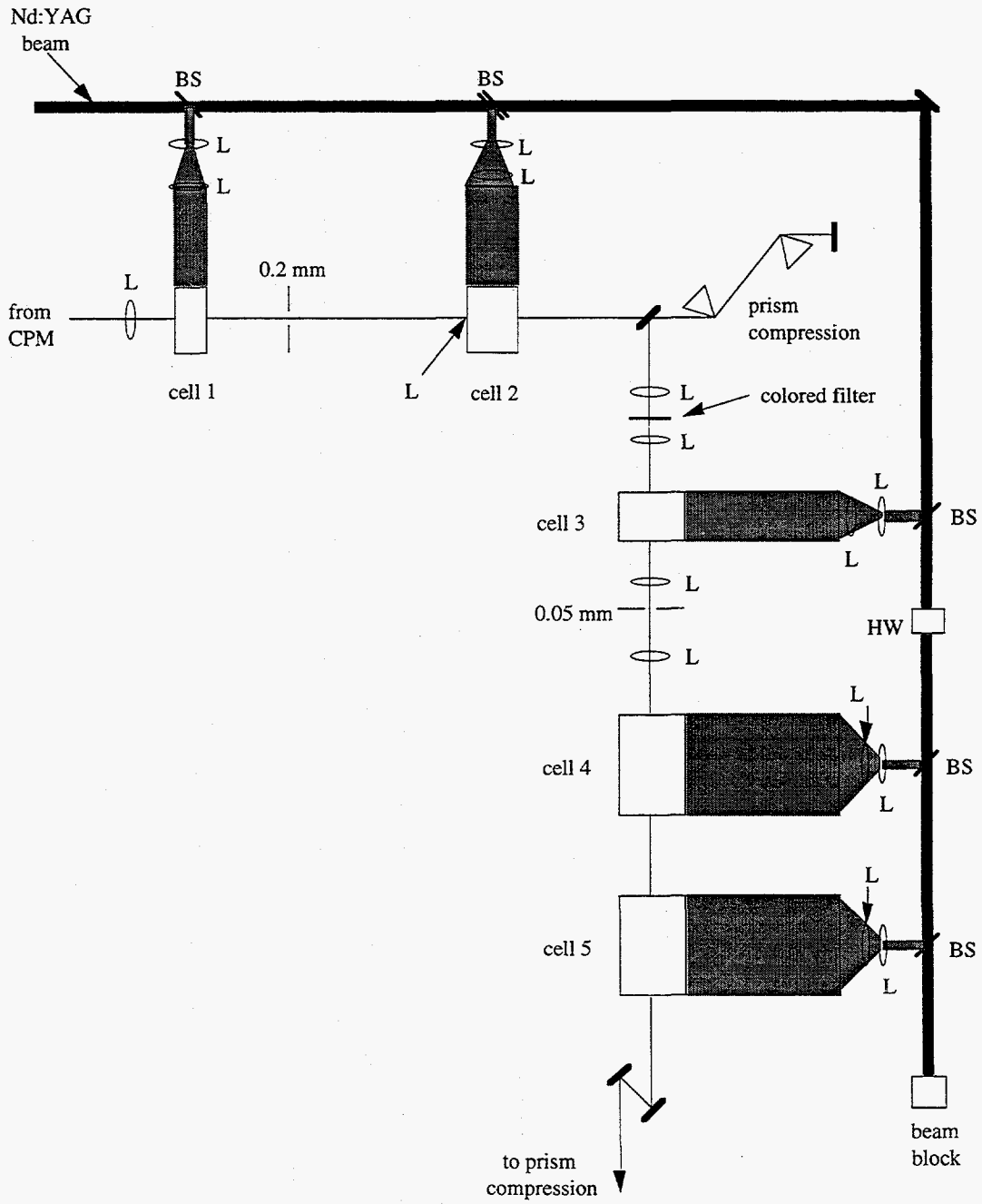

Fig. 2.2. Pulsed dye amplifier.

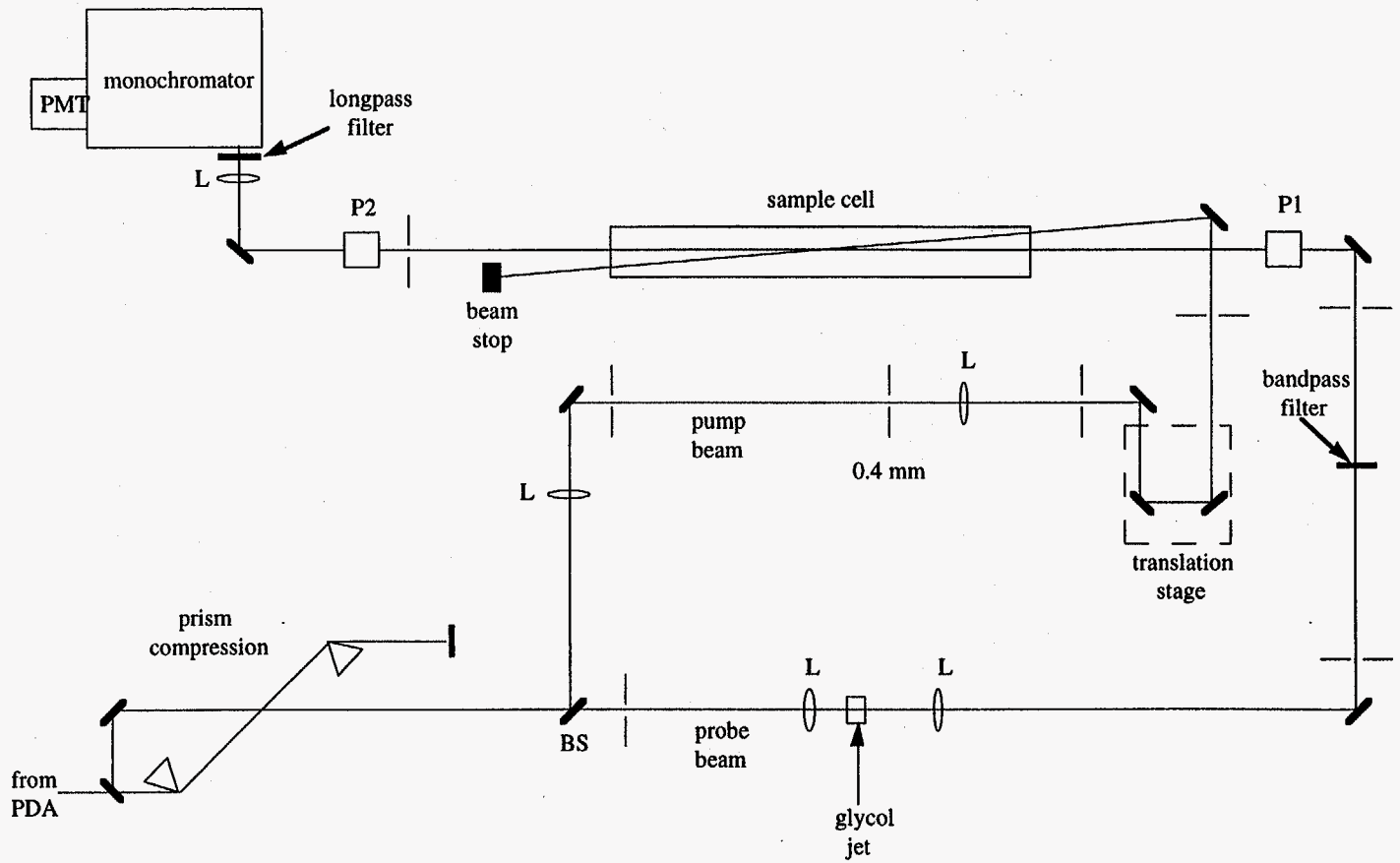

Fig. 2.3. Amplified CPM Femtosecond Laser System:
Compression, Interaction, and Detection Regions

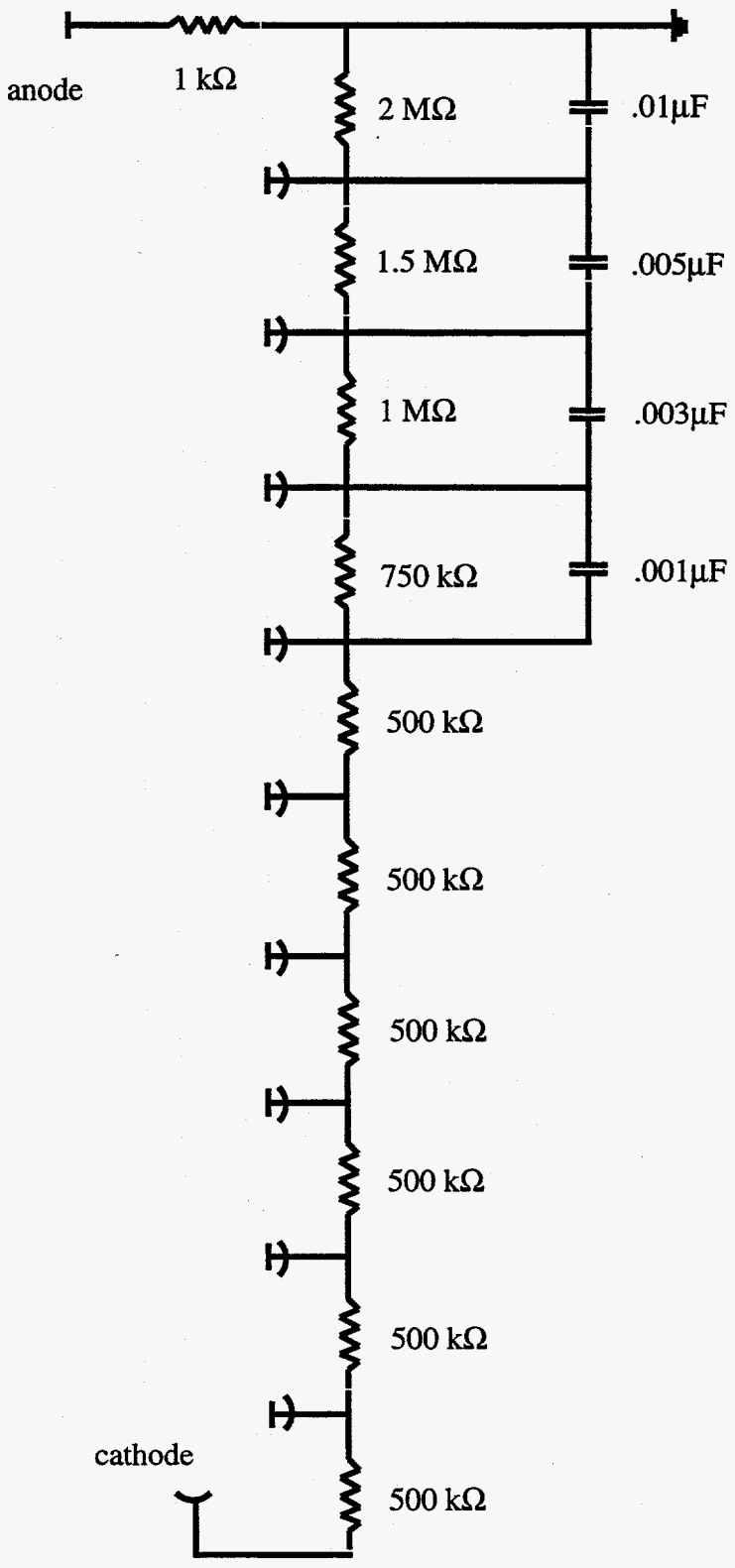

Fig. 2.4. PMT wiring diagram.

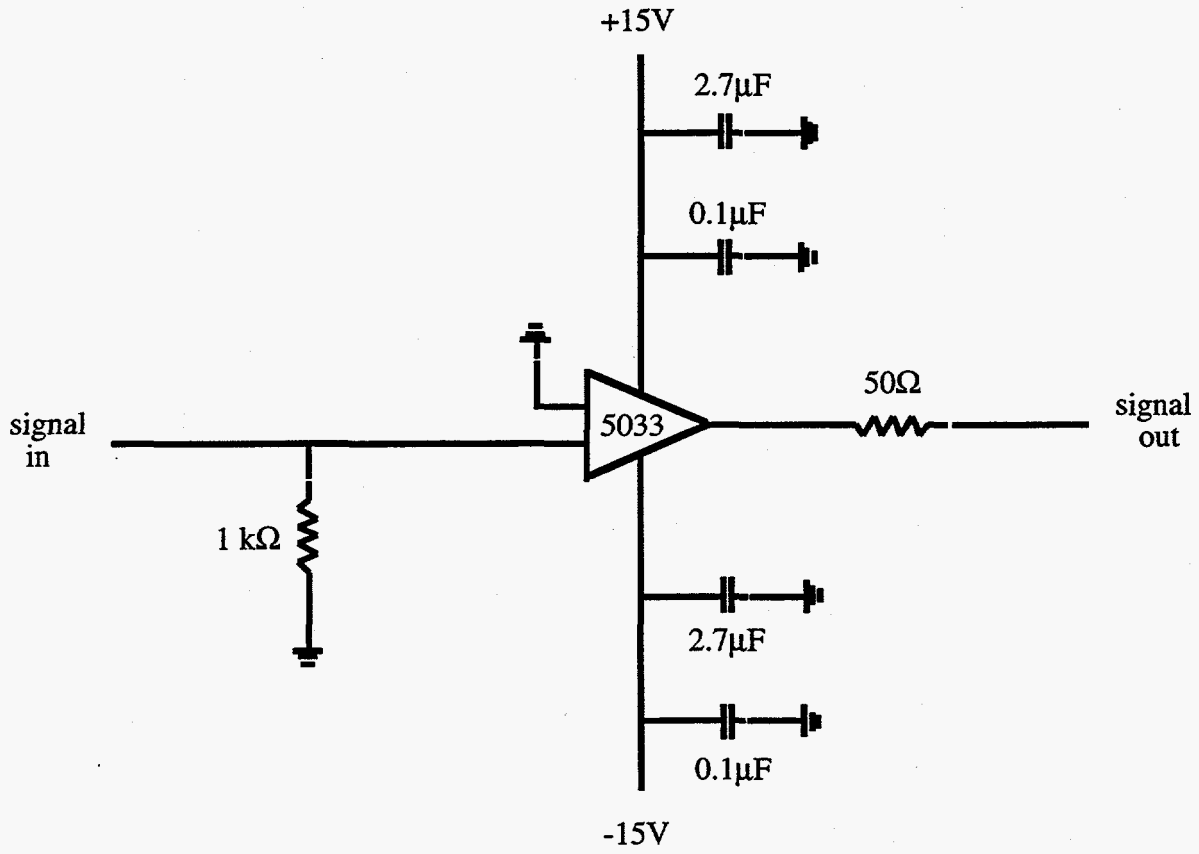

Fig. 2.5. Schematic of PMT preamplifier. Signal amplified by a factor of 20.

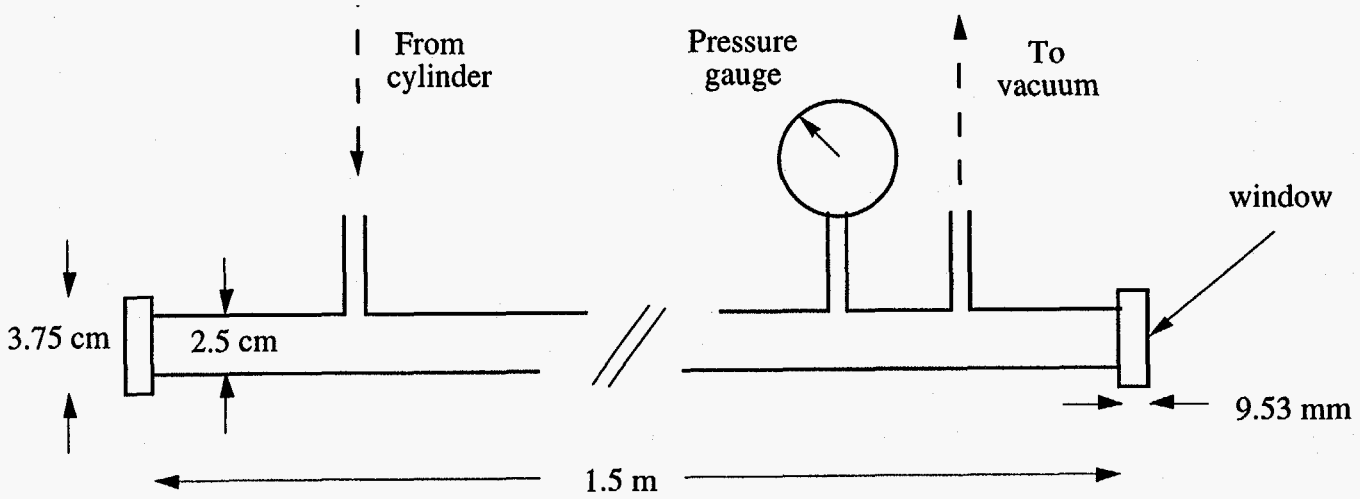

Fig. 2.6. Low pressure sample cell.

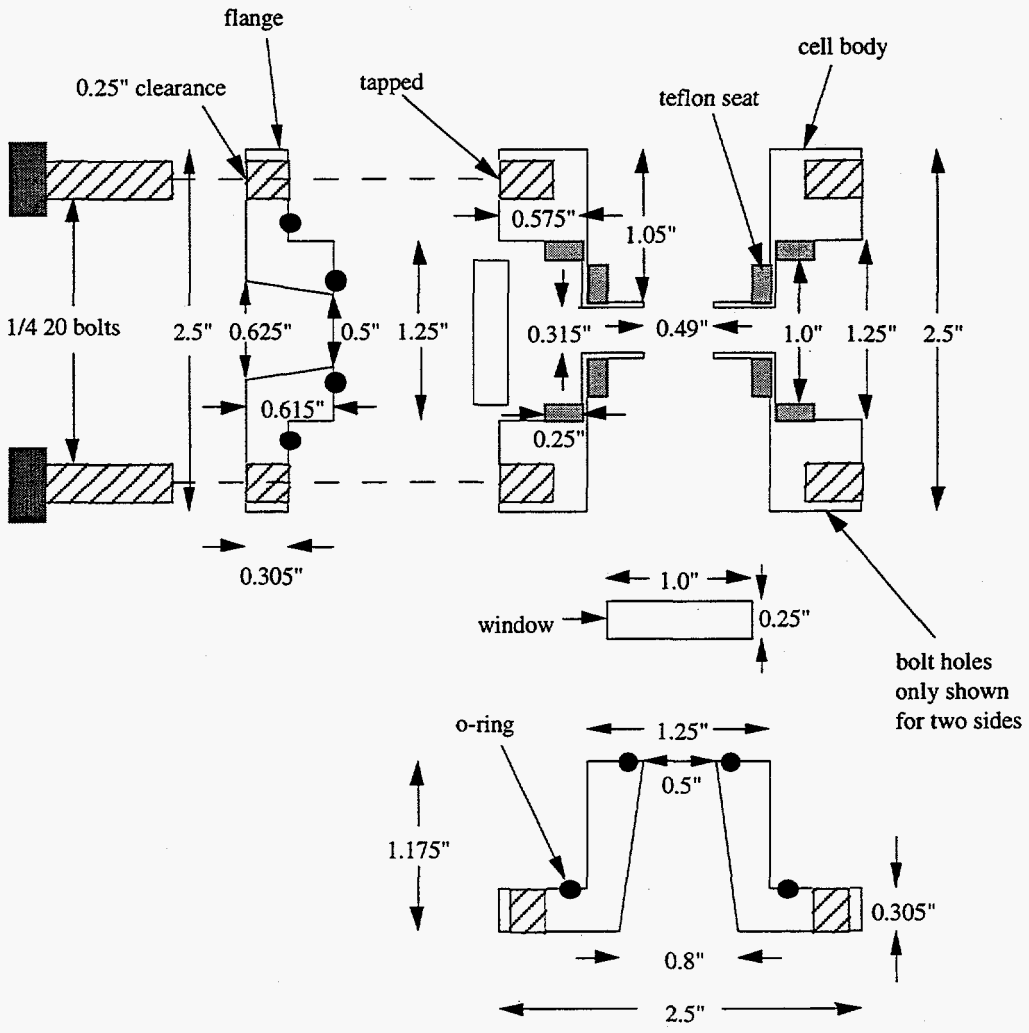

Fig. 2.7. High pressure sample cell cross section view from top.

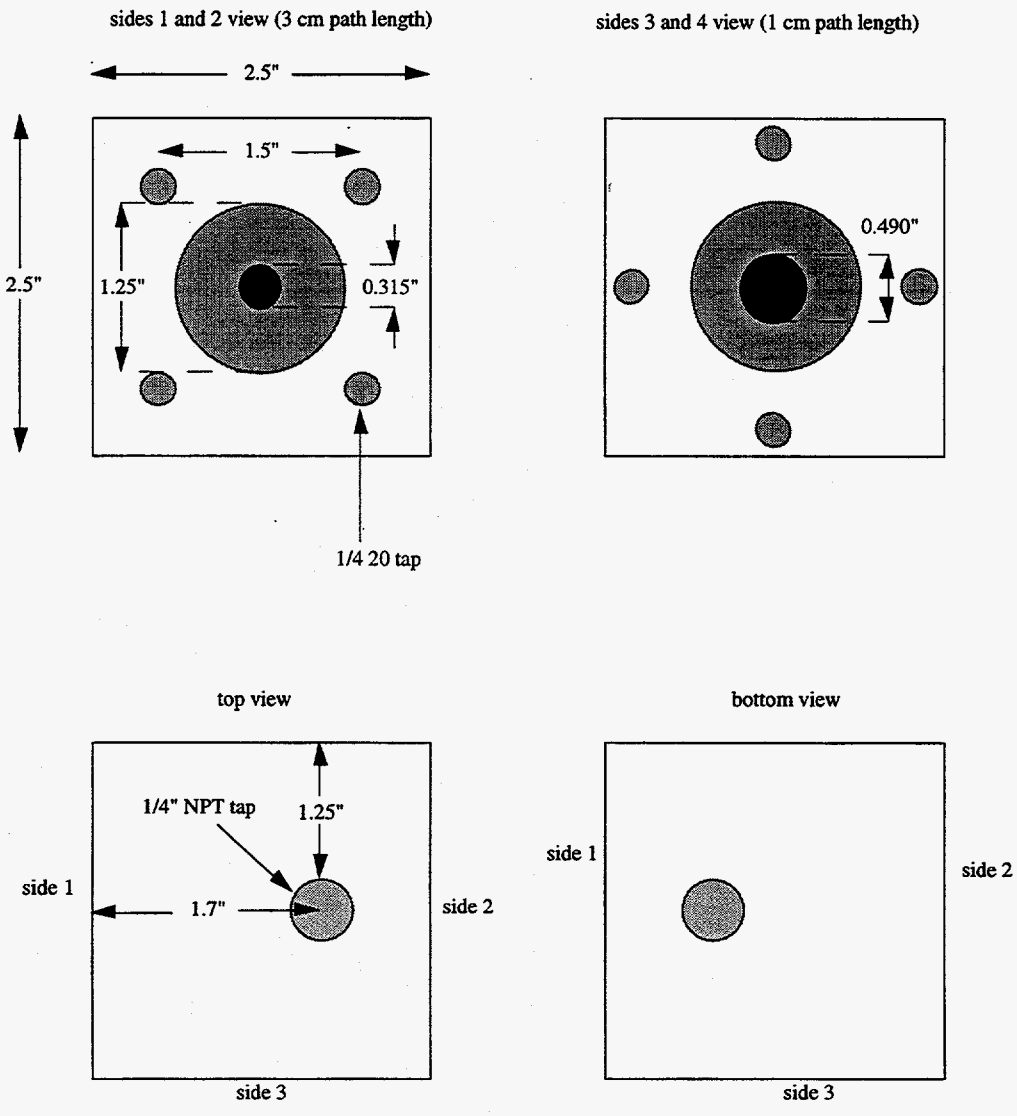

Fig. 2.8. High pressure cell.

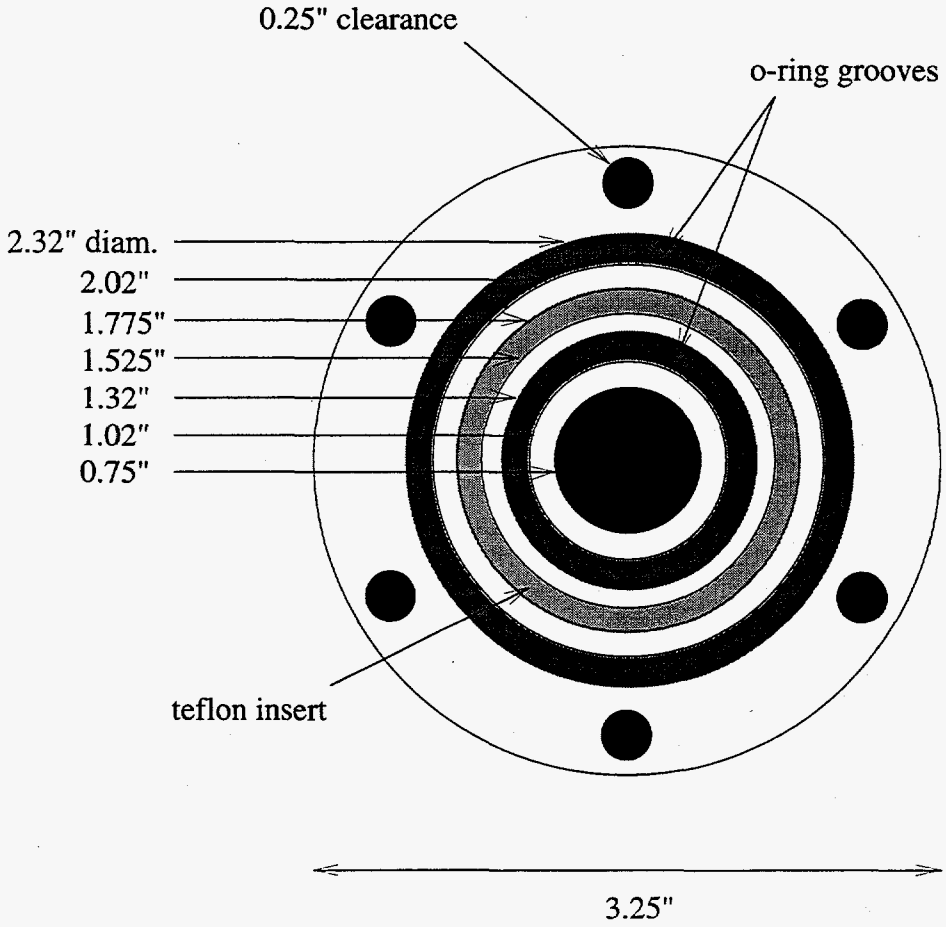

Fig. 2.9. Flange for high pressure cell, view from inside.

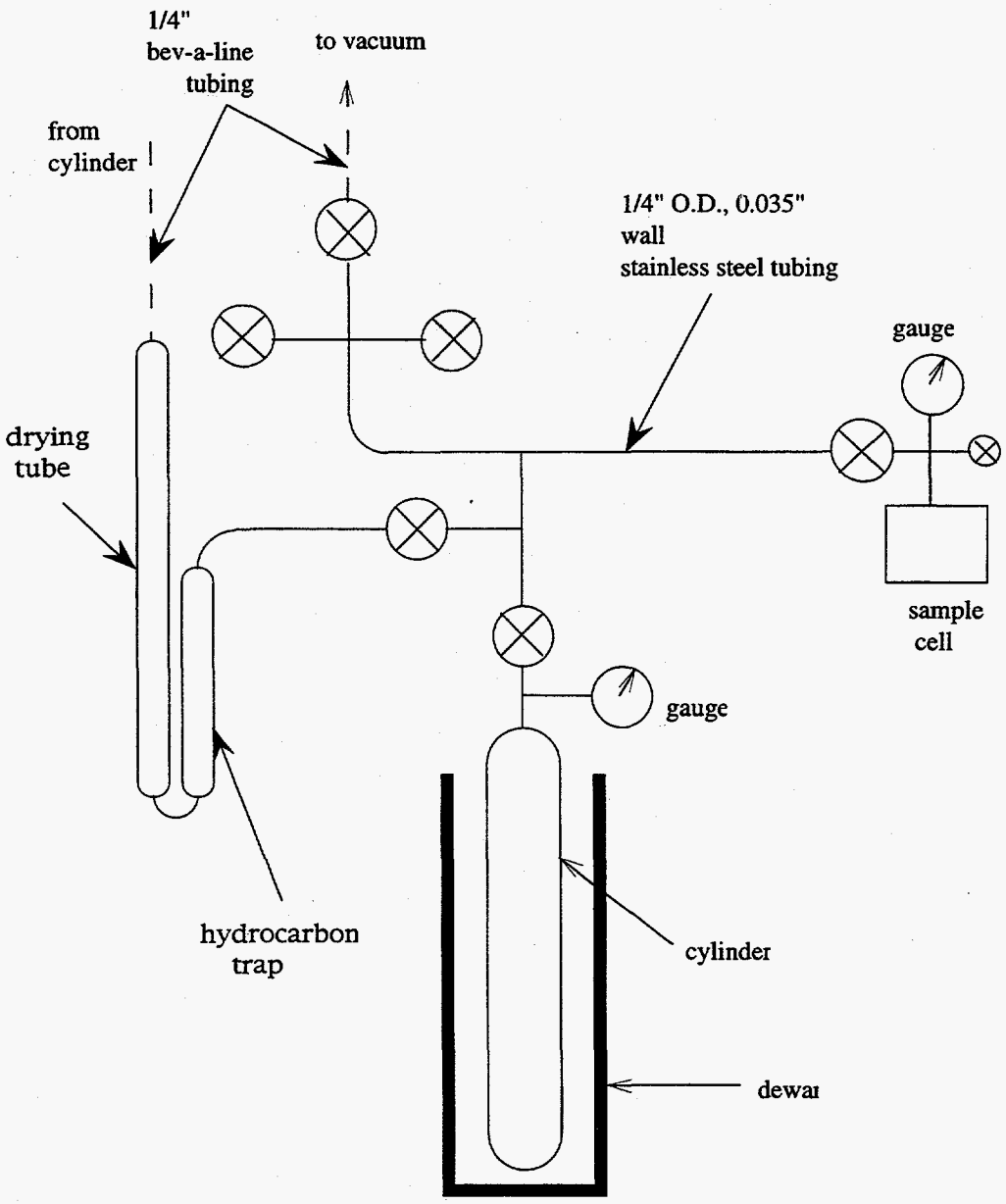

Fig. 2.10. High pressure gas handling manifold.

Chapter 3

Low Pressure Gases

3.1 Introduction

In this chapter we present a complete tensor analysis of the RIPS process. As in other pump-probe experiments, the molecular response in RIPS can be related to the third-order nonlinear susceptibility tensor, χ_{ijkl}. In Section 3.2 the correspondence between the Cartesian components of χ_{ijkl} and the irreducible molecular tensors is established using a spherical tensor formalism. It is shown that the molecular response in RIPS separates naturally into a superposition of three independent components, given by the autocorrelation functions of the Raman polarizability tensors of rank 0, 1, and 2, respectively. The weighting factor in the superposition is uniquely determined by the experimental configuration, i.e. the polarizations of the pump, probe, and detected field. We then generalize the tensor analysis to describe other pump-probe experiments, and to establish the relationship between the experimental observables in time- and frequency-domain techniques. In section 3.3 we give a general expression for the RIPS molecular response and apply it to symmetric and asymmetric tops. We compare theoretical and experimental results for CO_2 and O_3 as examples of a linear molecule and asymmetric top, respectively. Finally, the last section, 3.4, discusses the effects of collisions on the spectra at low gas densities.

3.2 Polarization Dependence and Tensor Analysis of the Molecular Response

3.21 Background

RIPS is a nonlinear optical technique involving coherent excitation of molecular rotations and/or other low frequency molecular modes. Like several other nonlinear coherent spectroscopies,[1] RIPS measures the third order nonlinear polarization. The effect can be understood within a density matrix formalism in the limit of perturbation theory.

The general form of the experimentally detected signal intensity is given by

$$I \propto \frac{1}{8\pi} \int_{-\infty}^{\infty} |E_s(t) + E_L(t)|^2 c\sigma \, dt, \tag{3.1}$$

where c is the speed of light, σ is the cross section of the probe laser beam, $E_s(t) = \mathcal{E}_s(t)e^{-i\omega_s t} + c.c.$ is the signal field, and $E_L(t) = \eta\mathcal{E}_d(t)e^{-i(\omega_d - \phi)t} + c.c.$ is the local oscillator field. Using the wave equation with the slowly-varying amplitude approximation in the limit of an optically thin sample,[2] one can show that the signal field amplitude in a sample of length L is

$$\mathcal{E}_s(L,t) = \frac{i2\pi\omega_d L}{cn} P^{(3)}(t), \tag{3.2}$$

where $P^{(3)} = P^{(3)}e^{-i\omega t} + P^{(3)*}e^{i\omega t}$ is the third order nonlinear polarization, ω_d is the probe laser frequency, and n is the index of refraction. In the limit of zero probe leakage (homodyne detection), a signal proportional to the square of the polarization would be detected:

$$I \propto \frac{\omega^2 L^2}{2cn^2} \int_{-\infty}^{\infty} \left(P^{(3)}(t)\right)^2 dt \ . \tag{3.3}$$

If desired, one can instead retain the phase information of the polarization by detecting a signal linear to $P^{(3)}(t)$ using an optical heterodyne technique. The heterodyned signal can be obtained by mixing the signal field with a much larger local oscillator field, in which case the signal will be dominated by the cross terms of Eq. (3.1). Even with a small oscillator field the heterodyne spectrum can be obtained by subtracting signals having oscillator fields of opposite sign. This eliminates the homodyne term while preserving the heterodyne signal. In either case the resulting signal is

$$I \propto \mathrm{Im}\left[\frac{\omega_d L}{4n} \int_{-\infty}^{\infty} \eta \mathcal{E}_d^*(t) P^{(3)}(t) e^{-i\phi} dt + \mathrm{c.c.}\right]. \tag{3.4}$$

Note that the heterodyne signal size can be increased dramatically by using a large local oscillator field, provided the field is stable. Another advantage of heterodyning is that it isolates either the birefringent or the dichroic parts of the signal, since linearly and circularly polarized light do not interfere with one another. Therefore, linearly polarized oscillator fields give the dichroic signal, and circularly polarized fields the birefringent signal.

The third order polarization is related to the third order density matrix by

$$P^{(3)}(t) = N\,\mathrm{Tr}\left[\mu(t)\rho^{(3)}(t)\right], \tag{3.5}$$

where N is the number density of the gas, $\mu(t)$ is the dipole operator, Tr represents the trace, and $\rho^{(3)}(t)$ is the third order density operator:

$$\rho^{(3)}(t)=\left(\frac{1}{i\hbar}\right)^3\int_{-\infty}^{t}dt_3\int_{-\infty}^{t_3}dt_2\int_{-\infty}^{t_2}dt_1\left[H'(t_3),\left[H'(t_2),\left[H'(t_1),\rho_0\right]\right]\right]. \tag{3.6}$$

In Eq. (3.6) $H'(t) = -\mu(t)E(t)$ is the interaction Hamiltonian and ρ_0 denotes the equilibrium density matrix operator. Unless otherwise stated all operators are assumed to be in the interaction representation,[3] e.g. $\mu(t) \equiv e^{iH_0 t/\hbar}\mu_s e^{-iH_0 t/\hbar}$, where μ_s is the dipole operator in the Schrödinger representation, and H_0 is the molecular Hamiltonian.

Expansion of the commutators in Eq. (3.6) results in 8 terms, which in turn give a total of 48 time-ordered terms upon permutation of the three interactions. Half of these can be neglected if the pump laser is far from resonance with any electronic transitions. Furthermore, when there is no time overlap of the pump and probe, only four of the remaining time-ordered terms are significant. These four terms correspond to the two double-sided Feynman diagrams[4] shown in Fig. 3.1 and their mirror images. The time axis runs from bottom to top in the diagrams. The first two interactions in each diagram are from the pump laser (ω_p), the second two from the probe laser (ω_d). The polarization due to the four terms is

$$P^{(3)}(t) = -\left(\frac{1}{i\hbar}\right)^3 \mathrm{Tr}\left\{N\int_{-\infty}^{t}dt_3\,\mu(t)\mu(t_3)E_d(t_3)\int_{-\infty}^{t_3}dt_2 \times\int_{-\infty}^{t_2}dt_1\left[\mu(t_2)E_p(t_2)\mu(t_1)E_p(t_1)\rho_0+\rho_0\mu(t_1)E_p(t_1)\mu(t_2)E_p(t_2)\right]\right\}+\text{c.c.} \tag{3.7}$$

In Eq. (3.7) E_p and E_d denote the pump and probe laser fields, respectively.

Due to the off-resonance condition, one often adopts the so-called fast dephasing approximation (FDA),[5-7] which is equivalent to setting $\mathcal{E}_p(t_1) = \mathcal{E}_p(t_2)$ and $\mathcal{E}_d(t) = \mathcal{E}_d(t_3)$ in Eq. (3.7). If we also introduce the scattering operators

$$\alpha(\omega) \equiv \frac{i}{\hbar}\int_0^\infty dt[\mu(0),\mu(-t)]e^{i\omega t}, \qquad \alpha_R(\omega) \equiv \frac{i}{\hbar}\int_0^\infty dt\, \mu(0)\mu(-t)e^{i\omega t}, \tag{3.8}$$

then Eq. (3.7) can be expressed as

$$P^{(3)}(t) = E_d(t)\int_{-\infty}^{\infty} |E_p(\tau)|^2 \chi(t-\tau)d\tau, \tag{3.9}$$

with the molecular response

$$\begin{aligned}\chi(\tau) &= -\frac{1}{i\hbar}\,\mathrm{Tr}\left\{N\rho_0\left[\alpha(\tau,\omega_d),\left(\alpha_R(0,\omega_p)+\alpha_R(0,-\omega_p)\right)\right]\right\} \\ &\approx -\frac{1}{i\hbar}\,\mathrm{Tr}\left\{N\rho_0\left[\alpha(\tau,\omega_d),\alpha(0,\omega_p)\right]\right\}\ ,\end{aligned} \tag{3.10}$$

where $\alpha(t,\omega) \equiv e^{iH_0 t/\hbar}\alpha(\omega)e^{-iH_0 t/\hbar}$ is again expressed in the interaction representation. It can be verified that the matrix element of $\alpha(\omega)$ between two levels of the ground electronic state is identical to the Dirac-Heisenberg Raman polarizability, and that $\alpha(\omega)$ is Hermitian when ω is far from any electronic transition. Note that Eq. (3.10) is equivalent to the expression of Yan and Mukamel (see Eqs. (5b), (12) of ref. 8), except the operators defined in Eq. (3.8) do not depend explicitly on the molecular energy levels.

Eq. (3.10) is simply a representation of the well-known linear response theory: the RIPS response is proportional to the autocorrelation of the Raman polarizability. However, when the dependence of the molecular response on laser polarizations is taken into account explicitly, this relationship to linear response theory becomes less apparent. $\chi(t)$ is in fact a fourth rank tensor, depending explicitly on four subscripts in the Cartesian coordinates. In standard nonlinear optics notation[9] it is written as $\chi(t)=\chi_{ijkl}(t,t_3,t_2,t_1)$, where the subscripts are paired with the time arguments from right to left. For isotropic

systems, only the four elements having ijkl=1111, 1122, 1221, and 1212 are nonzero,[2] where 1 and 2 represent orthogonal Cartesian coordinates (e.g. x and z). There are only three independent elements which can be measured, since the four elements above are related by $\chi_{1111} = \chi_{1212} + \chi_{1221} + \chi_{1122}$,[2] where the time dependence of the susceptibility elements is understood.

From Eq. (3.10) we see that in an off-resonant time-domain pump-probe experiment the susceptibility tensor elements are related to elements of the polarizability tensor according to

$$\chi_{ijkl} \propto \left\langle \alpha_{ij}(t)\alpha_{kl} \right\rangle. \tag{3.11}$$

As discussed by numerous authors,[2,4,10,11] a given experiment often measures some combination of the four nonzero Cartesian susceptibility components mentioned above. For example, in a typical RIPS experiment the pump and probe are linearly polarized with their polarization vectors oriented at a relative angle of 45°, while the signal field is polarized in a direction perpendicular to the probe, e.g. $\hat{\mathbf{e}}_p = (\hat{\mathbf{x}} + \hat{\mathbf{z}})/\sqrt{2}$, $\hat{\mathbf{e}}_d = \hat{\mathbf{z}}$, $\hat{\mathbf{e}}_s = \hat{\mathbf{x}}$. Therefore, the RIPS experimental observable is proportional to $\chi_{xzxz} + \chi_{xzzx} = \chi_{xxxx} - \chi_{xxzz}$, which is a combination of an autocorrelation and a cross correlation between Cartesian components of the polarizability tensor. The experimentally measured response depends on both the experimental configuration and the fundamental molecular properties.

3.22 Spherical tensor description of the nonlinear susceptibility

The relationship between the third order susceptibility and the fundamental molecular properties for an isotropic system has been investigated by many workers.[10,12-15] In particular, it has been pointed out that if the orientational motion of a molecular system is decoupled from the rest of the degrees of freedom, the tensorial susceptibility can be decomposed into the product of a rotational or geometric part and an internal or dynamic

part. Explicit expressions for these two components have been given for liquids[14] assuming a diffusional model for the orientational motion. This approach, however, can be generalized using the irreducible tensor formalism. In other words, the four nonzero Cartesian tensor elements (χ_{ijkl}) can be decomposed into three independent components, which represent the inherent molecular properties.

For simplicity, only the explicit tensor form for the first term of Eq. (3.10) is discussed, since subsequent inclusion of the second term is trivial. The first term is written as

$$\chi(\tau) = -\frac{N}{i\hbar}\mathrm{Tr}\left\{\left(\hat{\mathbf{e}}_s \bullet \alpha(\tau) \bullet \hat{\mathbf{e}}_d\right)\left(\hat{\mathbf{e}}_p^* \bullet \alpha(0)\rho_0 \bullet \hat{\mathbf{e}}_p\right)\right\}, \tag{3.12}$$

where $\hat{\mathbf{e}}_s$ is the polarization of the detected field, $\hat{\mathbf{e}}_p$ and $\hat{\mathbf{e}}_d$ are the polarizations of the pump and probe lasers, respectively, and the tensor contraction is defined by[16]

$$\left(\hat{\mathbf{e}}_a \bullet \alpha \bullet \hat{\mathbf{e}}_b\right) = \sum_{i,j} \alpha_{ij} e_a^i e_b^j = \sum_{k,q} (-1)^{k-q} [\alpha]_q^{(k)} \left[\hat{\mathbf{e}}_a \otimes \hat{\mathbf{e}}_b\right]_{-q}^{(k)}. \tag{3.13}$$

The right side of Eq. (3.13) has been expressed in spherical tensor notation. The above relation can be used to write the trace in Eq. (3.12) as

$$\left(\hat{\mathbf{e}}_s \bullet \alpha(\tau) \bullet \hat{\mathbf{e}}_d\right)\left(\hat{\mathbf{e}}_p^* \bullet \alpha(0) \bullet \hat{\mathbf{e}}_p\right) = \sum_{k,k',q,q'} (-1)^{k+k'-q-q'} [\alpha(\tau)]_q^{(k)} [\alpha(0)]_{q'}^{(k')} \left[\hat{\mathbf{e}}_s \otimes \hat{\mathbf{e}}_d\right]_{-q}^{(k)} \left[\hat{\mathbf{e}}_p^* \otimes \hat{\mathbf{e}}_p\right]_{-q'}^{(k')} \tag{3.14}$$

From two spherical tensors of rank k and k', one can construct a so-called bipolar harmonic tensor of rank L[17]

$$M_m^{(L)}(kk') \equiv \sum_{q,q'} (-1)^{k-k'+m} \sqrt{2L+1} \begin{pmatrix} k & k' & L \\ q & q' & -m \end{pmatrix} [\alpha]_q^{(k)} [\alpha]_{q'}^{(k')}, \tag{3.15}$$

where the expression in parenthesis denotes the 3-j symbol. The reversed expression can be easily obtained using the orthogonal property of the 3-j symbols,

$$[\alpha]_q^{(k)} [\alpha]_{q'}^{(k')} = \sum_{L,m} (-1)^{k-k'+m} \sqrt{2L+1} \begin{pmatrix} k & k' & L \\ q & q' & -m \end{pmatrix} M_m^{(L)}(kk'). \tag{3.16}$$

For an isotropic system such as a gas or a liquid, only the rank zero tensor has a nonzero equilibrium average. Thus,

$$\mathrm{Tr}\left[[\alpha]_q^{(k)} [\alpha]_{-q}^{(k)} \rho_0\right] = \mathrm{Tr}\left[\frac{(-1)^{k-q}}{\sqrt{2k+1}} M_0^0(kk)\rho_0\right]. \tag{3.17}$$

As a special case of Eq. 3.17

$$\mathrm{Tr}\left[[\alpha]_0^{(k)} [\alpha]_0^{(k)} \rho_0\right] = \mathrm{Tr}\left[\frac{(-1)^{k}}{\sqrt{2k+1}} M_0^0(kk)\rho_0\right]. \tag{3.18}$$

Comparing Eqs. (3.17) and (3.18), we obtain

$$\mathrm{Tr}\left([\alpha]_q^{(k)} [\alpha]_{-q}^{(k)} \rho_0\right) = (-1)^q \mathrm{Tr}\left([\alpha]_0^{(k)} [\alpha]_0^{(k)} \rho_0\right). \tag{3.19}$$

The entire tensor expression (3.14) reduces to

$$\begin{aligned} &\mathrm{Tr}\left[\left(\hat{e}_s \bullet \alpha(\tau) \bullet \hat{e}_d\right)\left(\hat{e}_p^* \bullet \alpha(0) \bullet \hat{e}_p\right)\rho_0\right] \\ &\quad = \sum_{k,q} (-1)^q \left[\hat{e}_s \otimes \hat{e}_d\right]_{-q}^{(k)} \left[\hat{e}_p^* \otimes \hat{e}_p\right]_q^{(k)} \mathrm{Tr}\left[[\alpha(\tau)]_0^{(k)} [\alpha(0)]_0^{(k)} \rho_0\right]. \end{aligned} \tag{3.20}$$

The right side of Eq. (3.20) is a sum of three terms, each of which contains the autocorrelation function of an irreducible molecular tensor. These terms can be written as

$$c_0 \mathrm{Tr}\left[[\alpha(\tau)]_0^{(0)}\,[\alpha(0)]_0^{(0)}\rho_0\right] + c_1 \mathrm{Tr}\left[[\alpha(\tau)]_0^{(1)}\,[\alpha(0)]_0^{(1)}\rho_0\right] + c_2 \mathrm{Tr}\left[[\alpha(\tau)]_0^{(2)}\,[\alpha(0)]_0^{(2)}\rho_0\right]$$

where

$$c_k = \sum_q (-1)^q \left[\hat{e}_s \otimes \hat{e}_d\right]_{-q}^{(k)} \left[\hat{e}_p^* \otimes \hat{e}_p\right]_q^{(k)} \tag{3.21}$$

is a constant that depends only upon the experimental configuration. The three autocorrelation functions are those of the isotropic, antisymmetric and symmetric polarizabilities, respectively, and represent the rotationally invariant molecular properties one can measure in a nonresonant four wave mixing experiment. The orientational aspect of the molecular response is contained in the last two functions. To what degree a given experiment measures the orientational properties of a molecular system as opposed to the isotropic properties, depends of course, on the experimental configuration. The c_k's in Eq. (3.21) can be easily evaluated for the aforementioned nonzero Cartesian tensor elements:

$$\begin{aligned}
\chi_{1111} &\propto \frac{1}{3}\left\langle [\alpha(t)]_0^{(0)} [\alpha(0)]_0^{(0)} \right\rangle + \frac{2}{3}\left\langle [\alpha(t)]_0^{(2)} [\alpha(0)]_0^{(2)} \right\rangle \\
\chi_{1212} &\propto -\frac{1}{2}\left\langle [\alpha(t)]_0^{(1)} [\alpha(0)]_0^{(1)} \right\rangle + \frac{1}{2}\left\langle [\alpha(t)]_0^{(2)} [\alpha(0)]_0^{(2)} \right\rangle \\
\chi_{1221} &\propto \frac{1}{2}\left\langle [\alpha(t)]_0^{(1)} [\alpha(0)]_0^{(1)} \right\rangle + \frac{1}{2}\left\langle [\alpha(t)]_0^{(2)} [\alpha(0)]_0^{(2)} \right\rangle \\
\chi_{1122} &\propto \frac{1}{3}\left\langle [\alpha(t)]_0^{(0)} [\alpha(0)]_0^{(0)} \right\rangle - \frac{1}{3}\left\langle [\alpha(t)]_0^{(2)} [\alpha(0)]_0^{(2)} \right\rangle
\end{aligned} \tag{3.22}$$

In the limit that the polarizability is symmetric ($\alpha^{(1)} = 0$) and the molecular rotation is separable and diffusional, Eqs. (3.22) reduce to the expressions given by Myers and Hochstrasser,[14]

$$\chi_{1111} \propto \frac{1}{3}\left(1 + 2r_0 e^{-T/\tau}\right) \qquad (3.23)$$
$$\chi_{1212} = \chi_{1221} \propto \frac{1}{2} r_0 e^{-T/\tau}$$
$$\chi_{1122} \propto \frac{1}{3}\left(1 - r_0 e^{-T/\tau}\right)$$

where τ is the rotational diffusion constant and r_0 is the initial anisotropy.

The general relations of Eqs. (3.22) allow one to easily determine what molecular property is observed in any off-resonant scattering experiment having an arbitrary polarization configuration. For a RIPS experiment utilizing a linear pump beam, Eq. (3.20) and Eqs. (3.22) show that the observed signal is proportional to the autocorrelation of the symmetric polarizability tensor, $\chi_{1221} + \chi_{1212} \propto \left\langle [\alpha(t)]_0^{(2)} [\alpha(0)]_0^{(2)} \right\rangle$. Furthermore, from Eq. (3.21) it can be determined that, for copropagating beams, a relative angle of 45° between the pump and probe polarizations gives the maximum signal. If the pump pulse is circularly polarized instead, i.e. $\hat{e}_p = (\hat{x} + i\hat{z})/\sqrt{2}$, $\hat{e}_p^* = (\hat{x} - i\hat{z})/\sqrt{2}$, then Eqs. (3.22) indicate that one would measure only the antisymmetric component of the polarizability, $\chi_{1212} - \chi_{1221} \propto \left\langle [\alpha(t)]_0^{(1)} [\alpha(0)]_0^{(1)} \right\rangle$. Thus, depending upon the polarization configuration, RIPS measures *either* the symmetric ($\alpha_0^{(2)}$) *or* the antisymmetric ($\alpha_0^{(1)}$) component of the polarizability.

Depolarized spontaneous Raman experiments, meanwhile, measure $|\alpha_{xz}|^2$,[18] the Fourier transform of the autocorrelation of the polarizability element, $\alpha_{xz}\alpha_{xz}(t) \propto \chi_{1212}$. According to Eqs. (3.22) the depolarized Raman experiment, in contrast to RIPS, necessarily measures a *combination* of $\alpha_0^{(1)}$ *and* $\alpha_0^{(2)}$. Of course, when the antisymmetric part of the polarizability is zero (i.e. $\alpha_{ij} = \alpha_{ji}$), as is often the case,[19,20] the depolarized Raman experiment and the RIPS experiment utilizing a linear pump both measure only the

symmetric polarizability. Only under these circumstances are the two experiments related by the Fourier transform.

3.23 Generalization to other time and frequency domain pump-probe experiments

The above tensor analysis is applicable to other scattering experiments as well. For example, the three pulse impulsive stimulated Raman scattering (ISRS) technique of Nelson *et. al.*[21] typically utilizes two pump beams having x and z polarization, respectively, an x-polarized probe, and z-polarized signal field. Use of Eqs. (3.22) shows that this experiment, like RIPS, measures the autocorrelation of $\alpha_0^{(2)}$. However, ISRS has also been done with all fields polarized identically, in which case both orientational and isotropic properties are measured, since the signal has contributions from $\alpha_0^{(2)}$ and $\alpha_0^{(0)}$.

When resonances are involved, such as in transient absorption or fluorescence experiments, the tensor analysis is analogous. In the case of transient absorption, for example, the nonlinear polarization in Eq. (3.7) is replaced by[22,23]

$$P^{(3)}(t) = -\left(\frac{1}{i\hbar}\right)^3 \mathrm{Tr}\{\, N \int_{-\infty}^{t} dt_3\, \mu(t) \int_{-\infty}^{t_3} dt_2 \int_{-\infty}^{t_2} dt_1 \big[\mu(t_2)E_p(t_2)\rho_0\mu(t_1)E_p(t_1) + \mu(t_1)E_p(t_1)\rho_0\mu(t_2)E_p(t_2)\big]\mu(t_3)E_d(t_3)\,\} + \text{c.c.} \tag{3.24}$$

As a result, the polarizability operators in Eq. (3.10) must be replaced by appropriate products of dipole operators. The polarization dependence of the experiment, however, can be analyzed in exactly the same manner as for the off-resonance case. For example, from Eqs. (3.22) it can be shown that when the probe and signal fields are chosen to have the same polarization, the measured response is given by

$$\chi \propto \frac{1}{3}\left\langle [G(t)]_0^{(0)} [G(0)]_0^{(0)} \right\rangle + \frac{2}{3} P_2(\cos\theta)\left\langle [G(t)]_0^{(2)} [G(0)]_0^{(2)} \right\rangle, \tag{3.25}$$

where P_2 represents the second Legendre polynomial, θ is the angle between the pump and probe field polarizations, and G is an operator defined by

$$G\rho \equiv \int_0^\infty \mu(\tau)\rho\mu e^{i\omega\tau} d\tau.$$

As a second rank tensor, G has properties similar to both the polarizability tensor and the "doorway" and "window" wavepackets discussed in reference 13. As in the off-resonant case, we have evaluated only the first term of Eq. (3.24) (see discussion above Eq. (3.12)).

When "magic angle" detection ($\theta \approx 54.74°$) is used, P_2=0, and one obtains the well-known result that only the isotropic response is measured. One can also eliminate the orientational part of the signal when the probe and signal fields have different polarizations. In this case

$$\chi \propto \frac{1}{3}(\cos\phi\cos\theta + \sin\phi\sin\theta)\left\langle [G(t)]_0^{(0)}[G(0)]_0^{(0)}\right\rangle + \frac{1}{3}(2\cos\phi\cos\theta - \sin\phi\sin\theta)\left\langle [G(t)]_0^{(2)}[G(0)]_0^{(2)}\right\rangle \tag{3.26}$$

where ϕ is the angle between the pump and signal fields and θ is defined above, i.e. $\hat{\mathbf{e}}_{pu} = \hat{\mathbf{z}}$, $\hat{\mathbf{e}}_{pr} = \sin\theta\,\hat{\mathbf{x}} + \cos\theta\,\hat{\mathbf{z}}$, $\hat{\mathbf{e}}_{sig} = \sin\phi\,\hat{\mathbf{x}} + \cos\phi\,\hat{\mathbf{z}}$. Although there is an infinite number of (θ, ϕ) combinations that can be chosen such that the signal is isotropic, often $\theta = \phi = 63.44°$ is used. This is usually called "mystic angle" detection.[15]

It should be noted that frequency-domain experiments having pump, probe, and signal field polarizations identical to those in similar time-domain experiments measure a different quantity than their time-domain counterparts. For example, when the pump and probe lasers are linearly polarized at a relative angle of 45°, frequency-domain RIKES

measures a combination of the isotropic and nonisotropic responses, whereas the time-domain RIKES measures only the nonisotropic part. The reason, which has been pointed out recently by Ziegler *et. al.*,[11] is that in the time-domain experiments the pump pulse alone provides the initial molecular excitation, whereas in the frequency-domain experiment this excitation is created by a *simultaneous* interaction with both the pump and probe laser fields having different polarizations. This point can be illustrated more clearly using the irreducible tensor analysis.

First, note that the correspondence between frequency-domain tensor element subscripts:

$$\chi_{ijkl}(\omega_2;\omega_2,\omega_1,-\omega_1) \propto \alpha_{ik}(-\omega_2,\omega_1)\alpha^*_{jl}(-\omega_2,\omega_1) \tag{3.27}$$

(see Eq. (4.65) of ref. 9) differs from that in the similar time-domain expression (Eq. (3.11)). This is true not only for scattering, but for absorption and emission experiments as well, since the tensorial properties of the G operator defined after Eq. (3.25) are identical to those of the polarizability. Thus, the correspondence of the tensor subscripts will be similar to that in Eqs. (3.11) and (3.27).

Applying the same tensor analysis used earlier, we can relate the frequency-domain susceptibilities to their time-domain counterparts given in Eqs. (3.22):

$$\begin{aligned}
\chi_{1111}(\omega) &\propto \frac{1}{3}\left|[\alpha(\omega)]_0^{(0)}\right|^2 + \frac{2}{3}\left|[\alpha(\omega)]_0^{(2)}\right|^2 \\
\chi_{1212}(\omega) &\propto \frac{1}{3}\left|[\alpha(\omega)]_0^{(0)}\right|^2 - \frac{1}{3}\left|[\alpha(\omega)]_0^{(2)}\right|^2 \\
\chi_{1221}(\omega) &\propto \frac{1}{2}\left|[\alpha(\omega)]_0^{(1)}\right|^2 + \frac{1}{2}\left|[\alpha(\omega)]_0^{(2)}\right|^2 \\
\chi_{1122}(\omega) &\propto -\frac{1}{2}\left|[\alpha(\omega)]_0^{(1)}\right|^2 + \frac{1}{2}\left|[\alpha(\omega)]_0^{(2)}\right|^2
\end{aligned} \tag{3.28}$$

where for convenience we keep only a single frequency argument to specify the tensor. The above relationships can be used to compare time- and frequency-domain experiments. For example, frequency-domain RIKES with a linear pump measures

$$\chi_{1212}(\omega_{pr};\omega_{pr},\omega_{pu},-\omega_{pu})+\chi_{1221}(\omega_{pr};\omega_{pr},\omega_{pu},-\omega_{pu})\propto\frac{1}{3}\left|\alpha_0^{(0)}\right|^2+\frac{1}{2}\left|\alpha_0^{(1)}\right|^2+\frac{1}{6}\left|\alpha_0^{(2)}\right|^2, \tag{3.29}$$

which is not the Fourier transform of the analogous time-domain observable (see discussion following Eqs. (3.23)).

With a circular pump, frequency-domain RIKES experiments measure

$$\begin{aligned}\chi_{1212}(\omega_{pr};\omega_{pr},\omega_{pu},-\omega_{pu})-\chi_{1221}(\omega_{pr};\omega_{pr},\omega_{pu},-\omega_{pu})&\propto\frac{1}{3}\left|\alpha_0^{(0)}\right|^2-\frac{1}{2}\left|\alpha_0^{(1)}\right|^2-\frac{5}{6}\left|\alpha_0^{(2)}\right|^2 \\ &=(1-3\rho_Q)\left|\alpha_{11}\right|^2,\end{aligned} \tag{3.30}$$

where $\rho_Q=\left|\alpha_{12}\right|^2/\left|\alpha_{11}\right|^2$ is the Raman depolarization ratio.[18] The signal is nonzero when the polarizability is symmetric. This is in contrast to the similar time-domain experiment, where we have indicated that, when $\alpha^{(1)}=0$, there is no RIPS signal for a circularly polarized pump beam. This has been demonstrated in Fig. 3.2. The figure shows RIPS spectra for CO_2 at 200 Torr taken under identical conditions, except that the polarization of the pump pulse was linear for the spectrum in Fig. 3.2(a) and circular in 3.2(b). Within the experimental sensitivity, the signal vanishes for the latter.

The disappearance of the RIPS signal for a circularly polarized pump when $\alpha^{(1)}=0$ has important implications for experiments aimed at observing excited state dynamics. When there are electronic resonances, one will generally see not only the excited state dynamics described by Eq. (3.24), but also ground state dynamics resulting from those interactions that are responsible for RIPS (Eq. 3.7).[24] However, by using a circularly

polarized pump, one can observe exclusively those processes in which there is absorption and/or stimulated emission, since the ground state RIPS processes do not contribute.

3.3 Rips Response For Symmetric And Asymmetric Tops

In this section a general formula for the RIPS molecular response is derived and then applied to symmetric and asymmetric tops. The general features of the response will be discussed for each case. The theoretical results are used to simulate RIPS spectra for CO_2, N_2, and O_3, which are then compared to experimental data.

Using Eq. (3.22), the RIPS response of Eqs. (3.10) and (3.12) can be written in irreducible tensor form as

$$\chi(t) = \frac{iN}{2\hbar}\left\langle\left[[\alpha(t)]_0^{(2)},[\alpha(0)]_0^{(2)}\right]\right\rangle, \tag{3.31}$$

where the angled brackets represent an ensemble average. The polarizability matrix elements of Eq. (3.31) can be evaluated by transforming the α's into the molecular reference frame:

$$\alpha_0^{(2)} = \sum_{\ell=-2}^{2} D_{0\ell}^{2*}\alpha_\ell'^{(2)} \ , \tag{3.32}$$

where $D_{0\ell}^2$ is the Wigner rotation matrix,[16] and the prime denotes the tensor in the molecular frame. The response is then expanded as

$$\chi(t) = \frac{iN}{2\hbar}\sum_{\ell,\ell'}\left\langle\left[D_{0\ell}^{2*}(t)[\alpha'(t)]_\ell^{(2)}, D_{0\ell'}^{2*}(0)[\alpha'(0)]_{\ell'}^{(2)}\right]\right\rangle. \tag{3.33}$$

Eq. (3.33) can be rewritten as[25]

$$\chi(t)=\frac{N}{2kT}\sum_{\ell,\ell'}\left(\left\langle[\alpha'(t)]_{\ell}^{(2)}[\alpha'(0)]_{\ell'}^{(2)}\right\rangle\frac{d}{dt}\left\langle\tilde{D}_{0\ell'}^{2*}(0)D_{0\ell}^{2*}(t)\right\rangle+\left\langle D_{0\ell'}^{2*}(0)D_{0\ell}^{2*}(t)\right\rangle\frac{d}{dt}\left\langle[\tilde{\alpha}'(0)]_{\ell'}^{(2)}[\alpha'(t)]_{\ell}^{(2)}\right\rangle\right) \tag{3.34}$$

where $\tilde{B}(0)\equiv kT\int_0^{1/kT}d\lambda e^{\lambda H^0}B(0)e^{-\lambda H^0}$ is the Kubo transform[18] of the operator B, $\left\langle\tilde{\alpha}_{\ell'}^{\prime(2)}(0)\alpha_{\ell}^{\prime(2)}(t)\right\rangle$ represents an average over the vibronic wavefunctions only, and

$$\left\langle\tilde{D}_{0\ell'}^{2*}(0)D_{0\ell}^{2*}(t)\right\rangle=\sum_{J\tau M}\rho_0\langle J\tau M|\tilde{D}_{0\ell'}^{2*}(0)D_{0\ell}^{2*}(t)|J\tau M\rangle, \tag{3.35}$$

where the rotational states are labeled by the total angular momentum (J), the projection of angular momentum along the space-fixed z axis (M), and τ, which distinguishes states with the same M and J but different energy. For symmetric tops τ=K, where K is the projection of angular momentum along the symmetry axis.[26]

Note from Eq. (3.34) that when vibration and rotation are separable the RIPS response for a linear pump contains two terms. These two terms can be expected to have a similar time dependence, since each term contains both vibrational and rotational dynamics. For example, if the rotational motion is diffusional, then both terms will decay with the same diffusion constant. A similar argument holds for the vibrational motion. Thus, in general both terms must be considered together.

The nonseparability of the time scales is most obvious for relatively small molecules. As discussed in the next section, the rotational dephasing time, determined by the destructive interference of the initial rotational wavepacket, is less than 100 fs for molecules such as CO_2, even though the characteristic rotational time scale $\tau_R = 1/Bc >> 1$ ps . Under these circumstances the first term of Eq. (3.34) can significantly affect the experimentally observed ultrafast dynamics. Conversely, for very large molecules the

derivative of the rotational correlation function may be much smaller than the correlation function itself. The first term of Eq. (3.34) could then be neglected relative to the second.

The second term, often referred to as that responsible for the experimentally observed vibrational dynamics, has been discussed in detail by many authors (see e.g. ref. 10 and references therein). Our emphasis will be on the first term, in particular the full quantum mechanical manifestation of the coherent rotational motions excited by an ultrafast pump pulse. For the di- and triatomic molecules discussed here, ultrafast lasers having a pulse width $\tau \approx$50-100 fs do not have a sufficient bandwidth to couple different vibrational states. As a result the vibrational average is time-independent, i.e.

$$\left\langle \tilde{\alpha}_{\ell'}^{\prime(2)}(0)\alpha_{\ell}^{\prime(2)}(t)\right\rangle = \left[\tilde{\alpha}_{\ell'}^{\prime(2)}\right]_{GG}\left[\alpha_{\ell}^{\prime(2)}\right]_{GG}, \tag{3.36}$$

where the quantity on the right represents a product of ground vibronic state matrix elements. Of course, for molecules having low frequency modes the laser can couple vibrational states, leading to vibrational coherence.[24,27,28] While the above discussion emphasizes the time dependence of the second rank molecular tensors, it should be pointed out that it applies to other ranks as well. That is, one only has to replace the superscript '2' with '0' or '1', to generalize to these other cases.

3.31 Symmetric Tops (N_2, CO_2, O_2)

The Wigner-Eckart theorem, in conjunction with the properties of Wigner rotation matrices and 3-j symbols, can be used to evaluate the rotational matrix elements in Eq. (3.34). Noting that for a symmetric top the matrix elements of $\alpha^{\prime(2)}$ are only nonzero when $\ell, \ell' = 0$ due to symmetry, and substituting $\alpha_0^{\prime(2)} = \sqrt{2/3}(\alpha_{\parallel} - \alpha_{\perp})$,[18] the first term of Eq. (3.34) can be written

$$\chi(t)=\frac{N}{i\hbar}\sum{}' \frac{1}{15}\left(\rho_{g'}-\rho_g\right)e^{\omega_{gg'}t}\left(\alpha_{\parallel}-\alpha_{\perp}\right)^2(2J+1)(2J'+1)\begin{pmatrix} J' & J & 2 \\ K & -K & 0\end{pmatrix}^2 \tag{3.37}$$

where the sum in this equation is over the thermally accessible rotational states, $\rho_g = e^{-E/kT}/Q$, $(J'-J)=\Delta J=\pm1,\pm2$, and the frequencies are given by

$$\omega_{gg'}=4\pi Bc(J_g+1)+i\Gamma_{gg'}, \qquad (\Delta J=-1) \tag{3.38a}$$

$$\omega_{gg'}=4\pi Bc(2J_g+3)+i\Gamma_{gg'}, \qquad (\Delta J=-2) \tag{3.38b}$$

Notice that in Eq. (3.37) we really need consider only the Raman frequencies for either positive or negative values of ΔJ, since terms with positive and negative ΔJ are equivalent. For linear molecules (K=0) Eq. (3.37) simplifies to

$$\chi(t)=\frac{N}{i\hbar}\sum_J \frac{1}{5}\left(\rho_{J'}-\rho_J\right)e^{\omega_{JJ'}t}\left(\alpha_{\parallel}-\alpha_{\perp}\right)^2\frac{(J+1)(J+2)}{2J+3}, \tag{3.39}$$

where J'=J+2. No $\Delta J=1$ transitions are allowed for linear molecules. Eq. (3.39) is similar to that derived by Lin *et. al.*[7] using a phenomenological approach.

In the high temperature limit ($kT >> \Delta E$), one can set $\tilde{D}^{2*}_{0\ell}=D^{2*}_{0\ell}$. The matrix elements of Eq. (3.37) can then be rewritten in terms of the spherical harmonics and evaluated using the spherical harmonic addition theorem[16] to give

$$\left\langle D^{2*}_{00}(0)D^{2*}_{00}(t)\right\rangle=\left\langle P_2(\cos\theta(t))\right\rangle, \tag{3.40}$$

where $\theta(t)$ is the angle between the molecular axis at time t and at time 0. The molecular response is therefore

$$\chi(t) = -\frac{N}{3kT}\left(\alpha_{\parallel} - \alpha_{\perp}\right)^2 \frac{d}{dt}\left\langle P_2(\cos\theta(t))\right\rangle. \qquad (3.41)$$

When the rotation is treated classically, the orientational average of the response in Eq. (3.41) reduces to the expression given previously by Cho *et. al.* (see Eq. 4.15 ref. 10). Note that the spherical harmonic addition theorem does not apply to asymmetric tops, because more than one angle is needed to define the orientation of an asymmetric top.

It is interesting to point out that for times shorter than the characteristic recurrence period, the molecular response can be described equally well using either a quantum or classical expression. In fact, it can be easily shown that if Eq. (3.41) is evaluated classically for rigid rotors it reproduces the quantum mechanical results until the first recurrence. The reason for this can be understood from Ehrenfest's theorem,[29] which implies that the center of the quantum wavepacket moves classically so long as the wavepacket is localized. Therefore, in this sense the quantum and classical descriptions are equivalent for short time scales, before significant spreading of the wavepacket occurs. However, only the quantum expression predicts the experimentally observed RIPS recurrences which occur in low density gases long after the initial dephasing.

The quantum result (Eq. (3.37)) shows that the RIPS molecular response is a discrete Fourier transform, with frequencies uniquely determined by the rotational constants of the molecule. From Eq. (3.38a) we see that the Fourier sum associated with the $\Delta J=1$ transitions produces identical transients occurring at delay times separated by $1/2Bc$. The $\Delta J=2$ transitions give transients every $1/4Bc$, but only every other transient has the same shape. This is due to the J-independent term, which has a period of $1/6Bc$. The overall period for the $\Delta J=2$ term is therefore $1/2Bc$.

The molecular response is dominated by the $\Delta J = 2$ transitions, since the value of the 3j symbols for these transitions scales as $1/J^{1/2}$, whereas those associated with the $\Delta J=1$ go as $1/J^{3/2}$. Note that the projection of angular momentum along the symmetry axis

does not change ($\Delta K=0$ in Eq. (3.37)) during any of the symmetric top transitions. Also, $K = 0$ for a linear molecule, so that only the $(J' - J) = \pm 2$ transitions are allowed. For spherical molecules there is no RIPS response, since the polarizability is isotropic $(\alpha_{\parallel} - \alpha_{\perp} = 0)$.

Nuclear spin statistics can modify the periodicity by systematically alternating $(\rho_{g'} - \rho_g)$ in Eq. (3.37). For example, Fig. 3 shows experimental and simulated spectra for CO_2 at 300 Torr in the heterodyne limit. In the simulation we set $B = 0.3902$ cm^{-1}, $D = 13.5 \times 10^{-8}$ cm^{-1},[26] and assume a 100 fs pump pulse, 180 fs probe pulse, and a room temperature (298K) Boltzmann distribution for the rotational state populations. Notice that CO_2 is missing every other rotational level, causing peaks to occur every 1/8Bc (≈ 10.7 ps) in the RIPS spectrum instead of every 1/4Bc. The experimental spectrum of N_2 at 300 Torr shown in Fig. 3.4 also has peaks every 1/8Bc, even though N_2 has no "missing" rotational states. Rather, the small peaks occurring at odd multiples of 1/8Bc are a manifestation of the two to one weighting of even over odd J states.

The expressions for the Raman frequencies (Eqs. (3.38a,b)) must be modified to accurately model the spectrum, especially for longer pump-probe delay times, due to the effects of intra- and intermolecular interactions. The major source of the intramolecular dephasing for small molecules such as CO_2 is centrifugal distortion, which modifies the Raman frequencies ($\omega_{gg'}$) of Eqs. (3.38a,b) by adding a term $\left(-DJ^2(J+1)^2\right)$ to the rotational energies. This destroys the otherwise integral relationship of the Raman frequencies, resulting in a reshaping and a spreading of the recurrences in the time domain that becomes more pronounced as the pump-probe delay increases. The effects of centrifugal distortion can become significant even for short delay times if the temperature is high enough. For example, in Fig. 3.3 the asymmetry of the recurrences at 10.7 and 32 ps is due to the centrifugal distortion.

Although we will mainly be interested in using RIPS to understand molecular dynamics, the technique can be used to measure spectroscopic constants with high

precision. These constants are well known for the small molecules discussed here, but for larger molecules having congested frequency domain spectra, RIPS can be a useful technique in helping to elucidate the molecular structure. As mentioned earlier, several groups have successfully used other RCS techniques to determine molecular structure.

The level of precision in determining spectroscopic constants from RIPS spectra depends upon the length of time delay over which scans are taken, with longer time domain spectra allowing a better determination of the constants. For example, the error in measuring B can be roughly determined by

$$\frac{\delta B}{B} \propto \frac{\delta t}{N T_0}$$

where δt is the uncertainty in measuring the time to the Nth recurrence, and T_0 is the time between recurrences (=1/8Bc for CO_2). The precision in measuring B is actually somewhat better than stated above, since we can measure delays to the other N-1 recurrences as well. In the limit where the distance to each recurrence is NT_0, the uncertainty in B would decrease as $(1/N)^{3/2}$, since we would then have N identical measurements. Presumably, the uncertainty in time is primarily due to the finite laser pulse width. Therefore, assuming a δt=100 fs and assuming we take a spectrum out to 100 ps, the constant for a small molecule like N_2 ($B \approx 2$ cm^{-1}) could be measured to better than 0.001 cm^{-1}.

The uncertainty in higher order constants such as the distortion constant, D, is more difficult to quantify. However, empirically it was found that for N_2 and O_2 this constant could be determined to $\pm$20% from scans of 150 ps. Likewise, it was possible to determine the electronic spin-spin splitting constant of O_2 (λ=1.985 cm^{-1}) to $\pm$10% from such spectra.

3.32 Asymmetric Tops (O_3)

In contrast to the symmetric top case, the rotational matrix elements of Eq. (3.35) for an asymmetric top cannot be further simplified after orientational averaging. The response of a near-symmetric top, however, should be similar to that of a symmetric top, given in Eq. (3.37). For example, one could expect to obtain fairly good results by approximating the rotational wavefunctions as symmetric top rotational states and using accurate asymmetric top rotational energies to calculate the Raman frequencies ($\omega_{gg'}$) in Eq. (3.37). This is analogous to using zero order wavefunctions and first order energies in stationary perturbation theory.

Fig 3.5 shows a comparison of experimental O_3 results with a simulation based on the method described above. The middle curve (b) in the figure is an experimental O_3 RIPS heterodyne spectrum taken at 120 Torr. The top curve (a) is the simulated spectrum, which assumes a 100 fs pump pulse, a 180 fs probe, and a 298K Boltzmann distribution for the rotational state populations. The rotational Raman frequencies were calculated using spectroscopic constants found in the literature.[30] Additionally, the simulation accounts for a small amount of O_2 ($\approx 5\%$) present during the experimental scan.

There is remarkable agreement between the two curves. In particular, the spectra show recurrences at times given approximately by $n/4(B+C)c \cong n/8Bc$ (≈ 9.9 ps), with the small peaks at $t \approx (2n+1)/8Bc$ due to nuclear spin statistics. The asymmetry of O_3 is manifested in the spreading of the later recurrences. Compared to symmetric tops the individual recurrences contain more peaks over a broader delay time. The recurrences are also less symmetric compared to CO_2. In addition, there is a corresponding decrease in the intensity of the later peaks relative to the initial peak near t=0 in O_3 versus CO_2 (compare Figs. 3.3 and 3.5). These characteristics of the spectrum point to the fact that, in addition to collisional and centrifugal dephasing, the irregularity of the asymmetric top energy level

spacings themselves contribute an additional dephasing mechanism in the time-domain spectrum of these molecules.

Although the approximation discussed above gives results that are in fairly good agreement with experiments, there are minor discrepancies between the experimental and simulated spectra. This can be remedied by using perturbation theory to expand the asymmetric top rotational wavefunctions to first order in a symmetric top basis:

$$|J,\Omega\rangle = A_K(E,J)|JKM\rangle + A_{K+2}(E,J)|JK+2M\rangle + A_{K-2}(E,J)|JK-2M\rangle, \qquad (3.42)$$

where we explicitly include the dependence of the expansion coefficients on E to distinguish between states with the same J but different energy. The approximation in Eq. (3.42) is good if $A_K(E,J) >> A_{K\pm2}(E,J)$. The polarizability matrix elements are then given by

$$\left|\left[\alpha_0^{(2)}\right]_{g'g}\right|^2 = \sum_{K,K',K'',K'''}\sum_{\ell,\ell'}\langle G|\alpha_\ell'^{(2)}|G\rangle\langle G|\alpha_{\ell'}''^{(2)}|G\rangle\frac{1}{5}(2J+1)(2J'+1)\times$$
$$\left(A_K(E,J)A_{K'}(E',J')A_{K''}(E',J')A_{K'''}(E,J)\right)\begin{pmatrix} J' & J & 2 \\ K' & -K & \ell \end{pmatrix}\begin{pmatrix} J & J' & 2 \\ K''' & -K'' & \ell' \end{pmatrix} \qquad (3.43)$$

It can be seen that terms involving $\ell,\ell' = 0,\pm2$ and $\Delta J = 0,\pm1,\pm2$ contribute. There are no terms with $\ell,\ell' = \pm1$, since the perturbation only couples states in which the K's differ by an even integer (see Eq. (3.42)).

If each asymmetric rotational wavefunction is written as in Eq. (3.42), there will be $3^4 = 81$ terms for each transition in Eq. (3.43). Of these, the symmetric top term ($K = K' = K'' = K'''$) will be the most important one. The next largest terms will be those in which three of the K's are the same, i.e.

$$\sum_{K}\sum_{\ell,\ell'}\frac{1}{5}(2J+1)(2J'+1)\langle G|\alpha_0^{\prime(2)}|G\rangle\langle G|\alpha_{\mp2}^{\prime(2)}|G\rangle\begin{pmatrix}J' & J & 2\\ K-K & 0\end{pmatrix}A_K(E,J)A_K(E',J')A_K(E',J')\times$$
$$\left\{A_{K\pm2}(E,J)\begin{pmatrix}J & J' & 2\\ K\pm2 & -K & \mp2\end{pmatrix}+A_{K\mp2}(E,J)\begin{pmatrix}J & J' & 2\\ K & -(K\mp2) & \mp2\end{pmatrix}\right\} \tag{3.44}$$

For a near-symmetric top, there are four of these terms (each of which occurs twice in Eq. (3.43), for a total of eight) that contain three of the larger expansion coefficients and one smaller coefficient. Neglecting differences in the 3j symbols, these four different terms are smaller than the main one by a factor of

$$\frac{1/2\left(\alpha_{xx}-\alpha_{yy}\right)A_{K\pm2}(E,J)}{\sqrt{2/3}\left(\alpha_{zz}-\alpha_{xx}\right)A_K(E,J)},$$

where we have used $\alpha_{\pm2}^{\prime(2)}=1/2\left(\alpha_{xx}-\alpha_{yy}\right)$.[16] For a near-symmetric top it is expected that $\left(\alpha_{xx}-\alpha_{yy}\right)<\left(\alpha_{zz}-\alpha_{xx}\right)$, however the ratio of the two may vary significantly from molecule to molecule. The ratio $A_{K\pm2}(E,J)/A_K(E,J)$, on the other hand, is determined by the asymmetry parameter $\kappa\equiv(2B-A-C)/(A-C)$. In molecules with $|\kappa|\geq0.95$, the ratio of these coefficients is small for fairly low-lying rotational states. For example in ozone, a near-prolate top (A=3.55 cm^{-1}, B=0.445 cm^{-1}, C=0.394 cm^{-1})[30] with $\kappa=-0.97$, the ratio of these coefficients is less than 0.1 for most of the thermally populated J states.

The next largest terms in Eq. (3.43) have two relatively small expansion coefficients ($A_{K\pm2}$), and are thus smaller than the symmetric top term by approximately another factor of ten. These terms and terms that contain three or four $A_{K\pm2}$ coefficients can be ignored relative to the five terms mentioned above, so long as $|\kappa|$ is on the order of 0.95 or larger. For molecules which are more asymmetric, one would have to use higher

orders of perturbation theory and include more terms from the expansion, or else diagonalize the Hamiltonian matrix to find the expansion coefficients of Eq. (3.43).

The bottom curve (c) in Fig. 3.5 shows a simulation for O_3 using the perturbative approach outlined above. In the simulation we used the theoretically calculated value of $(\alpha_{xx} - \alpha_{yy})/(\alpha_{zz} - \alpha_{xx}) = 0.15$ from reference 31, which results in excellent agreement between the simulated and experimental spectra. We find that this value of $(\alpha_{xx} - \alpha_{yy})/(\alpha_{zz} - \alpha_{xx})$ can be varied by as much as 50% without significantly distorting the spectrum for pump-probe delay times up to 45 ps. Matching the experimental spectrum at longer delay times would most likely allow less latitude in the variation of this ratio.

3.4 Collisional Decay

The intensity of the RIPS recurrences decays with time due to intermolecular interactions, i.e. collisions. A collision can be thought of as adding a random phase shift to a rotating molecule, causing it to fall out of the coherent ensemble. At low pressures the decay of the recurrences can be adequately accounted for phenomenologically using complex, instead of real, Raman frequencies (Eqs. (3.38)), giving an exponential decay of the signal in time.

Such a decay is displayed in Fig. 3.6, which shows a homodyne spectrum of O_2 at 520 Torr measured over a period of 200 ps. For clarity only every fourth recurrence is shown. A good fit to the data is obtained assuming a J-independent $\Gamma_{g'g} = 5.7 \pm 0.3$ ns^{-1}. The corresponding cross-section (σ) of 75 ± 4 Å^2 is much larger than the hard sphere cross-section of 40 Å^2.[32] It is, however, consistent with that obtained by thermal averaging of rotational Raman line widths from Berard *et al.*,[33] which gives σ=71 Å^2. In that experiment, the authors determined that the line widths were almost entirely due to inelastic collisions.

We have also measured a decay constant of 6.5 ± 0.3 ns^{-1} for 530 Torr of N_2, corresponding to $\sigma = 52 \pm 3$ Å^2. This agrees with the thermally averaged value of 0.55 nm^2 measured in the stimulated Raman gain experiments of Herring et. al.[34] It is also in agreement with the thermal average of rotational energy transfer rates measured by Sitz and Farrow for J = 2-14 levels of the vibrationally excited state (v=1),[35] suggesting that the RIPS polarization decay is due mainly to inelastic collisions.

Finally, RIPS spectra of CO_2 at 100 and 500 Torr were fit using J-independent decay constants to obtain a cross section of 127 ± 6 Å^2. This is close to the value of 145 Å^2 deduced from averaging spontaneous Raman line width measurements made by Herpin and Lallemand[36] at a somewhat higher pressure of 2.8 bar.

The exponential character of the RIPS decay at these low pressures suggests that the collisional dephasing is not strongly J-dependent. In fact, we have tried to fit our data assuming $\Gamma_{g'g}$ depends exponentially on $\Delta E_{g'g}$ (energy-gap law). It was found that the Γ's for J = 1 and J = 11 can differ by no more than 20% without distorting the shape of the transients at later time.

The results mentioned above confirm that frequency domain and real time experiments can provide similar dynamical information. The frequency domain spectra are more convenient to perform at low pressure, where spectral lines are narrow and well resolved. To get the same information from time domain experiments requires scanning over hundreds of picoseconds, since at low densities the infrequent molecular interactions take a long time to manifest themselves. On the other hand, at higher pressures the faster dynamics lead to broad overlapping lines in the frequency domain, making linewidth measurements more difficult. Time domain measurements are better suited to studying this high density regime. RIPS results in high pressure CO_2 will be discussed in the next chapter.

References

1. Y.R. Shen, *The Principles of Nonlinear Optics*, (Wiley, New York, 1984).

2. M.D. Levenson, *Introduction to Nonlinear Laser Spectroscopy*, (Academic Press, New York, 1982).

3. J.J. Sakurai, *Modern Quantum Mechanics*, (Addison-Wesley, New York, 1985), p.318.

4. G.L. Eesley, M.D. Levenson, and W.M. Tolles, IEEE J. Quant. Elect. **14**, 45 (1978).

5. J. Chesnoy and A. Mokhtari, Phys. Rev. A **38**, 3566 (1988).

6. Y.J. Yan, L.E. Fried, and S. Mukamel, J. Phys. Chem. **93**, 8149 (1989).

7. C.H. Lin, J.P. Heritage, T.K. Gustafson, R.Y. Chiao and J.P. McTague, Phys. Rev. A **13**, 813 (1976).

8. Y.J. Yan and S. Mukamel, J. Chem. Phys. **94**, 997 (1991).

9. M. Schubert and B. Wilhelmi, *Nonlinear Optics and Quantum Electronics*, (John Wiley ans Sons, New York, 1986), p.209.

10. M. Cho, M. Du, N.F. Scherer, G.R. Fleming, and S. Mukamel, J. Chem. Phys. **99**, 2410 (1993).

11. L.D. Ziegler, R. Fan, A.E. Desrosiers, and N.F. Scherer, J. Chem. Phys. **100**, 1823 (1994).

12. D. Waldeck, A.J. Cross, Jr., D.B. McDonald, and G.R. Fleming, J. Chem. Phys. **74**, 3381 (1981).

13. M. Cho, G.R. Fleming, and S. Mukamel, J. Chem. Phys. **98**, 5314 (1993).

14. A.B. Myers and R.M. Hochstrasser, IEEE J. Quantum Electron. **QE-22**, 1482 (1986).

15. D.S. Alavi, R.S. Hartman, and D.H. Waldeck, J. Chem. Phys. **92**, 4055 (1990).

16. R.N. Zare, *Angular Momentum*, (Wiley, New York, 1988).

17. J.M. Brown, and B.J. Howard, Mol. Phys., **31**, 1517 (1976); **32**, 1197 (1976).

18. D.A. McQuarrie, *Statistical Mechanics*, (Harper Collins, New York, 1976).

19. D.A. Long, in *Non-Linear Raman Spectroscopy and Its Chemical Applications*, edited by W. Kiefer and D.A. Long (D. Reidel, Holland, 1982).

20. L.D. Barron and E. Norby Svendsen, in *Advances in Infrared and Raman Spectroscopy*, edited by R.J.H. Clark and R.E. Hester (Heyden & Son Ltd., London, 1981), vol. 8.

21. Y.-X. Yan, L.-T Cheng, and K.A. Nelson, *Advances in Non-linear Spectroscopy*, edited by R.J.H. Clark and R.E. Hester (Wiley, New York, 1987), p 299; S. Ruhman, B. Kohler, A.G. Joly, and K.A. Nelson, IEEE J. Quantum Electron. **QE-24**, 470 (1988).

22. W.T. Pollard, C.H. Brito-Cruz, C.V. Shank, and R.A. Mathies, J. Chem. Phys. **90**, 199 (1989).

23. W.T. Pollard, S.Y. Lee, and R.A. Mathies, J. Chem. Phys. **92**, 4012 (1990).

24. W.T. Pollard, S.L. Dexheimer, Q. Wang, L.A. Peteanu, C.V. Shank, and R.A. Mathies, J. Phys. Chem. **96**, 6147 (1992).

25. We use the well-known relation $\frac{i}{\hbar}\left\langle \hat{A}(t)\hat{B}(0) - \hat{B}(0)\hat{A}(t)\right\rangle = \frac{1}{kT}\frac{d}{dt}\left\langle \tilde{B}(0)\hat{A}(t)\right\rangle$, see e.g. ref. 19 p. 495.

26. G. Herzberg, *Molecular Structure and Molecular Spectra, III. Electronic Spectra and Electronic Structure of Polyatomic Molecules*, (Van Nostrand Reinhold, New York, 1966).

27. N.F. Scherer, D.M. Jonas, and G.R. Fleming, J. Chem. Phys. **99**, 153 (1993).

28. R.M. Bowman, M. Dantus, and A.H. Zewail, Chem. Phys. Lett. **161**, 297 (1989).

29. C. Cohen-Tannoudji, B. Diu, and F. Laloe, *Quantum Mechanics*, Vol. 1 (John Wiley & Sons, New York, 1977), p.243.

30. M. Bellini, P. De Natale, G. Di Lonardo, L. Fusina, M. Inguscio, and M. Prevedelli, J. Mol. Spec. **152**, 256 (1992).

31. G. Maroulis, J. Chem. Phys. **101**, 4949 (1994).

32. G.W.C. Kaye and T.H. Laby, *Tables of Physical and Chemical Constants* (Longman, London, 1973).

33. M. Berard and P. Lallemand, J. Chem. Phys. **78**, 672 (1983).

34. G.C. Herring, M.J. Dyer, and W.K. Bischel, Phys. Rev. A **34**, 1944 (1986).

35. G.O. Sitz and R.L. Farrow, J. Chem. Phys. **93**, 7883 (1990).

36. M.-C. Herpin and P. Lallemand, J. Quant. Spectrosc. Radiat. Transfer **15**, 779 (1975).

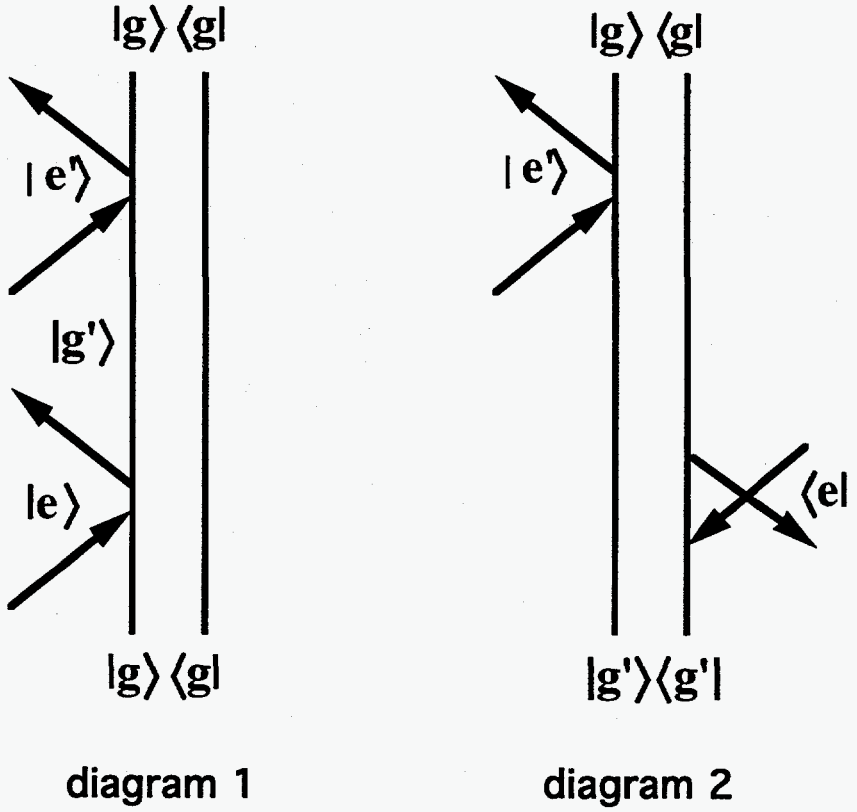

Fig. 3.1. Double sided Feynman diagrams that, with their mirror images, account for the RIPS process. States g and g' are in the ground vibronic manifold. Excited virtual states are represented by e, e'. Ket time evolution is represented on the left, and bra evolution on the right of the diagrams. Time increases from bottom to top in the diagrams. In both diagrams the first two interactions with the pump laser field leaves the molecule in a coherent superposition state represented by the off diagonal density matrix elements $|g'\rangle\langle g|$. Two interactions with the second laser field probes the coherence, in the process reforming stationary states given by the density matrix elements $|g\rangle\langle g|$.

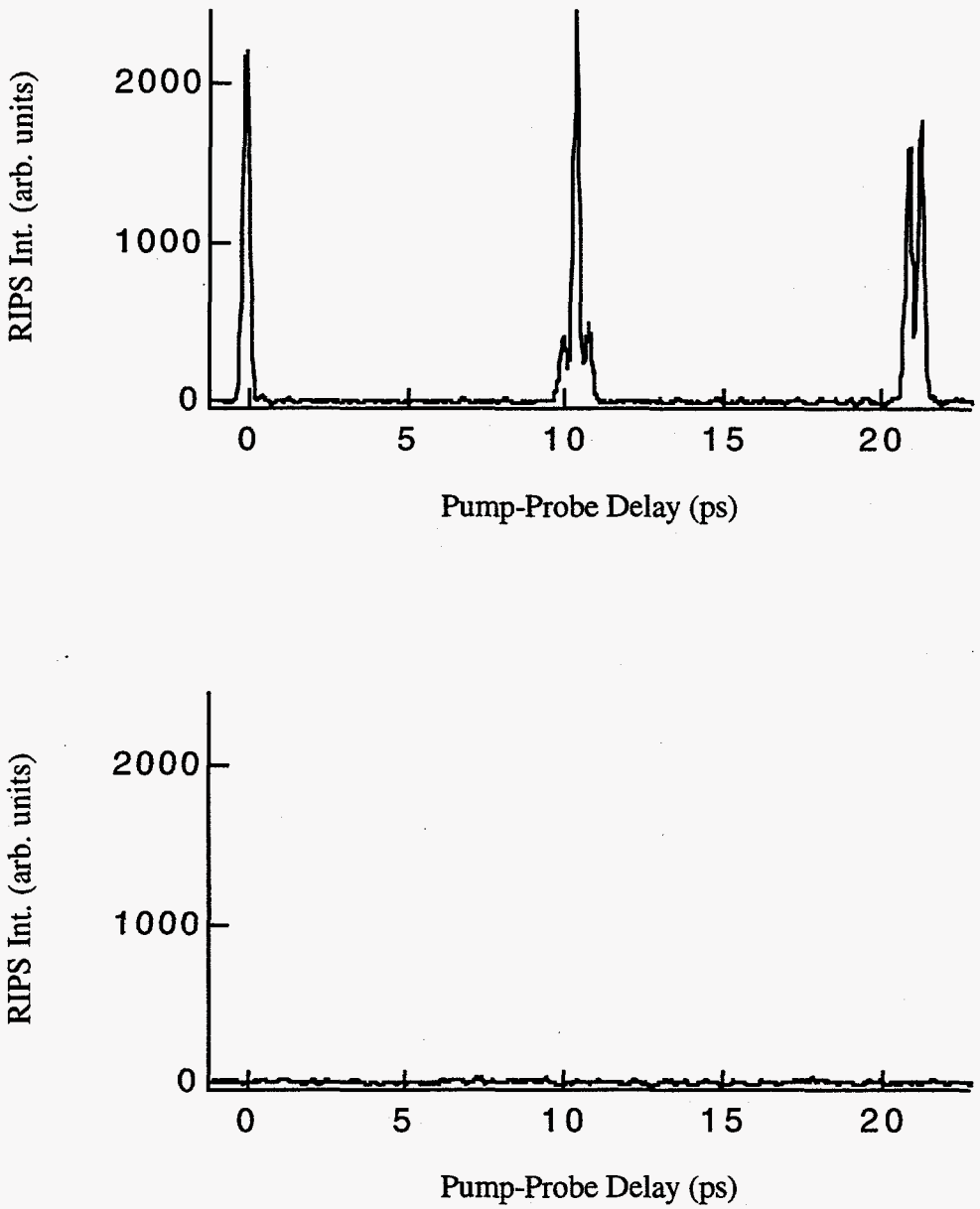

Fig. 3.2. Experimental RIPS homodyne spectrum for 200 Torr CO_2 using (a) a linearly and (b) a circularly polarized pump pulse. Ground state dynamics are not observed in (b) due to a vanishing $\alpha^{(1)}$.

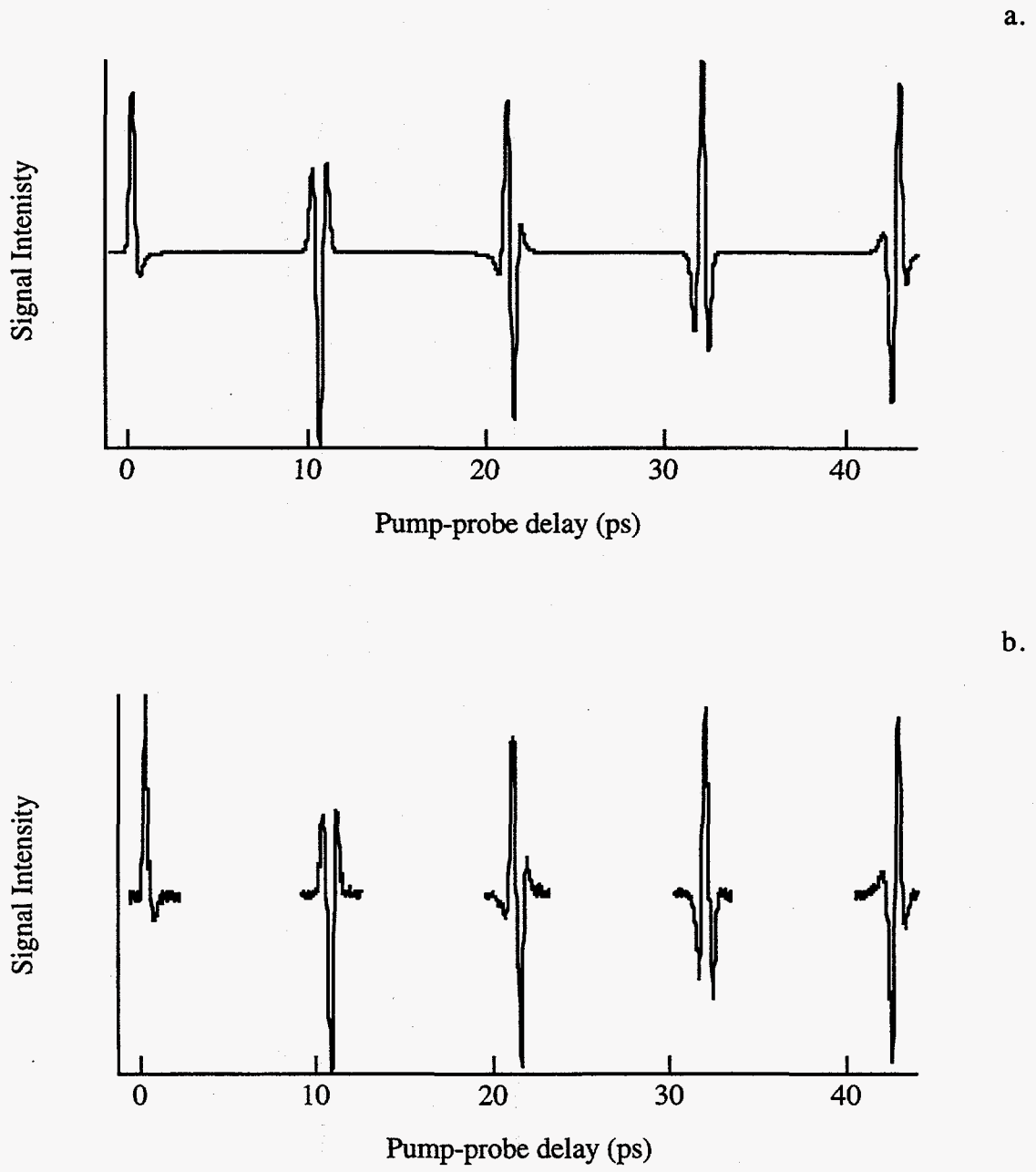

Fig. 3.3. (a) Simulated and (b) experimental CO_2 RIPS spectrum. Experimental spectrum was taken with 300 Torr CO_2. The simulation uses B=0.3902 cm^{-1}, D=13.5 x 10-8 cm^{-1}, and assumes a 100 fs pump pulse width, 180 fs probe pulse width, and a 298 K sample temperature.

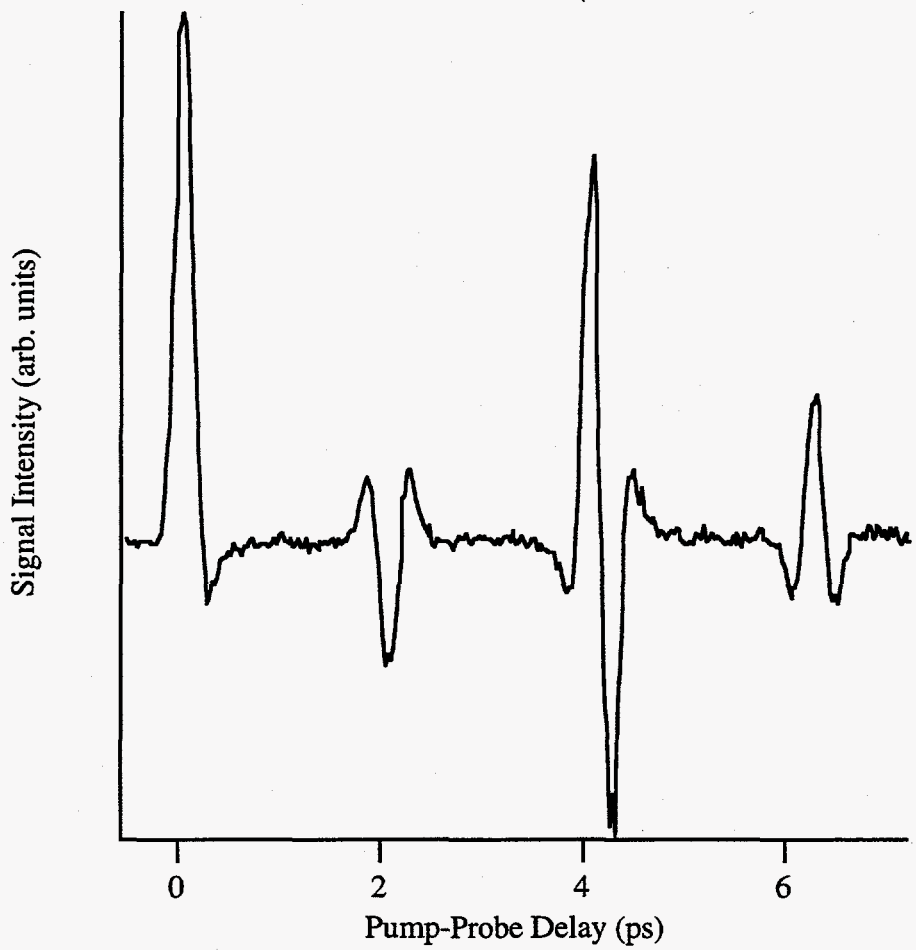

Fig. 3.4. Experimental RIPS spectrum for N_2 at 300 Torr. The appearance of small recurrences at odd multiples of 1/8Bc (at approximately 2 and 6 ps) result from the unequal weighting of even and odd rotational states.

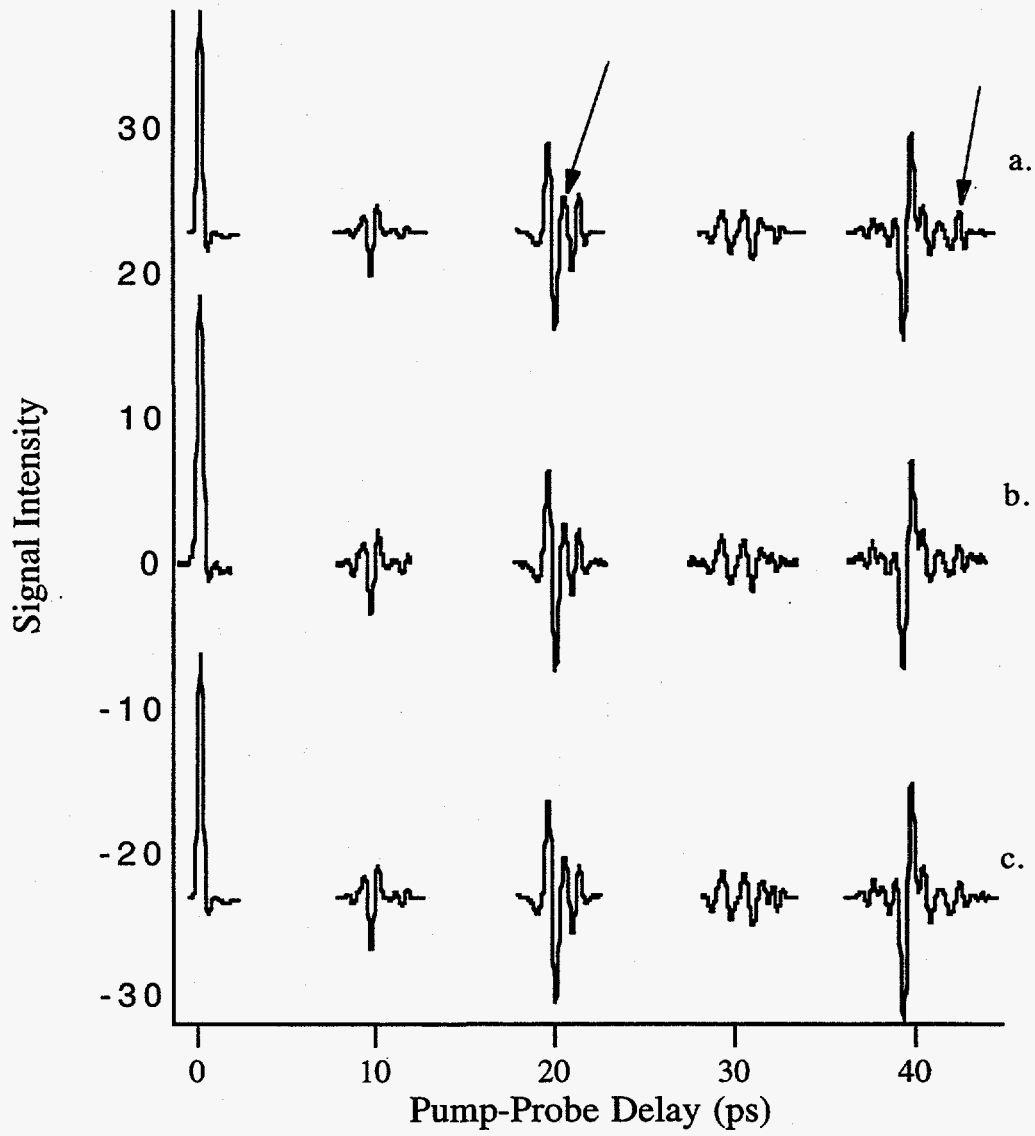

Fig. 3.5. (a), (c) Simulated and (b) experimental O_3 RIPS spectrum. Experimental spectrum was taken with 120 Torr O_3. The simulation in (a) uses spectroscopically determined frequencies, but approximates the transition matrix elements with those of a symmetric top; (c) same frequencies as in (a), but the matrix elements are evaluated using first order perturbation theory. The discrepancies in (a) marked by arrows are not present in (c).

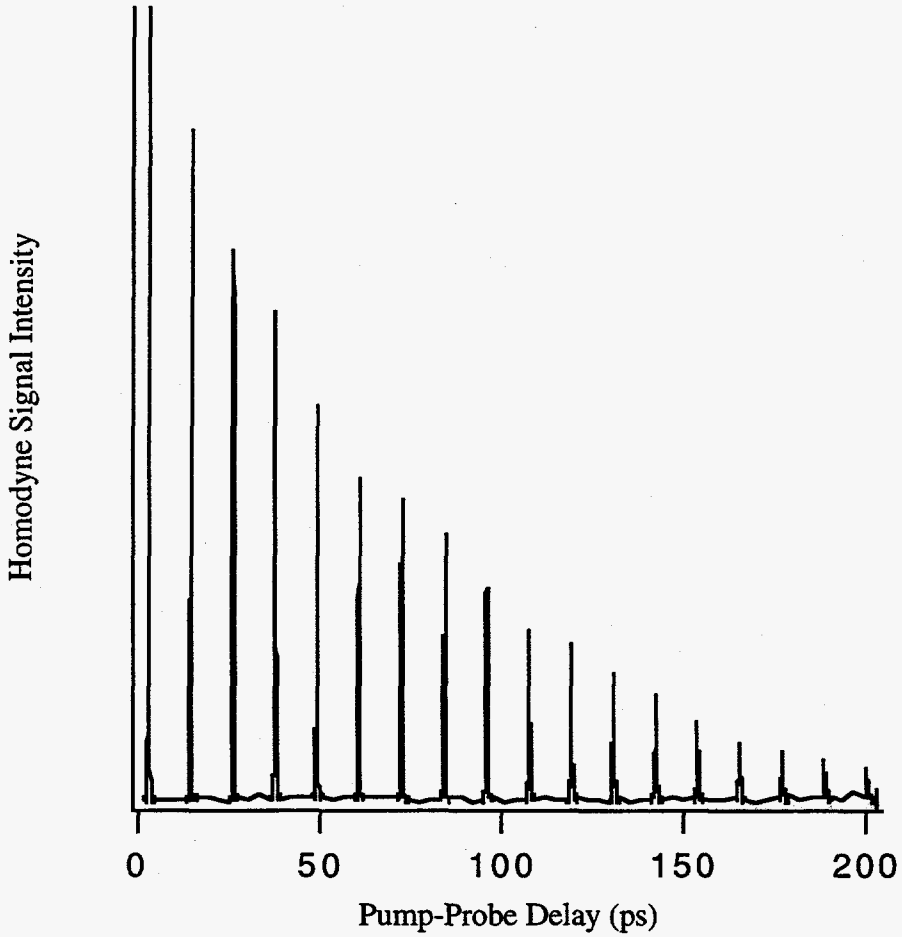

Fig. 3.6. Experimental RIPS homodyne spectrum for 520 Torr O_2 (only every fourth recurrence is shown). The spectrum is fit using a rotational dephasing constant of Γ=5.7 ns^{-1}.

Chapter 4

High Pressure Carbon Dioxide

4.1 Introduction

In this chapter RIPS results for high density CO_2 gas and liquid (5 to $\approx$63 atm) are presented. The motivation behind these experiments is to understand how the orientational dynamics evolve as the density is increased. It is known that in the low density limit the molecules behave as isolated free quantum rotors that do not interact with one another. In the liquid, meanwhile, we have the opposite extreme in which the molecules are essentially always within the sphere of influence of their neighbors, and the rotational motion can often be described using a classical diffusion model. Between these two limits lies a wide density regime where collisions play an important role in determining the rotational dynamics. The question is, how do collisions affect the evolution of the rotational motion in going from the rare gas to the liquid?

In order to answer this question, we have focused our experiments on high pressure CO_2 gas. It is at the intermediate densities of the high pressure gas where collisions become frequent enough that they strongly influence the reorientational motion, but are still infrequent enough to be considered independent, discernible events. It is hoped that these experiments will lead us to a more complete and consistent picture of how collisional interactions shape the dynamics over the entire fluid density range.

We chose CO_2 for these studies, in part, because both the vapor and liquid phases are accessible at room temperature and moderate pressures. Also, as a small linear molecule, its rotational dynamics should be less complicated than those of larger, less symmetric molecules. Finally, because it is small, CO_2 also rotates relatively quickly, and

therefore its rotational recurrences provide a more precise "clock" for the experiments than those of large, slowly rotating molecules.

Some information concerning the rotational dynamics of CO_2 in the gas and liquid phases can be obtained through analysis of collisionally broadened line widths in various frequency domain light scattering experiments. For example, it has been suggested[1,2] that rotational Raman line widths largely reflect inelastic collision times. The S branch line widths have been measured for CO_2 at relatively low pressure by Jammu et. al.[3] (5, 9 atm) and by Herpin and Lallemand[4] (2.8 bar). Similarly, Boquillon has measured the CARS line widths at very low pressure[5] (37.5 Torr).

In contrast to the rotational Raman line widths, the broadening of the depolarized Rayleigh spectrum is expected to be quite sensitive to elastic reorienting collisions.[1,2] Depolarized Rayleigh (rotationally elastic) scattering experiments for CO_2 gas at low densities have been reported by Cooper et. al.[6] (1-5 atm) and Keijser et. al.[7] (2-12 atm), while Versmold[8] has obtained Rayleigh results at higher densities ranging from 2 to 1000 bar. In addition, several experimental[9,10] and molecular dynamics[11,12] studies of light scattering in liquid CO_2 have been reported, from which orientational correlation functions have been obtained.

Finally, ^{13}C NMR experiments are another source of information for the orientational dynamics in CO_2,[13] since the relaxation time for the ^{13}C nucleus is determined by the spin-rotational coupling.[2,13] Like RIPS, these experiments cannot directly measure dynamics associated with individual rotational states, as all rotational levels contribute to a single relaxation time. The NMR studies are complimentary to RIPS, since the NMR relaxation time is more strongly influenced by the higher J levels than is RIPS. In fact, the NMR signal depends on J^2,[2] while RIPS scales linearly with J.

To our knowledge CO_2 rotational dynamics have not been studied previously using time resolved scattering experiments. However, many time resolved polarization

experiments have been done on liquid CS_2,[14-17] in which the rotational motion appears to be governed by classical diffusion.

In this chapter we demonstrate that RIPS provides information about both elastic and inelastic collisions, and is therefore complimentary to the frequency domain scattering techniques. As mentioned in Chapter 1, RIPS offers some advantages over frequency domain techniques, especially at high density where molecular interactions are more frequent and the dynamics are quite fast. It has been pointed out previously[18] that time domain methods are well suited to observing these very fast dynamics. For one thing, relaxation rates can be measured directly in the time domain, without the complication of attempting to Fourier transform a noisy signal convoluted with an instrumental response function from the frequency domain to the time domain. We show here that RIPS can be used to simultaneously record both the elastic and inelastic scattering spectrum over a wide density range with very high signal to noise.

What we find is that as the density is increased, both qualitative and quantitative changes occur in the RIPS spectrum due to more frequent intermolecular interactions. Some of the changes can be explained within the framework of the phenomenological decay model for the rotational dynamics introduced in Chapter 3. However, at the highest densities studied, this model is replaced by the J diffusion model, which more accurately reflects the slowing of the initial dephasing due to collisions. At intermediate densities between approximately 400 and 800 psi, neither model adequately accounts for the complete experimental response. The RIPS results suggest the need for an improved model that can simultaneously account for the distinct time scales of the dynamics associated with the elastic and inelastic collisions, as well for the onset of diffusional reorientation in the mid density regime. In addition, a successful model should also give the correct results in both the high and low density limits.

4.2 Phenomenological Decay Model

4.21 Pressure to Density Conversion

Before discussing the results, we note that at the higher pressures discussed in this chapter the pressure and density are not proportional to one another. Since the molecular collision frequency depends on density, pressures were converted to density by solving the Kammerlingh Onnes virial expansion[19]

$$\rho + b\rho^2 + c\rho^3 = \frac{P}{RT}, \tag{4.1}$$

using the Newton-Raphson approximation.[20] In Eq. (4.1) ρ is the number density, P is the pressure, R is the ideal gas constant, T is the temperature, and b and c are the second and third virial coefficients, respectively. For CO_2 b=-124.9 cm^3/mole and c=4363 $cm^6/mole^2$.[21] Eq. (4.1) was used to obtain densities for all pressures except those at the liquid/vapor equilibrium, where the virial equation was abandoned in favor of published values for the fluid density.[22] The densities are expressed in units of amagat, where one amagat is the ideal gas density at STP (1 amagat=2.687×10^{19} molecules/cm^3). The relationship of density to pressure for CO_2 at 295 K is shown in Fig. 4.1.

4.22 Additional Scattering Response at High Densities

Fig. 4.2a shows the RIPS spectrum of CO_2 at 25.9 amagat (355 psi). As expected, the rotational recurrences in this spectrum decay much more quickly than at lower pressure due to a higher collision frequency (compare Fig. 4.2 with the 300 Torr spectrum in Fig. 3.3). However, the enlarged view of the 25.9 amagat data displayed in Fig. 4.2b shows

another important difference. A broad peak appears in this high pressure spectrum which was not observed in the low pressure data. This feature is caused by elastic, or J to J scattering, and can only be seen at higher densities. The origin of the response from these diagonal transitions and the reason for its observance at higher densities can be understood by reexamining the molecular susceptibility of Eqs. (3.31, 3.34):

$$\chi(t) = \frac{N}{2kT}\frac{d}{dt}\left\langle [\tilde{\alpha}(0)]_0^{(2)} [\alpha(t)]_0^{(2)} \right\rangle \tag{4.2}$$

where we have written the polarizability tensors in the laboratory frame. In the classical limit this response reduces to the time derivative of the polarizability autocorrelation function. It should be recalled that in the previous chapter the collisional decay of the recurrences was accounted for by adding a phenomenological damping term to the Raman frequencies. The effect of this was to give an exponential decay to the *derivative* of the free rotor correlation function.

There is perhaps a more consistent way of treating the effects of collisions. It will be recalled that our initial results in Chapter 3, which were derived in the collisionless limit, showed that the molecular response is given by the derivative of the correlation function. It is reasonable to expect that the response is also given by the derivative of the correlation function when collisions *do* occur. A simple model for such a correlation function would be an exponentially damped free rotor model, where the damping is a manifestation of collisions that prevent some molecules from rephasing at later recurrence times. The derivative of the damped correlation function would then give two terms:

$$\frac{d}{dt}\left\langle [\tilde{\alpha}(0)]_0^{(2)} [\alpha(t)]_0^{(2)} e^{-\gamma t} \right\rangle = -\left\langle e^{-\gamma t} \frac{d}{dt}([\tilde{\alpha}(0)]_0^{(2)} [\alpha(t)]_0^{(2)}) \right\rangle + \left\langle \gamma [\tilde{\alpha}(0)]_0^{(2)} [\alpha(t)]_0^{(2)} e^{-\gamma t} \right\rangle \tag{4.3}$$

The first term is the one we considered in the previous chapter. The second term can be analyzed in a manner analogous to that presented in Chapter 3 for the first term (see the analysis above Eq. 3.37).

Note that there are two parts to the second term of Eq. 4.3, one for $|\Delta J|=1,2$ transitions, and one for $\Delta J=0$ transitions. The part arising from the $|\Delta J|=1,2$ transitions is very similar in form to the first term of Eq. (4.3), and is essentially given by the time integral of Eq. 3.37. The molecular response associated with this part is

$$\frac{N}{\hbar}\sum{}' \frac{\gamma}{15} e^{-\gamma t}\left(\rho_{g'}-\rho_g\right)\frac{\cos(\omega_{gg'}t)}{\omega_{gg'}}\left(\alpha_\parallel-\alpha_\perp\right)^2(2J+1)(2J'+1)\begin{pmatrix} J' & J & 2 \\ K-K & 0 & \end{pmatrix}^2$$

where we have taken only the real component. The second part of the second term, which is due to transitions diagonal in J ($\Delta J=0$), and therefore has no oscillatory components, is given by

$$\frac{N}{kT}\sum{}' \frac{\gamma}{15}\rho_g\left(\alpha_\parallel-\alpha_\perp\right)^2 e^{-\gamma t}(2J+1)^2\begin{pmatrix} J & J & 2 \\ K-K & 0 & \end{pmatrix}^2$$

where the sum is over all thermally accessible rotational states.

Simplifying the two new parts of the response above for the case of linear molecules and adding the result to the real part of our low pressure term from Chapter 3 gives the total molecular response:

$$\chi(t)=\frac{N}{\hbar}\sum_J \frac{1}{5}\left(\rho_{J'}-\rho_J\right)e^{-\gamma_J t}\left[\sin(\omega_{JJ'}t)+\frac{\gamma_J}{\omega_{JJ'}}\cos(\omega_{JJ'}t)\right]\left(\alpha_\parallel-\alpha_\perp\right)^2\frac{(J+1)(J+2)}{2J+3} \tag{4.4}$$

$$+N\beta\sum_J \frac{\gamma_J'}{15}\rho_J\left(\alpha_\parallel-\alpha_\perp\right)^2 e^{-\gamma_J' t}\frac{J(2J+1)(J+1)}{(2J+3)(2J-1)}$$

where J'=J+2. The decay constants for the diagonal and off diagonal terms have been distinguished as γ'_J and γ_J, respectively, since the decay rates associated with the elastic and inelastic transitions may be different. Note that either of these decay constants may be J dependent, as indicated by the subscripts.

The sine and cosine terms, which are due to off diagonal transitions, give rise to the time domain equivalent of the O and S branches of the Raman frequency domain spectrum. The third term is from elastic scattering and therefore represents the time domain equivalent of the Raman Q branch. The sine and cosine terms are responsible for a fairly sharp initial response peak near zero delay and for the quantum recurrences that occur at later delay times. According to Eq. (4.4) the molecular response from the elastic scattering is simply an exponentially decaying function.

Note that the cosine terms are weighted by the inverse rotational frequencies, $1 / \omega_{JJ'}$, with the result that the low J states make the largest contribution to these terms. Also, since the second and third terms in Eq. (4.4) are linear to the decay constant, they only contribute at relatively high densities where the decay constant becomes large. For CO_2 these terms become significant at pressures higher than about 6-7 amagat ($\approx$ 100 psi).

4.23 Comparison of Phenomenological Model with Experiment

We have successfully modeled the RIPS spectrum of CO_2 up to densities of 25.9 amagat using a J-dependent decay for the off diagonal terms and a J-independent decay for the diagonal terms. The decay of the off diagonal terms was taken to depend exponentially on the ΔJ=2 transition frequency, which is linear in J:

$$\gamma_J = \gamma_0 \exp(-AJ) \tag{4.5}$$

This so called exponential gap model has been used extensively to fit line widths in frequency domain experiments (for an excellent review of this and similar rate scaling models see ref. 23 and references therein). Figs. 4.3 and 4.4 show the fits to data taken at 5.1 and 25.9 amagat. The data at 25.9 amagat was fit using γ_J'=0.34 ps^{-1}, γ_0=0.565 ps^{-1}, and A=0.008. For the 5.1 amagat fit γ_J'=0, γ_0=0.12 ps^{-1}, and A=0.01. In both cases the simulated spectra were smoothed by Gaussian fits to the experimentally measured pump and probe pulse widths.

To obtain better agreement with experiments, a small Gaussian centered at zero time delay was included in the simulations to account for an instantaneous electronic response. The addition of this term is suggested by RIPS spectra of argon gas, which show an instantaneous response having a width approximately equal to the laser cross correlation, whose intensity scales linearly with density. Since the argon atomic nuclear response is forbidden by symmetry, the signal is most likely due to an electronic response, or possibly a two body collision induced signal. Addition of the instantaneous component results in good agreement between the simulations and the experimental spectra.

The decay constants associated with the elastic light scattering can be determined by plotting the log of the signal intensity versus time and fitting the linear portion (between about 2 and 10 ps) to a line. This was done for a range of densities from approximately 16 to 70 amagat, at which point the resolution of the Q-branch from the other branches begins to disappear. Fig. 4.5 shows a plot of the measured decay rates versus density. The rates are linear to density, with a slope of $(1.22\pm.04)\times10^{-2}$ $ps^{-1}amagat^{-1}$, corresponding to an effective collisional cross section of 85 ± 3 $Å^2$. This value is in good agreement with those measured in low pressure spontaneous Rayleigh experiments by Keijser et. al.[7] (83 ± 2 $Å^2$, 2-12 amagat) and Cooper et. al.[6] (81 $Å^2$, 1-5 amagat).

Fig. 4.6 shows a similar plot of the best fit values of the off diagonal decay rates for RIPS spectra at several densities up to 25.9 amagat. Since the decay rate for the off diagonal scattering is different for each state, only the rate for the most populated J level

(γ_{16}) has been plotted. The plot shows that γ_{16} (and thus γ_0) is linear to density, with a slope of $(1.94 \pm .08) \times 10^{-2}$ ps^{-1}amagat^{-1}. It was found that the data at each density could be fit using a value of $A = .009 \pm .001$ for the J-dependence.

The necessity of including a significant J-dependence in the off diagonal rates at high densities can be seen from Fig. 4.7a, which compares the experimental recurrence at 23.3 amagat with simulations using J-dependent and J-independent rates. The J-independent decay in Fig. 4.7b has been set equal to the best fit J-dependent decay for the J=16 state. The J-dependent recurrence in Fig. 4.7a fits the data quite well, whereas the J independent simulation in Fig. 4.7b has a slightly different shape and is broader than the experimental recurrence. Presumably, this J-dependence of the decay would also be apparent at lower densities as well, provided the spectra are taken out to a sufficiently long delay time.

The decay rates for individual J states corresponding to the best fit exponential gap parameters given above are plotted in Fig. 4.8. Also plotted are the individual J decay rates corresponding to the S branch spontaneous rotational Raman line width measurements of Herpin and Lallemond[4] taken at 2.6 amagat, and those obtained earlier by Jammu et. al.[3] at 5 and 9 amagat. The rates found from the line width measurements have a slightly greater J dependence and are slightly faster than the RIPS rates. Of course, the frequency domain experiments measure the individual line widths, whereas in the RIPS experiment all the populated J states contribute to a single overall decay rate. Also, the RIPS data reported here was taken at higher densities and over a much larger density range than the frequency domain data mentioned above.

Because RIPS can be used to measure decay rates for both diagonal and off diagonal scattering simultaneously, it has the potential to provide a great deal of valuable information concerning collisional dynamics. First note that the linearity of the decay rates with pressure shown in Figs. 4.5 and 4.6 demonstrates that bimolecular collisions dominate the dephasing dynamics for both types of scattering over the entire density range

investigated. These two plots also show that the rate of decay for the coherence associated with the diagonal scattering is only about 65% of that for the off diagonal scattering (at J=16), suggesting that different mechanisms are responsible for the dephasing of the diagonal and off diagonal coherence.

The difference in decay rates is consistent with Gordon's theory of frequency domain line broadening,[1,2] which predicts that collisions have differing effects on the Raman Q and O, S branches. According to Gordon collisions that change the J state effectively interrupt the O and S branch scattering, since within these branches the transition frequencies are different for different J states. Therefore, a rotationally inelastic collision will move the molecule to a state that has a different transition frequency. In other words, the inelastic collision limits the molecule's effective lifetime during which is can contribute to a particular rotation transition.

Rotationally inelastic collisions do not necessarily interrupt the Q branch scattering, however, since all the J lines are superimposed at a transition frequency of zero. A collision causing a transition between different J states will leave the molecule with the same Q branch transition frequency of zero. The Q branch "lifetime" results mainly from molecular realignment due to reorienting collisions. Of course, these reorienting collisions can also be expected to cause a decay of the O and S branches. Consequently, according to the theory, the decay associated with the off diagonal scattering depends on both inelastic and reorienting collisions, whereas the decay of the diagonal states is mainly from reorientating collisions, which may be either elastic or inelastic.

Recall that in Chapter 3 a comparison with results from experiments that directly measure changes in rotational state population showed that the RIPS O, S branch scattering decays at about the inelastic collision rate. The line broadening theory outlined above therefore suggests that elastic reorienting collisions are not prevalent, for they would cause the RIPS O, S branches to decay faster than the inelastic collision rate. As a result the Q branch decay is due to inelastic collisions that change the orientation, and the O, S branch

decay is due to energy transferring collisions, whether or not the orientation changes. Since the RIPS Q branch scattering decays about 30-35% slower than the O, S scattering, the data suggests that a significant number of collisions involving energy change do not result in reorientation.

4.24 Limitations of the Phenomenological Model

The decay of the off diagonal coherence can be measured at densities where the first recurrence remains large enough to be observed in the spectrum; at densities beyond this point there are no spectral features with which to fit a decay constant. For CO_2 this limit is reached at a density between 35 and 40 amagat. However, fitting the recurrence decay above about 350 psi is complicated by a broadening of the initial peak in the experimental spectrum, which increases gradually with pressure. The broadening is not too significant in the spectra between 15 and 26 amagat (see Figs. 4.3, 4.4), but becomes unmistakable by 39.8 amagat, as shown in Fig. 4.9. At 87.3 amagat the discrepancy is larger yet (Fig. 4.10), while in the saturated vapor the experimental peak is almost two times wider than the simulated one.

Several potential sources for the broadening of the initial peak can be ruled out. For example, an electronic molecular response would be instantaneous, whereas the additional intensity observed in the spectrum is clearly delayed by hundreds of femtoseconds. A collision-induced component to the scattering could contribute to the peak, but molecular dynamics simulations suggest the intensity of the collision induced signal alone is too small to account for the discrepancy.[12,24] Finally, classical molecular dynamics simulations performed in our laboratory using a Lennard-Jones two site potential do not show any collective orientational effects in the density range of interest.

In light of the above reasoning, we believe the broadening at higher densities is due to a slowing of the initial alignment and dephasing of individual molecules in the sample,

caused by frequent collisions that hinder the molecular free rotation. We would expect such a slowing of the rotation to become significant when the collision frequency becomes greater than the rotational period. At that point the J states are so short lived that the initial alignment and dephasing no longer occurs by free molecular rotation, but depends upon some type of slower diffusional motion. To verify the plausibility of this reasoning, consider the RIPS spectrum at 39.8 amagat, where the broadening becomes noticeable. Linear extrapolation of the low pressure inelastic scattering decay rate (from Fig. 4.6) to this density gives an average collision frequency of 1.3 ps, which is half the rotational period of CO_2 in the J=16 state. This comparability of the collision frequency and the rotational period explains the onset of broadening in this density range.

Note that the broadening of a peak in the time domain spectrum is equivalent to a narrowing of a feature in the frequency domain spectrum, and that the time domain micro structure reflects the frequency domain macro structure (and vice versa). Therefore, the broadening of the initial dephasing peak in the RIPS spectrum reflects a narrowing of the envelope of the frequency domain rotational spectrum. This collisional narrowing is similar to the narrowing of the Doppler profile seen in the frequency domain. In the present case the narrowing is caused by an interruption of the molecular free rotation, which begins to blur the distinction between different J levels. Thus, this decrease in the "inhomogeneous" line width accompanies the simultaneous broadening of the individual or "homogeneous" line widths as the density and collision frequency is increased. To fit the data at high densities we need a model that reflects the frequency domain collisional narrowing by keeping track of the orientation of molecules whose rotation is collisionally hindered, in addition to that of molecules that have not yet collided.

4.3 Rotational Diffusion Model

One simple model that can account for broadening of the initial peak at higher densities is the extended rotational diffusion model developed by Gordon.[25] The J-diffusion variety of this model assumes that the rotational angular momentum is randomized by each collision, with molecules undergoing free rotation between collisions. The molecules thus experience a random walk or diffusion in angular momentum space. This J diffusion is similar to "regular" orientational diffusion, in which the random walk occurs in position space. Orientational diffusion has been used successfully to describe dynamics in some liquids,[26,27] but will not suffice here, since it predicts a simple exponential correlation function that cannot account for the negative or anticorrelated features in the RIPS spectra. Anticorrelation can occur, however, in J diffusion.

The memory function approach provides a convenient method of implementing the extended J diffusion model. As shown by Berne and Harp,[28] this approach can be used to relate the orientational autocorrelation function $G(t) = \langle P_2(\cos\omega_{JJ'})\rangle$ to its associated memory function, K(t), via a Volterra equation:

$$\dot{G}(t) = -\int_0^t du K(u) G(t-u) \tag{4.6}$$

Bliot et. al.[29] have shown that the memory function for molecules undergoing extended J diffusion is related to the memory function for freely rotating molecules (K_{FR}) by

$$K_{JD}(t) = K_{FR}(t)\exp(-t/T_{JD}), \tag{4.7}$$

where T_{JD} ($=1/\gamma_{JD}$) is the time between angular momentum changing collisions.

We use a trapezoidal approximation to the integral[30] in Eq. (4.6) to solve for the derivative of the orientational autocorrelation function. The MATLAB® functions used to carry out these calculations are contained in the appendix. We first analytically calculate the free rotor correlation function (and its derivative) for a thermal ensemble of CO_2 molecules and use it to solve for $K_{FR}(t)$. The diffusional memory function is then calculated via Eq. (4.7). Finally, $K_{JD}(t)$ is plugged back into Eq. (4.6) to obtain the correlation function. The accuracy of the numerical solution to Eq. (4.6) is quite sensitive to the size of the time step used in the calculation. For CO_2 a step size of 0.5 fs was used, as it was found empirically that further reduction of the step size did not result in significant changes in the calculated correlation functions.

Figs. 4.11 to 4.16 compare calculated J diffusion correlation functions to experimental spectra taken over a wide range of densities. As before, the simulations have been smoothed by the experimentally determined pump and probe pulse widths. The simulations reproduce the CO_2 data reasonably well in the liquid and very high density gas, where the spectrum consists primarily of a single decaying peak near time zero. For example, the match is seen to be pretty good at 87.3 amagat (Fig. 4.13a), which corresponds to CO_2 gas slightly below the liquid/vapor equilibrium density. Likewise, simulations of the vapor at the liquid/vapor equilibrium, the liquid at the liquid/vapor equilibrium, and the liquid at a density somewhat higher than the liquid/vapor equilibrium all fit the data well (Figs. 4.14-4.16). Note in particular that at each of these four densities the width of the J diffusion simulation matches the initial peak of the experimental data. For comparison, we have included with the liquid data of Fig. 4.16 a simulation based upon the phenomenological model, which is shown to be in poor agreement with the data.

The fit to the RIPS spectrum for CO_2 liquid in equilibrium with vapor gives a J diffusion collision time of 120 fs. This is in fairly good agreement with the value of 90 fs extracted from the Raman linewidth data of van Konynenburg and Steele.[9] The latter data

was also taken at the liquid/vapor equilibrium, though at a somewhat lower temperature of 281 K.

We have found that the J diffusion model gives reasonably good fits to the RIPS data at very high densities, where the initial peak is the only feature present in the spectrum. The fits are not as good at lower densities where several spectral features occur. For example, an enlarged view of the data at 87.3 amagat (Fig. 4.13b) shows that, while the model matches the dephasing of the initial peak pretty well, the fit to the Q branch feature between 1-5 ps is poor. Thus, if we fit the initial peak correctly, the simulated decay of the Q branch transitions is too fast.

The discrepancies are larger at somewhat lower densities, as shown by a comparison of the simulation to the 25.9 amagat data displayed in Fig. 4.12. Here the J diffusion collision time has been adjusted to match the decay rate of the recurrences. However, it can be seen that when the collision time is chosen in this way to match the relative amplitudes of the initial peak and the first recurrence, there is not enough diffusional broadening of the initial peak in the simulation. Equivalently, making the collision time shorter will sufficiently broaden the initial peak, but will make the recurrence far too small and the Q branch feature too large and too steep. As a result the J diffusion model does not give a good fit to the data between 5 and 87 amagat.

One serious drawback of the J diffusion model is that it can only account for one time scale--nominally the time between J changing collisions. As mentioned above, the experimental data in the moderate to high pressure gas has at least two associated time scales. One is related mainly to the rate of energy (or J) changing collisions. The other depends more strongly on reorienting collisions. The J diffusion model cannot simultaneously account for both time scales.

A second shortcoming of the J diffusion model, which can be seen in Fig. 4.12 (and 4.7), is that the simulated recurrence is the wrong shape due to a lack of J dependence in the decay. It has been pointed out that one cannot include a J dependence in the model

and still maintain the equilibrium thermal distribution of rotational energy.[25] From a more practical point of view, it is not clear how a J dependence should be incorporated using the memory function formalism, since the correlation function of Eq. (4.6) is not separable into state specific terms. In other words, the J dependence could be put into K, but the effect of this on G is not one to one due to the convoluted relationship between K and G.

The inadequacy of the J diffusion model in describing the rotational motion suggested by the RIPS experiments is also evident in the molecular dynamics simulations of Steel and Street.[11] They compared the results of the J diffusion model to molecular dynamics simulations using a two site Lennard-Jones potential with quadrupole interactions. They found that the J diffusion model could not reproduce their calculated correlation functions.

We know of only one other attempt to fit gas phase orientational dynamics using the J diffusion model. This involved depolarized Rayleigh scattering experiments in CO_2 done by Versmold.[8] In that study the author claimed "almost perfect" agreement of the model with the data at densities between 23 and 190 amagat. It is perhaps a testament to the high sensitivity of RIPS that our data show fairly large discrepancies with the model throughout much of this density range.

There is a possibility that a better fit to the experimental data could be obtained in the middle density range by using something other than an exponential for damping the memory function in Eq. (4.7). For example, a spectral moment analysis suggests a Gaussian form for the memory function[31]

$$K_{JD}(t) = K_{FR}(t)\exp(-Ct^2), \tag{4.8}$$

where C depends on the mean square torque. Attempts at using this form for the memory function did not improve the fits to the experimental data. Likewise, a number of other simple functions, as diverse as $sech^2$ and a damped cosine, were also tried with little

success. Part of the reason why none of these models works is because they all account for only a single time scale. Although one could take the product of K_{FR} with a more complicated function, or a combination of functions, having different time scales to try to match the data, the physical significance of the parameters in the resulting memory function would be unclear.

In Fig. 4.17 we have plotted the J diffusion decay rates ($1/T_{JD}$) for the densities at which good fits to the data were obtained. Also plotted is the extrapolated best fit line through the phenomenological off diagonal decay rates found at lower densities. Although the decay rate in each model represents the effective collision frequency, the two sets of points do not appear to lie on the same line. This is to be expected, considering that these two models are quite different.

Ideally, we would like a model that accurately describes the rotational dynamics throughout the entire fluid density regime. Such a model would likely incorporate aspects of both the phenomenological and J diffusion models. Like the phenomenological model, the improved model should account for the differing rates of decay for the diagonal and the off diagonal scattering, and would allow for a J dependence of the off diagonal decay. At higher densities, meanwhile, the model should be similar to the J diffusion model in predicting the broadening of the spectrum that results from frequent collisions.

The alternative to developing such a model would be to compare the experimental results to molecular dynamics simulations using model potentials. This may be more expedient for a given molecule, but would sacrifice the simplicity and generality contained in a model for reorientation containing a few dynamic parameters, such as the elastic and inelastic collision frequency.

References

1. R.G. Gordon, J. Chem. Phys. **44**, 3083 (1965).
2. W.B. Neilsen and R.G. Gordon, J. Chem. Phys. **58**, 4131 (1973).
3. K.S. Jammu, G.E. St. John and H.L. Welsh, Can. J. Phys. **44**, 797 (1966).
4. M.-C. Herpin and P. Lallemand, J. Quant. Radiat. Transfer **15**, 779 (1975).
5. J.P. Boquillon, SPIE *Pulsed Single Freq. Lasers: Technology and Applications* **912**, 160 (1988).
6. V.G. Cooper, A.D. May, E.H. Hara and H.F. Knaap, Phys. Lett **27A**, 52 (1968).
7. R.A.J. Keijser, K.D. Van Den Hout, M. De Groot and H.F.P. Knaap, Physica **75**, 515 (1974).
8. H. Versmold, Mol. Phys. **43**, 383 (1981).
9. P. van Konynenburg and W.A. Steele, J. Chem. Phys. **62**, 2301 (1975).
10. M. Perrot, J. Devaure and J. Lascombe, Mol. Phys. **36**, 921 (1978).
11. W.A. Steele and W.B. Streett, Mol. Phys. **39**, 279 (1980).
12. D. Frenkel and J.P. McTague, J. Chem. Phys. **72**, 2801 (1980).
13. C. J. Jameson, A.K. Jameson, N.C. Smith and Karol Jackowski, J. Chem. Phys. **86**, 2717 (1987).
14. B.I. Greene and R.C. Farrow, J. Chem. Phys. **77**, 4779 (1982).
15. B.I. Greene and R.C. Farrow, Chem. Phys. Lett. **98**, 273 (1983).
16. C. Kalpouzos, W.T. Lotshaw, D. McMorrow and G.A. Kenney-Wallace, J. Phys. Chem. **91**, 2028 (1987).
17. D. McMorrow, W.T. Lotshaw and G.A. Kenney-Wallace, IEEE J. Quantum Electronics **24**, 443 (1988).
18. M. Cho, M. Du, N.F. Scherer, G.R. Fleming and S. Mukamel, J. Chem. Phys. **99**, 2410 (1993).

19. P.W. Atkins, *Physical Chemistry (3rd edn.)*, (W.H. Freeman and Company, New York, 1986).

20. W.H. Press, B.P. Flannery, S.A. Teukolsky and W.T. Vetterling, *Numerical Recipes*, (Cambridge University Press, Cambridge, 1986).

21. J. H. Dymond and E. B. Smith, *The Virial Coefficients of Pure Gases and Mixtures, A Critical Compilation*, (Oxford University Press, Oxford, 1980).

22. N.B. Vargaftik, *Tables on the Thermophysical Properties of Liquids and Gases (2nd edn.)*, (Hemisphere Publishing Corp., 1975).

23. J.I. Steinfeld, P. Ruttenberg, G. Millot, G. Fanjoux and B. Lavorel, J. Phys. Chem. **95**, 9638 (1991).

24. H. Stassen, T. Dorfmuller and B.M. Ladanyi, J. Chem. Phys. **100**, 6318 (1994).

25. R.G. Gordon, J. Chem. Phys. **44**, 1830 (1965).

26. D. Kivelson and P.A. Madden, Ann. Rev. Phys. Chem. **31**, 523 (1980).

27. G.R. Alms, D.R. Bauer, J.I. Brauman and R. Pecora, J. Chem. Phys. **58**, 5570 (1973).

28. B.J. Berne and G.D. Harp, Adv. Chem. Phys. **17**, 63 (1970).

29. F. Bliot and E. Constant, Chem. Phys. Lett. **18**, 253 (1973).

30. T.E. Eagles and R.E.D. McClung, Chem. Phys. Lett. **22**, 414 (1973).

31. W.A. Steele, Mol. Phys. **43**, 141 (1981).

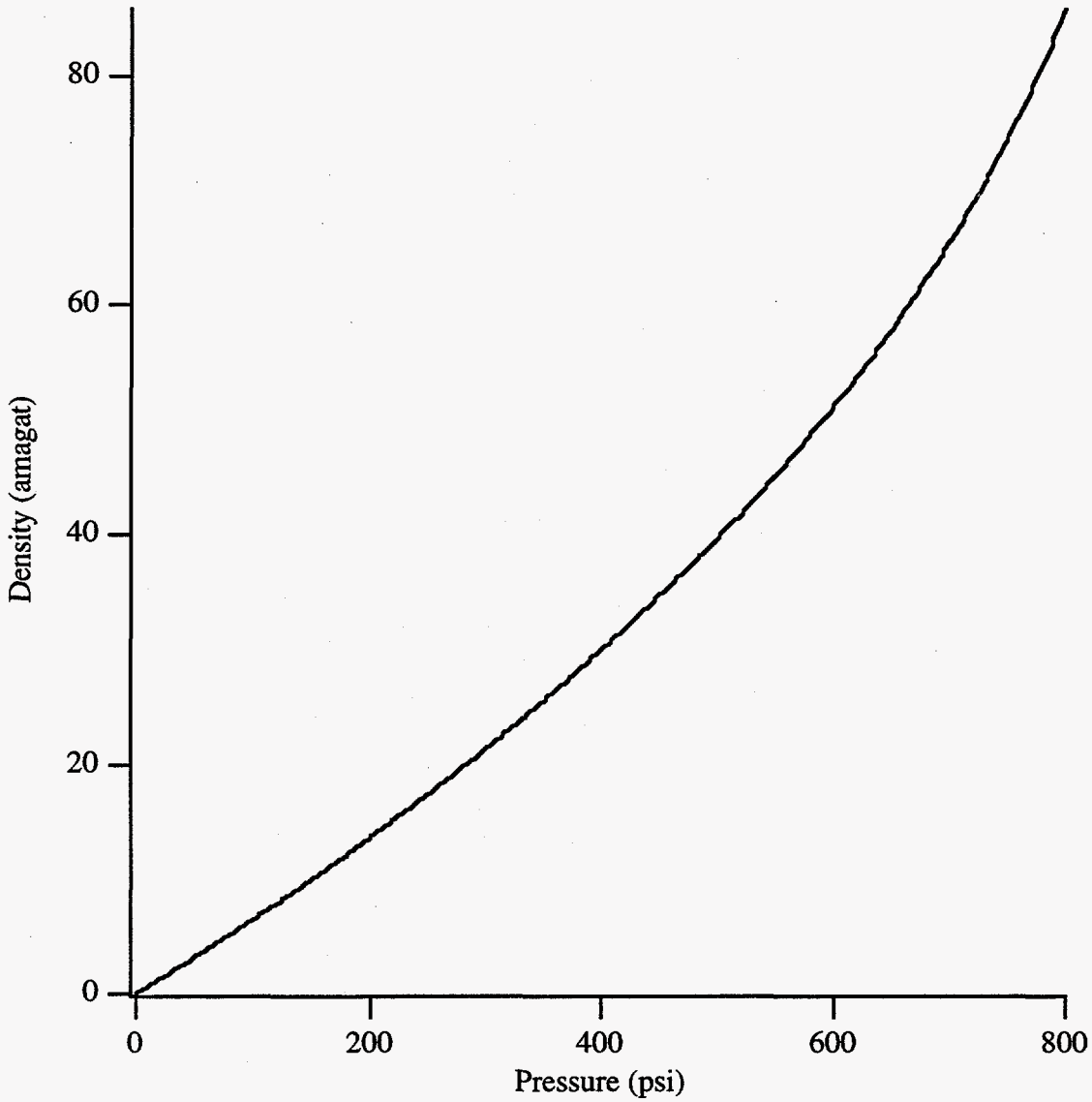

Fig. 4.1. CO_2 density versus pressure calculated from the virial expansion: $\rho + b\rho^2 + c\rho^3 = P/RT$, with b=-124.9 cm^3/mole and c=4363 cm^6/$mole^2$.

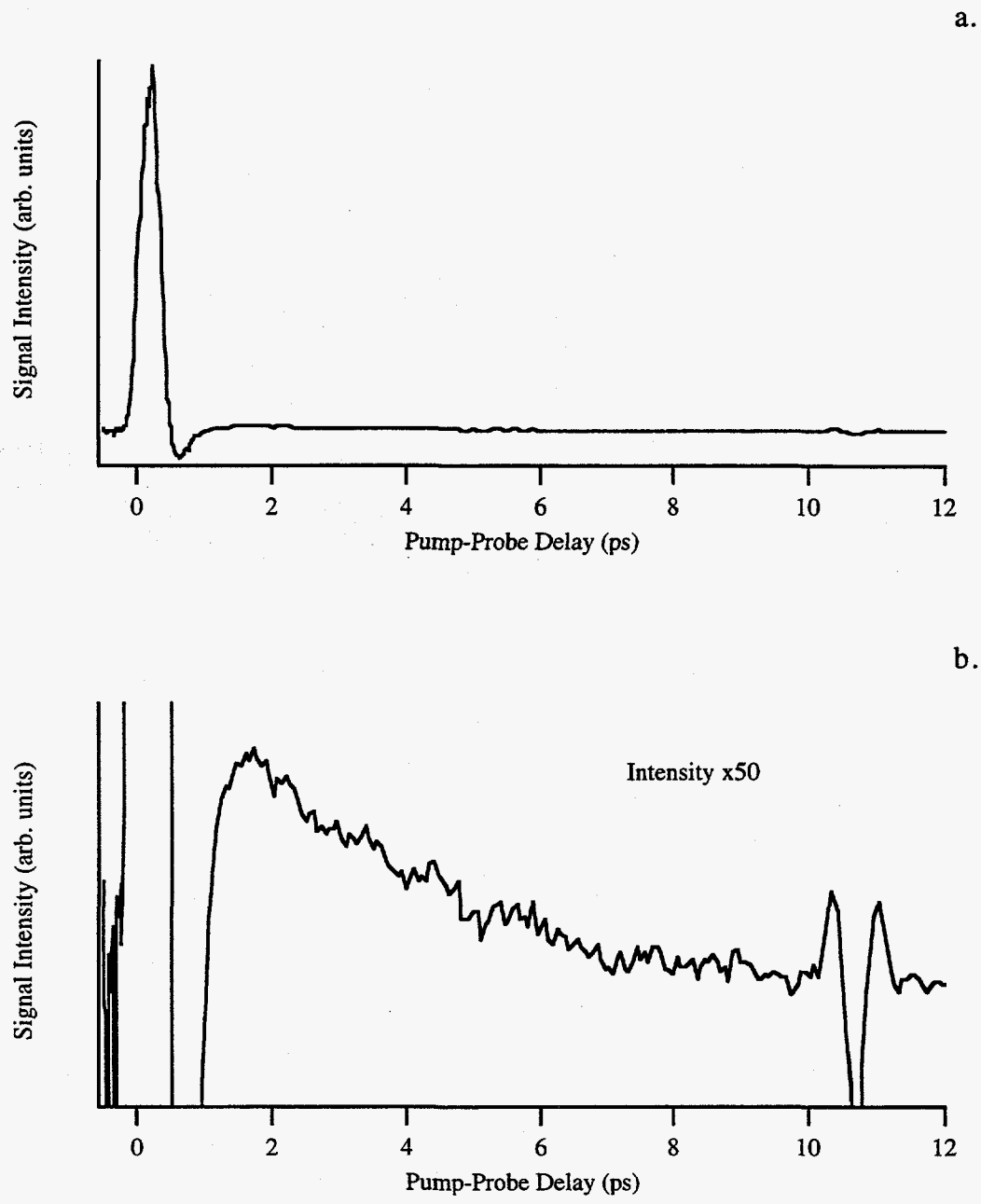

Figure 4.2. (a) The CO_2 RIPS spectrum at 296 K and 25.9 amagat, in which the first recurrence is just discernible. (b) A vertically expanded (x50) view of the spectrum in (a), in which the recurrence, as well as a broad, slowly decaying feature are evident.

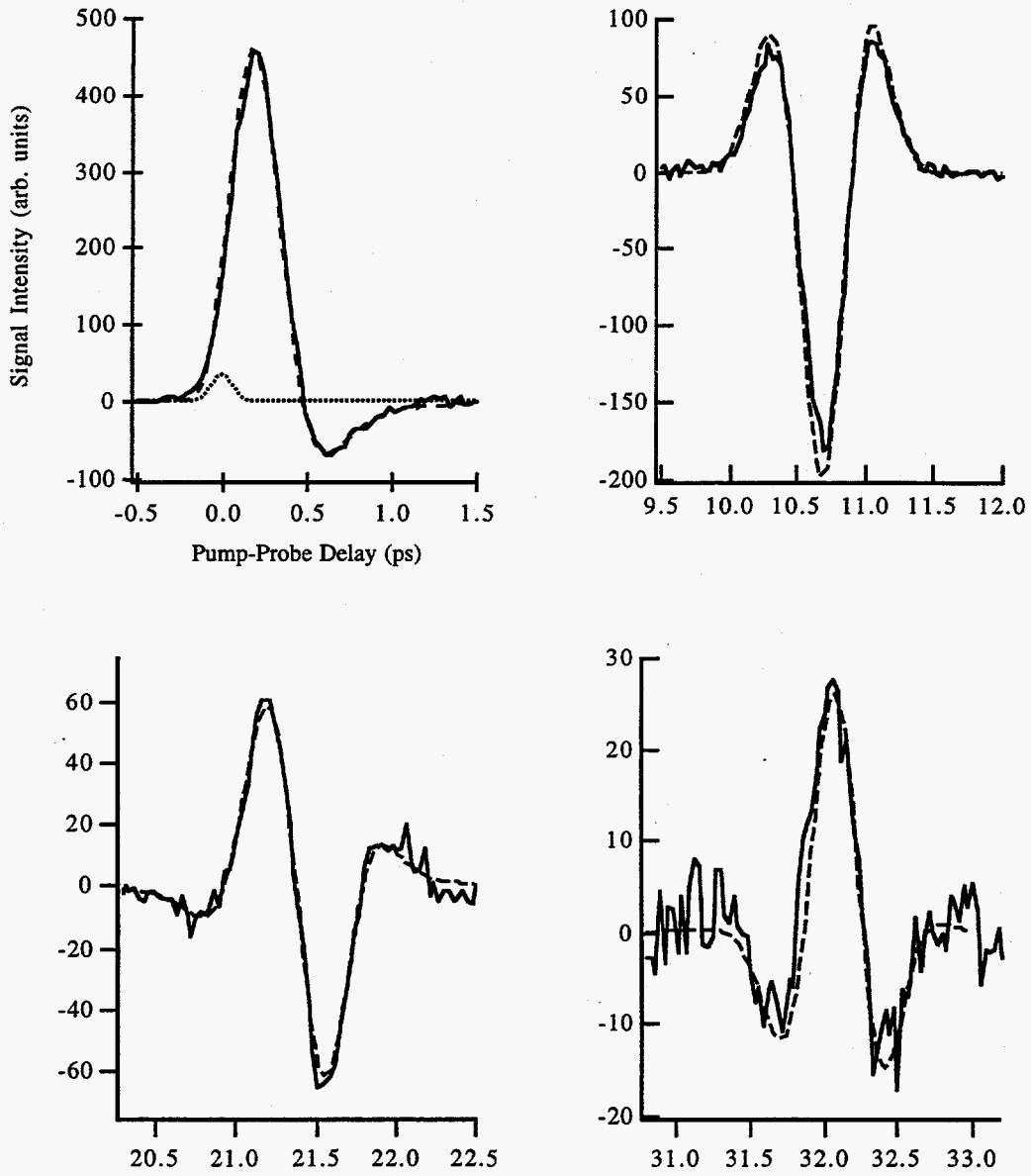

Fig. 4.3. Fit of phenomenological model (dashed line) to experimental (solid line) RIPS CO_2 spectrum at 5.1 amagat, with $\gamma_J'=0$, $\gamma_0=0.12$ ps^{-1}, and A=0.01. The simulated spectrum was smoothed by the pump and probe pulse widths (140 fs). In addition, a small Gaussian component (200 fs FWHM, dotted line) was added to the simulations at zero delay to account for an instantaneous electronic response.

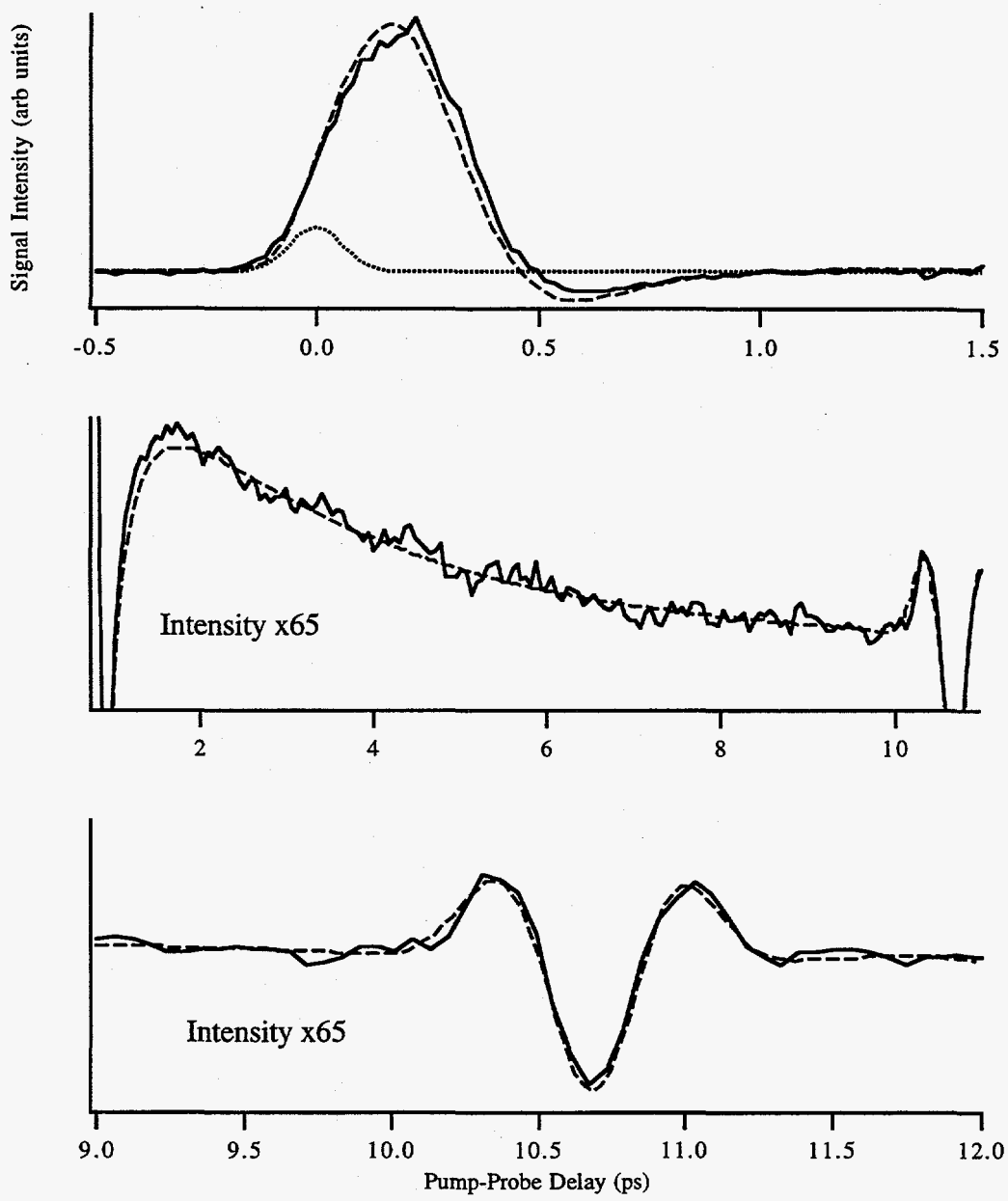

Fig. 4.4. Fit of the phenomenological decay model (dashed line) to the experimental (solid line) RIPS CO_2 spectrum at 25.9 amagat, using γ'_J=0.34 ps^{-1}, γ_0=0.565 ps^{-1}, and A=0.008. The simulation was smoothed by the pump and probe pulse widths (100 fs), and a small Gaussian component (150 fs FWHM) was included in the simulation to account for the instantaneous electronic response.

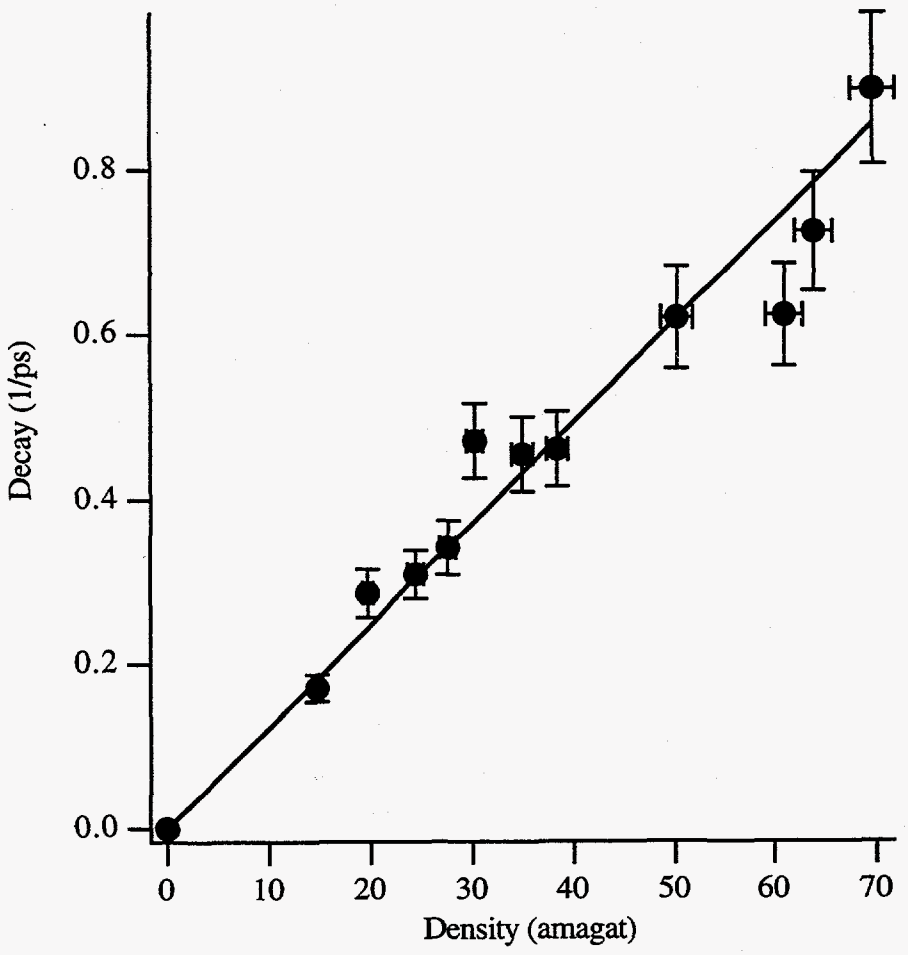

Fig. 4.5. RIPS coherence decay rate (γ') for diagonal states in CO_2 as a function of density. The rate is linear with density, having a slope of $(1.22 \pm .04) \times 10^{-2}$ $ps^{-1}amagat^{-1}$.

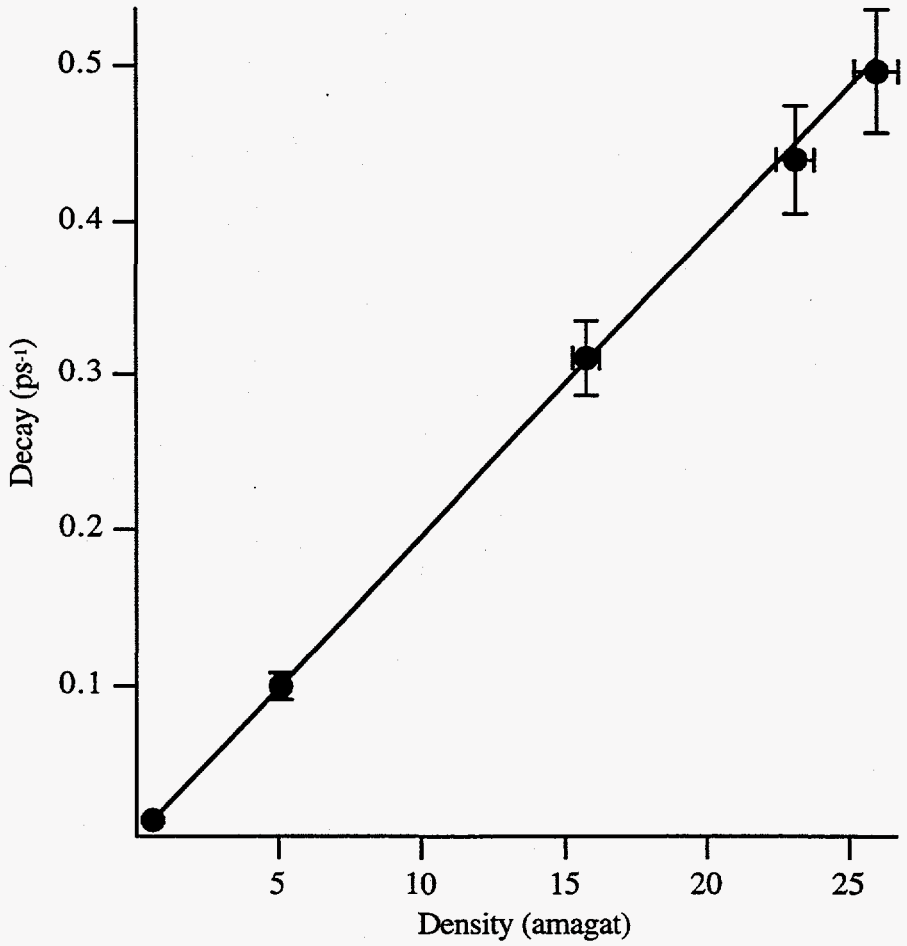

Fig. 4.6. RIPS coherence decay rate of the off diagonal states for CO_2 as a function of density. Plotted is the rate for J=16 (γ_{16}). The rate is linear with density, having a slope of $(1.94 \pm .08) \times 10^{-2}$ $ps^{-1}amagat^{-1}$.

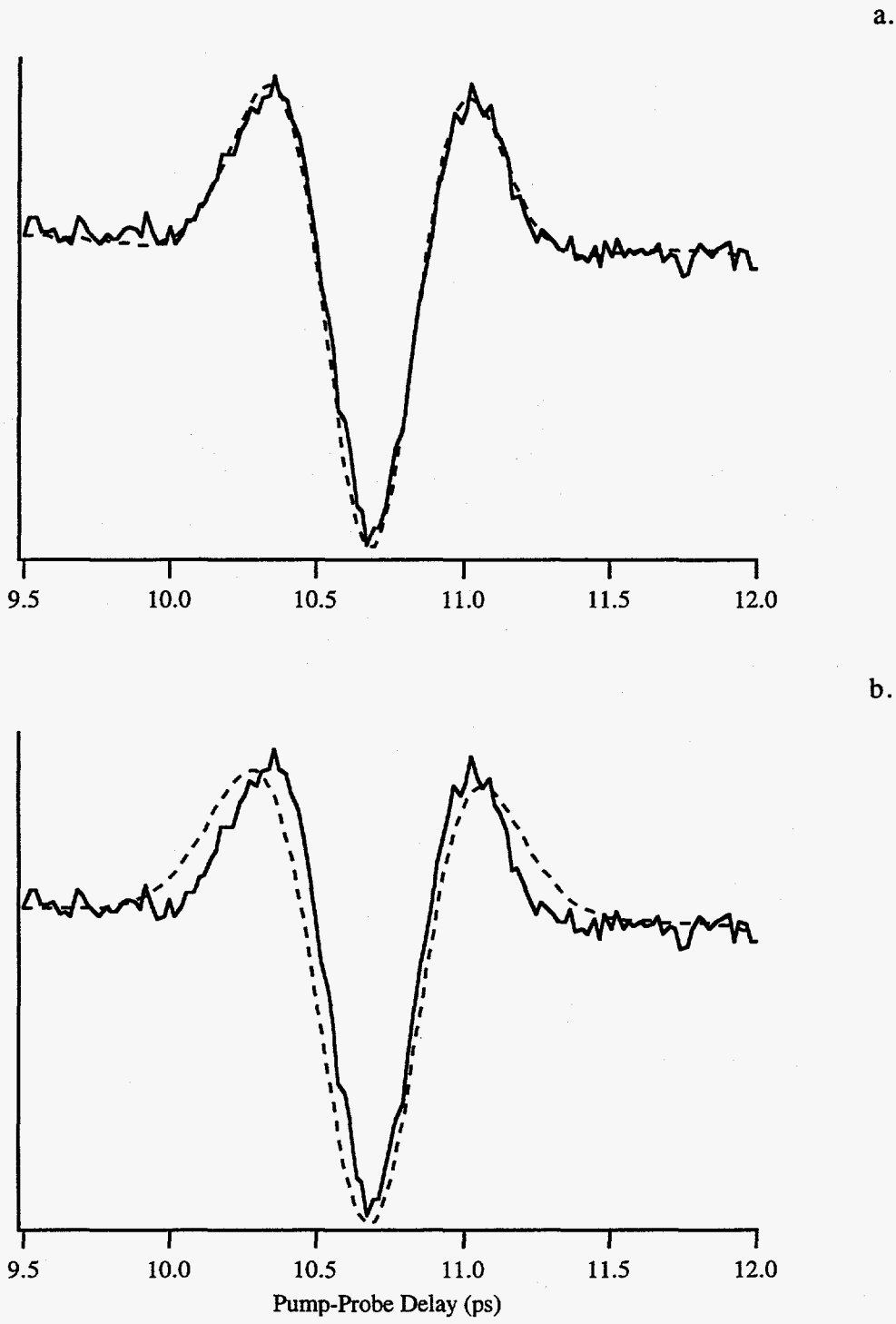

Fig 4.7. Fits (dashed line) to the experimental (solid line) CO_2 RIPS spectrum at 23.3 amagat using (a) J dependent decay γ=0.5exp(-.008J) ps^{-1}, and (b) J-independent decay γ=0.41 ps^{-1}, suggest a significant J dependence to the decay.

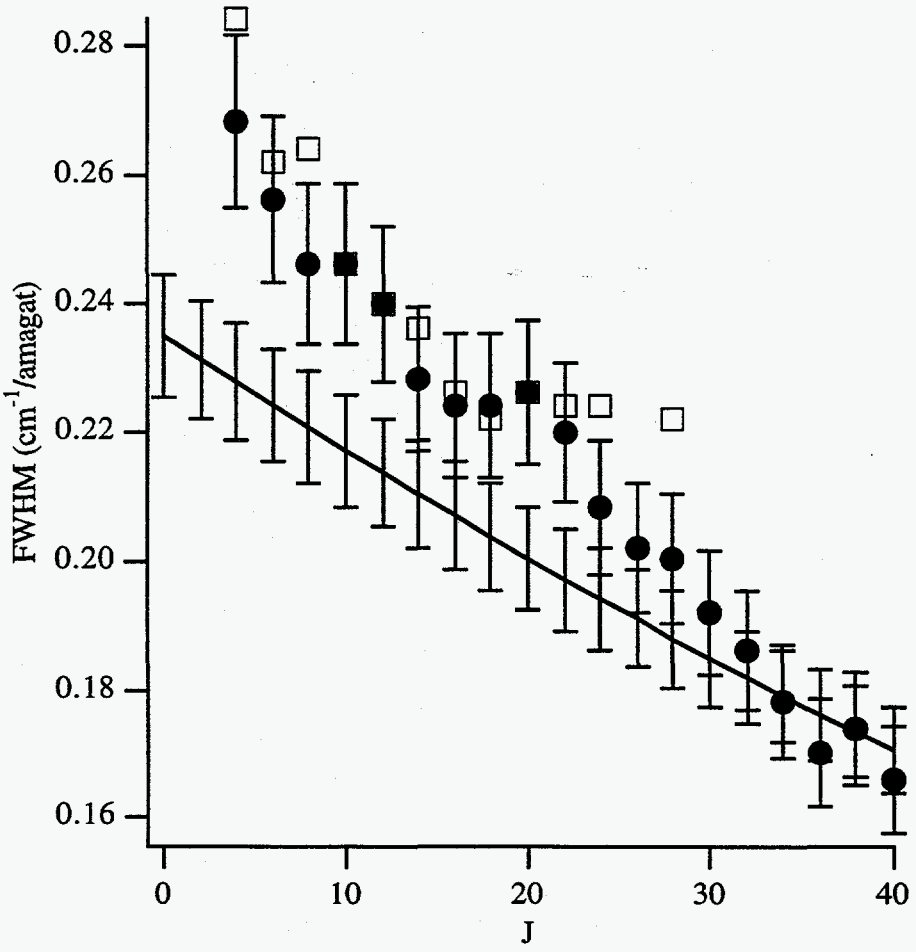

Fig. 4.8. Dependence of the RIPS off diagonal coherence decay rate on rotational state (solid line), converted to equivalent line widths. Also shown are the S branch rotational Raman linewidth measurements of Herpin and Lallemond (circles) and of Jammu et. al. (squares).

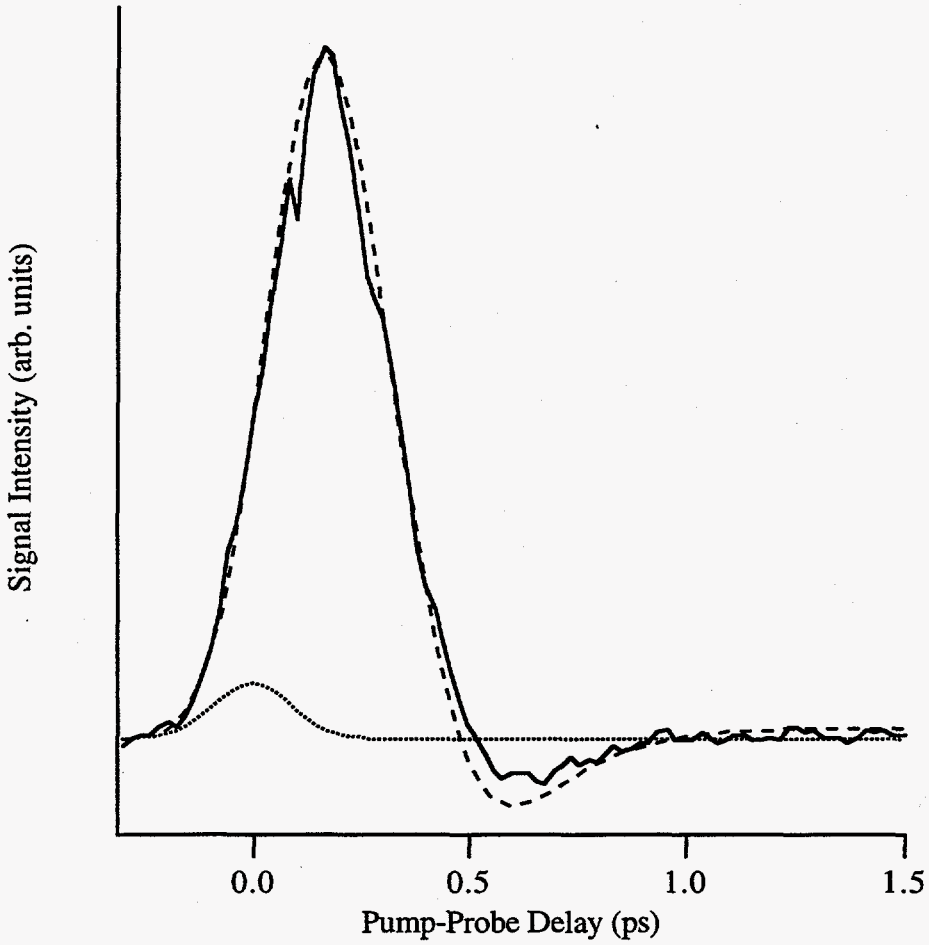

Fig. 4.9. Fit of the phenomenological decay model (dashed line) to the experimental (solid line) RIPS CO_2 spectrum at 39.8 amagat, using γ'_J=0.47 ps^{-1}, γ_0=0.76 ps^{-1}. The simulation was smoothed by the pump and probe pulse widths (140 fs), and also included the 200 fs Gaussian component shown as the dotted line in the figure. The broadening of the experimental spectrum, resulting in a poor fit between delays of 0.4 and 1 ps, cannot be reproduced with this model.

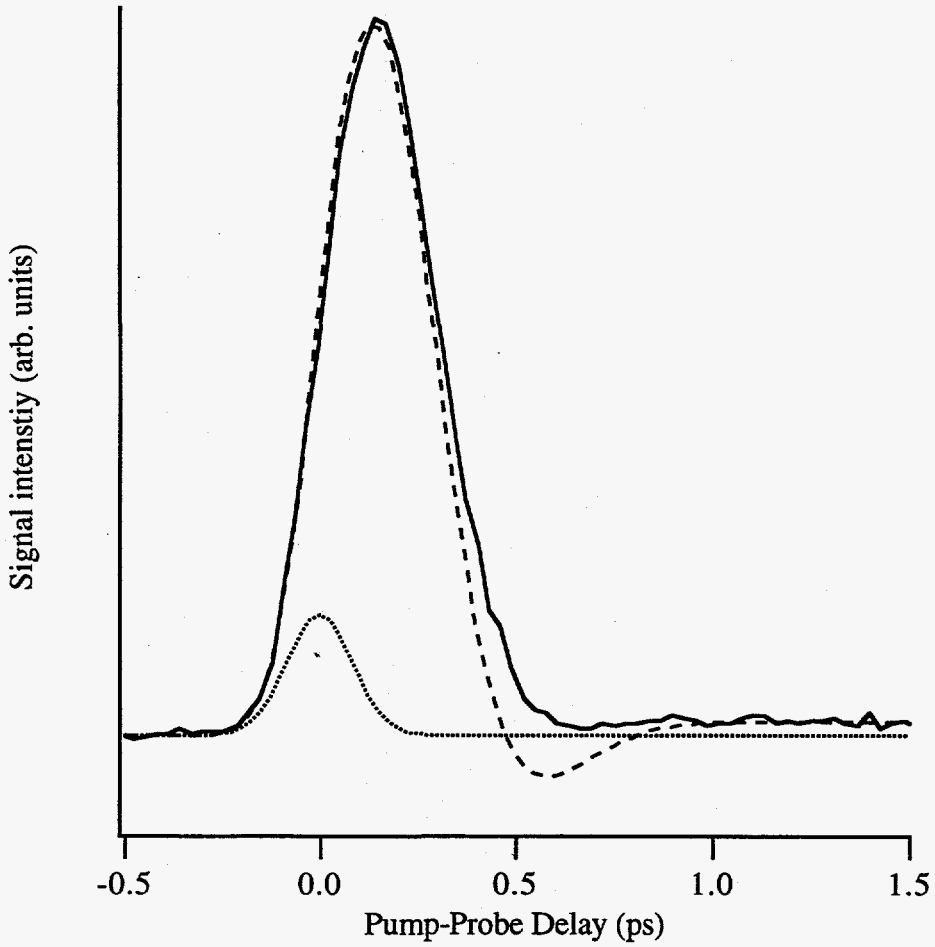

Fig. 4.10. Fit of the phenomenological decay model (dashed line) to the experimental (solid line) RIPS CO_2 spectrum at 87.3 amagat, using γ'_J=1 ps^{-1}, γ_0=2 ps^{-1}. The simulation was smoothed by the pump and probe pulse widths (130 fs), and also included the 200 fs Gaussian component shown as a dotted line in the figure. The fit is clearly quite poor at this density.

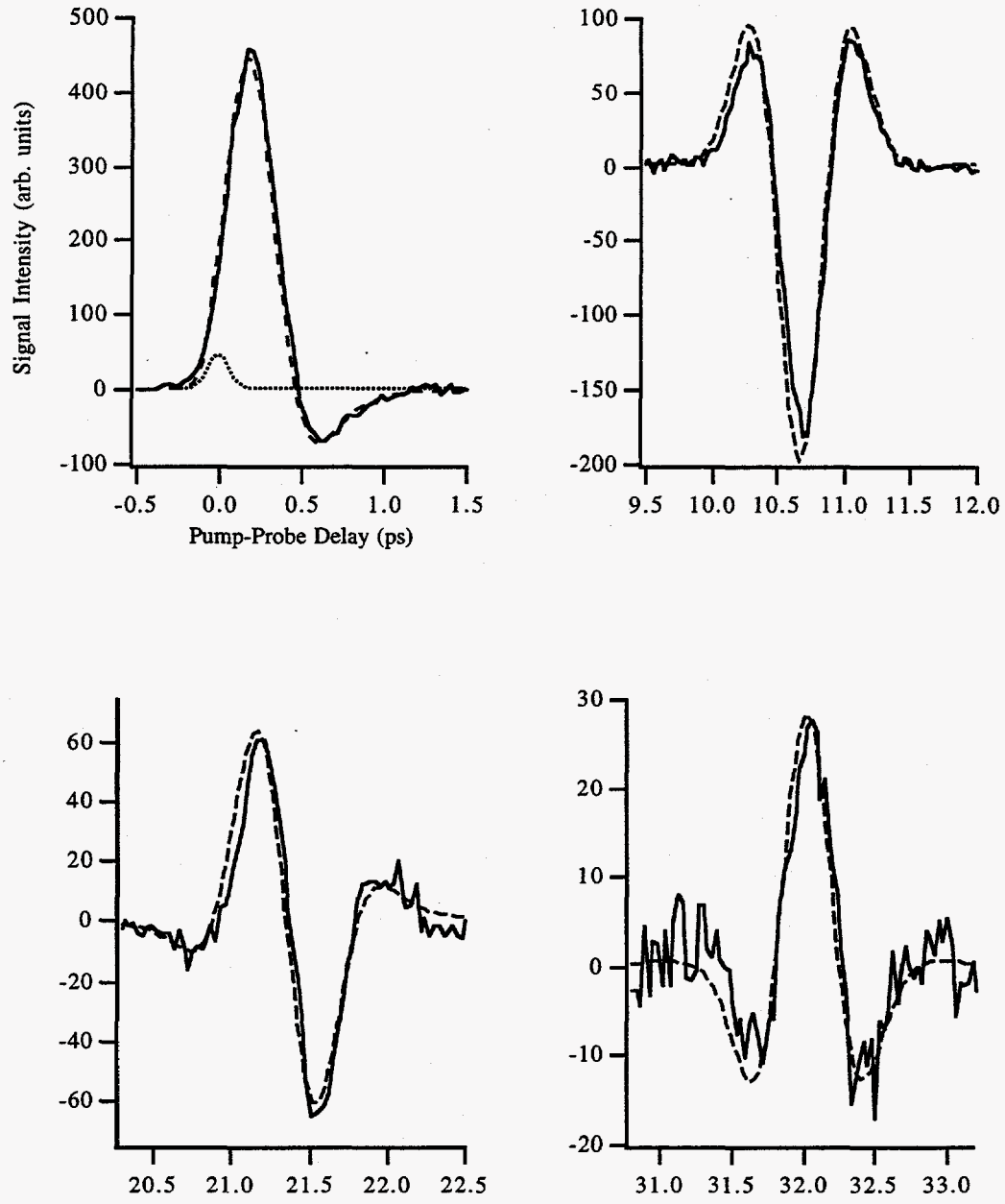

Fig. 4.11. Fit of J diffusion model (dashed line) to experimental (solid line) RIPS CO_2 spectrum at 5.1 amagat, with γ_{JD}=0.094 ps^{-1}. The simulated spectrum was smoothed by the pump and probe pulse widths (140 fs) and includes the Gaussian shown (200 fs FWHM).

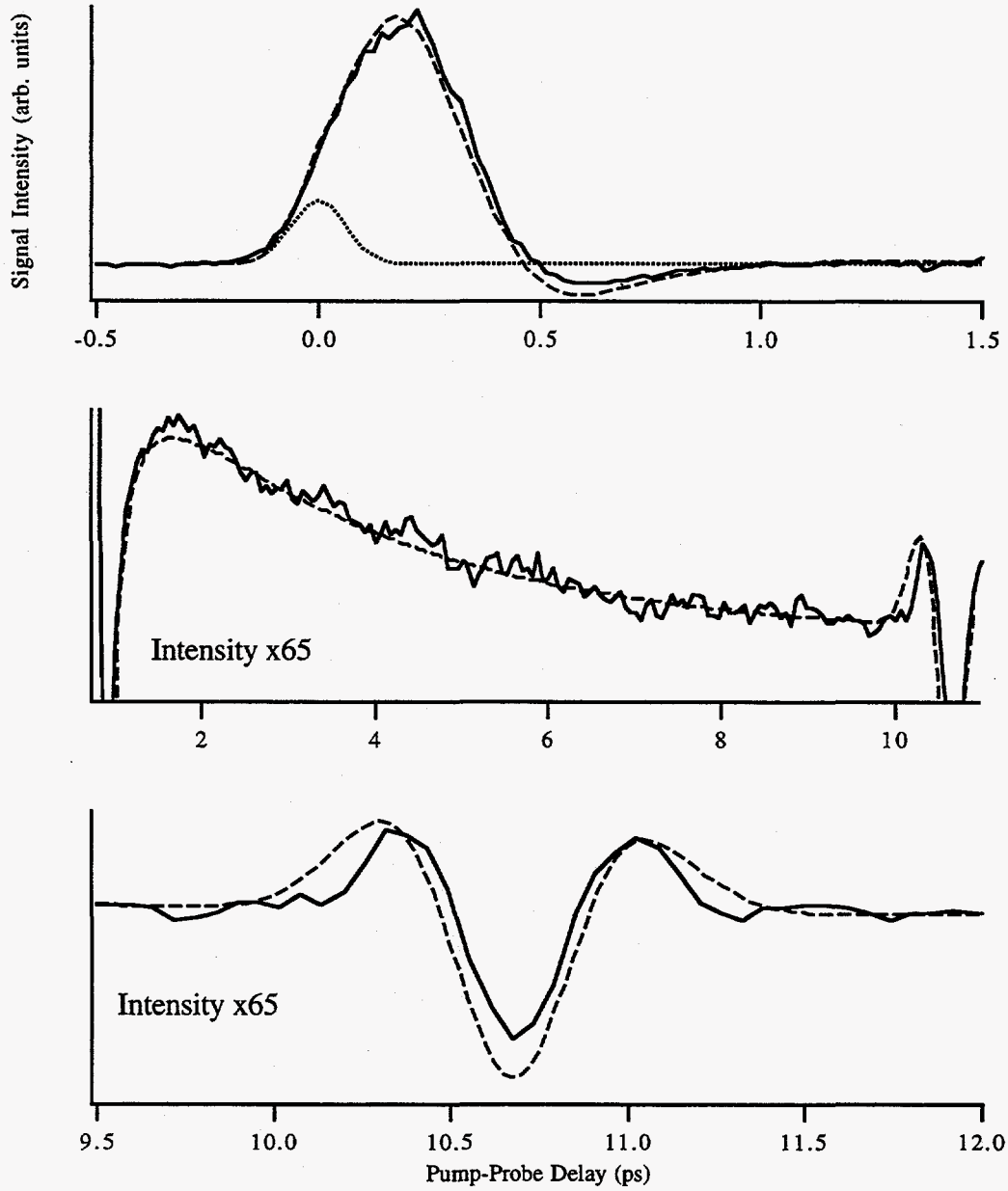

Fig. 4.12. Fit of the J diffusion model (dashed line) to the experimental (solid line) RIPS CO_2 spectrum at 25.9 amagat, using γ'_{JD}=0.45 ps^{-1}. The simulation was smoothed by the pump and probe pulse widths (100 fs), and includes a Gaussian component (150 fs FWHM, dotted line) to account for the instantaneous electronic response. The fit to the recurrence in particular is quite poor.

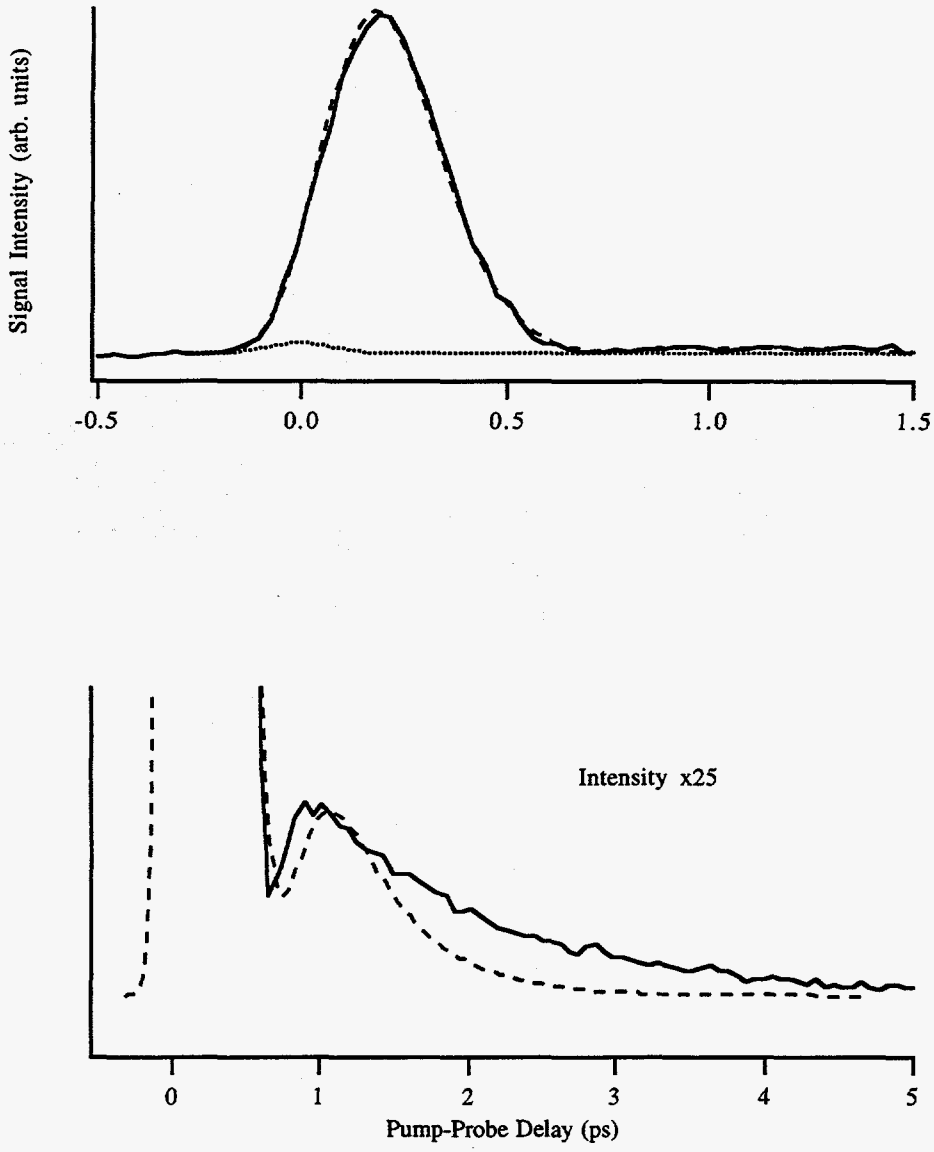

Fig 4.13. (a) Fit of the J diffusion model (dashed line) to the experimental (solid line) RIPS CO_2 spectrum at 87.3 amagat, using γ_{JD}=2.94 ps^{-1}. The simulation was smoothed by the pump and probe pulse widths (130 fs), and includes a Gaussian component (200 fs FWHM, dotted line) to account for the instantaneous electronic response. (b) A vertically expanded view of the data between 0 and 5 ps.

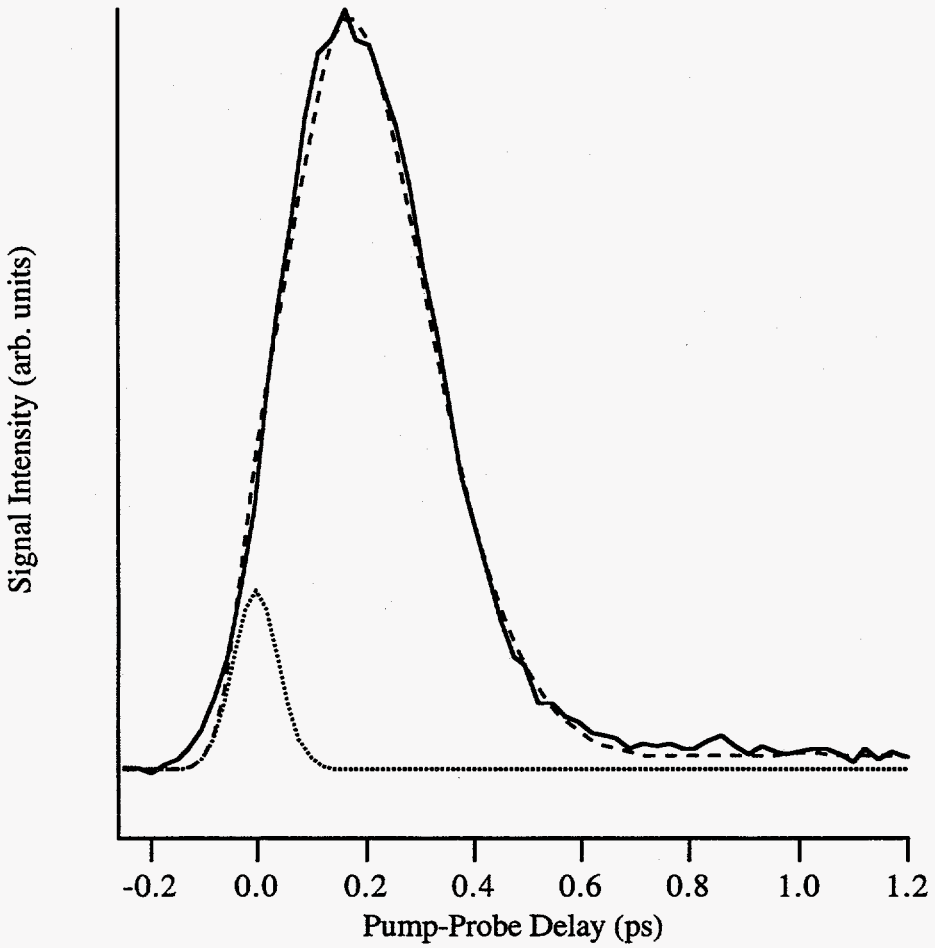

Fig. 4.14. Fit of the J diffusion model (dashed line) to the experimental (solid line) RIPS spectrum of CO_2 vapor at the liquid-vapor equilibrium (115.2 amagat), using γ_{JD}= 3.33 ps^{-1}. The simulation was smoothed by the pump and probe pulse widths (60 fs), and includes a Gaussian component (100 fs FWHM, dotted line) to account for the instantaneous electronic response.

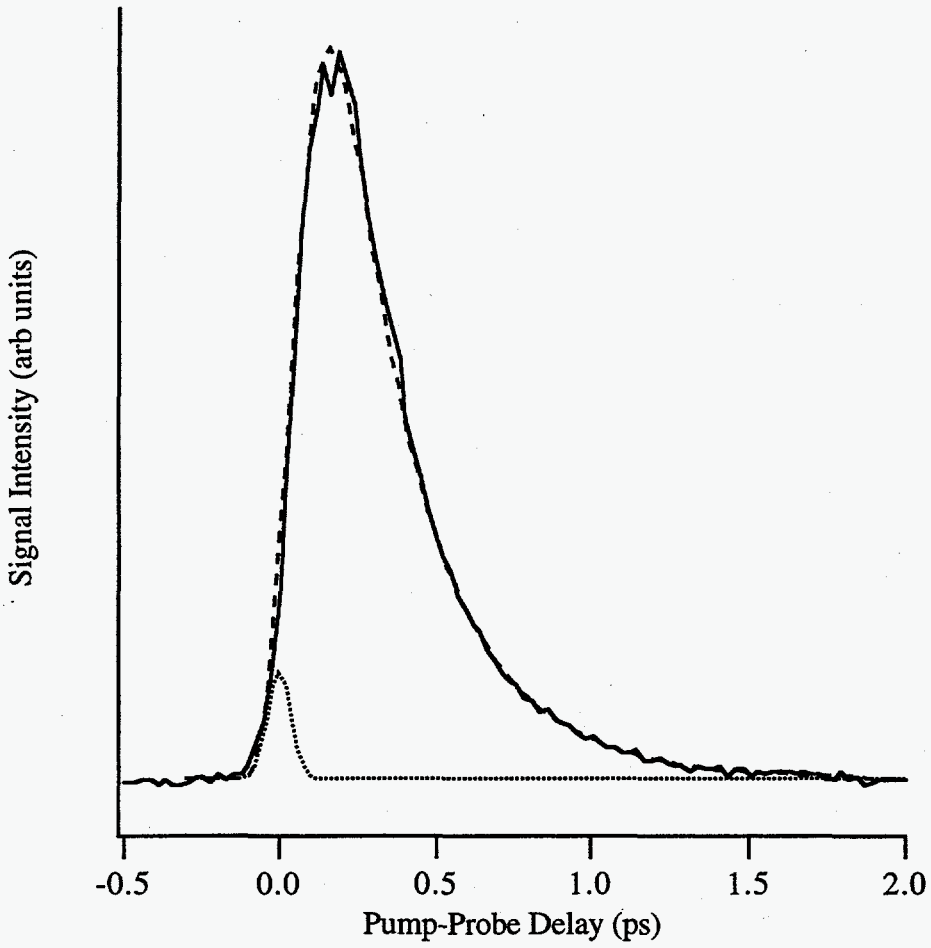

Fig 4.15. Fit of the J diffusion model (dashed line) to the experimental (solid line) RIPS spectrum of CO_2 liquid at the liquid-vapor equilibrium (354 amagat), using γ_{JD}=8.33 ps^{-1}. The simulation was smoothed by the pump and probe pulse widths (60 fs), and includes a Gaussian component (100 fs FWHM, dotted line) to account for the instantaneous electronic response.

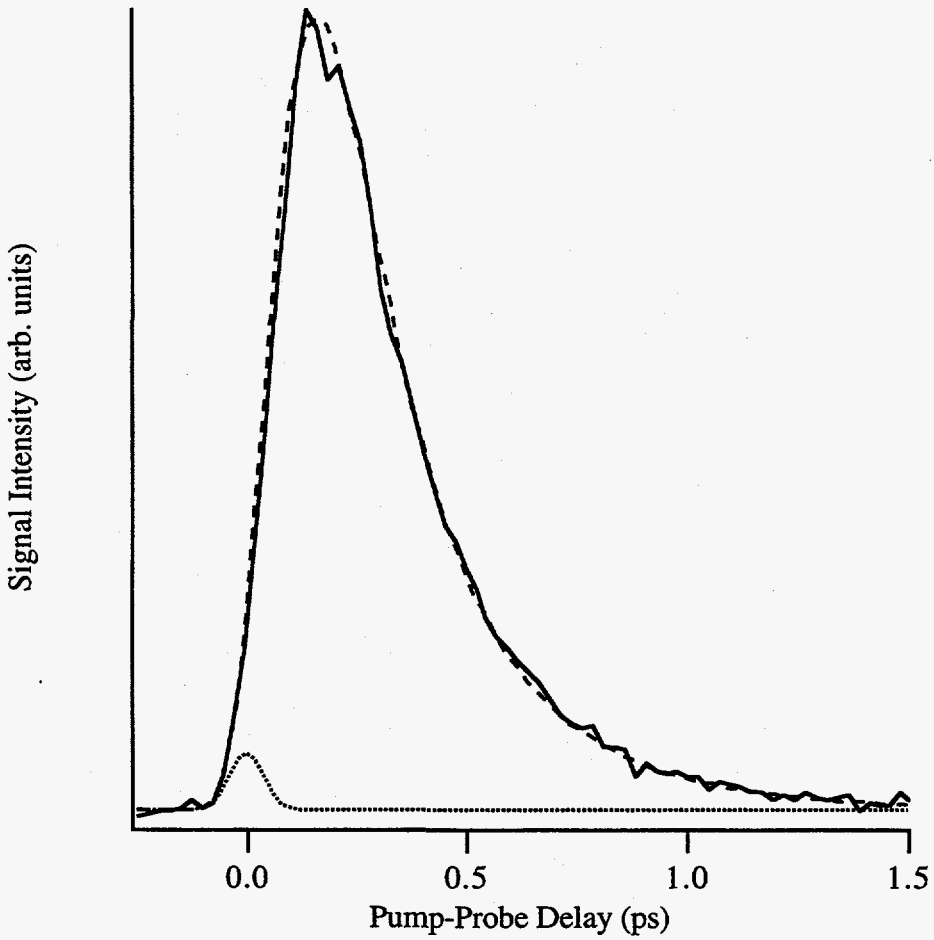

Fig 4.16. Fit of the J diffusion model (dashed line) to the experimental (solid line) RIPS spectrum of CO_2 liquid at a density of 392 amagat. The simulation has $\gamma_{JD} = 7.14$ ps^{-1}, was smoothed by the pump and probe pulse widths (60 fs), and includes a Gaussian component (100 fs FWHM, dotted line) to account for the instantaneous electronic response.

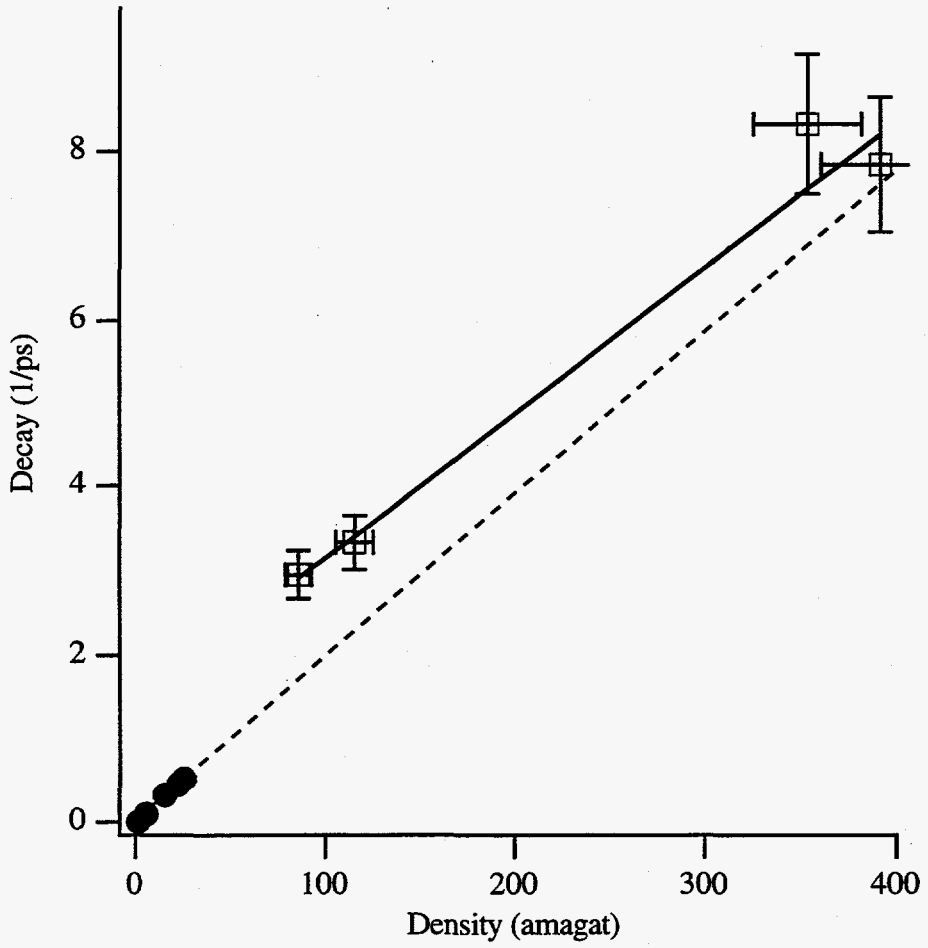

Fig. 4.17. A straight line plot of the J diffusion decay rate versus density (squares) gives a slope of 1.74 $x10^{-2}$ ps^{-1}/amagat. Also shown is the extrapolated line (dotted) from the fit of the low pressure data (circles) to the phenomenological decay model, which gives a slope of 1.94 x 10^{-2} ps^{-1}/amagat.

Appendix

Computer Programs for Simulating Molecular Response

```
/* RCS0.C  main program for calculation of  Raman Induced Polarization Spectroscopy
response */

#include <stdio.h>
#include <math.h>
#include <ctype.h>
#include <conio.h>
#include "rcs.h"

float gamma;            /*decay constant= gamma*exp(-coef*J) (ps-1),
                                    modified 2-19-93*/
float coef;
extern float gammaq;
float gammaq;           /*decay constant for potato (ps-1),
                                    modified 9-12-94 */
float  brot;            /* rotational constant (cm-1) */
float  drot;            /* centrifugal constant (cm-1) */
float kt;               /* temperature (cm-1) */
int even;               /* 2 for homonuclear, else 1 */
float spin;             /* nuclear spin for homonuclear molecules */
float parity0, parity1; /*stat. weight of J-levels */
int maxj;               /* maximum J excited */
int jo;                 /* lowest possible j */
int espin;              /* electronic spin */
float part_fxn;         /* partition function at kt */
float tstep;            /* time step size in data file */
float *rcsdat;

FILE *fpar;

void main(void)
{
        char c;
    char str[80];

        if (!(fpar=fopen("rcs.par","r")))
                fpar = stdin;

        printf("\n\n");
        printf("--- RCS program generating 'potato' for linear mol ---\n");
        printf("-----The output is the response fxn to delta pulse pump -----\n");
        printf("-----       use 'smooth,g' option in <finesse>          -----\n");
        printf("-----         to get finite pulse response            -----\n");
        printf("\n\n\n");
```

```
        printf("Please enter the rotational const, temperature (cm-1): ");
        fgets(str,79,fpar);
        sscanf(str,"%f%f", &brot, &kt);
        printf("%f %.2f",brot,kt);
        printf("\nPlease enter the centrifugal const(cm-1): ");
        fgets(str,79,fpar);
        sscanf(str,"%f", &drot);
        printf("%.4e",drot);

printf("\nEnter [g, c] {decay const.= g*exp(-c*J)(ps-1)}: ");
fgets(str,79,fpar);
        sscanf(str,"%f%f", &gamma, &coef);
        printf("%.4f\t%.4f\t",gamma, coef);

        maxj = (int)(sqrt(10.*kt/brot));
        fgets(str,79,fpar); /* read out the decay for potato */
        sscanf(str,"%f", &gammaq);
        printf("%.4f",gammaq);

        spin = 0.;
        jo = 0;
        printf("\nIs the molecule homonulear? ");
        fgets(str,79,fpar);
        while((c=tolower(str[0]))!='y' && c!='n');
        printf("%c",c);
        if (c=='y') {
                even = 2;
                printf("\nEnter the nuclear spin please: ");
                fgets(str,79,fpar);
                sscanf(str,"%f", &spin);
                printf("%.1f",spin);
                if ((int)(spin) != spin) {
                        parity0 = spin;
                        parity1 = spin + 1;
                        }
                else {
                        parity1 = spin;
                        parity0 = spin + 1;
                        }
                printf("\nEnter the lowest possible J: ");
                fgets(str,79,fpar);
                sscanf(str,"%d", &jo);
                printf("%d", jo);
                espin = 0;
                if (jo!=0) {
                        printf("\nEnter the electronic spin: ");
                        sscanf(str,"%d", &espin);
                        printf("%d", espin);
                        }
                }
        else even = 1;
        printf("\nDo you want to calculate the derivative of RCS as well?");
        if ((c=getche()) =='y' || c == 'Y')
```

```
                delta_kd();
        else
                delta_k0();
        fclose(fpar);
}

/* RCS1  functions for the claculation of the Raman induced rotational coherence
        spectrum of see J.P.Heritage et.al, Phys. Rev. Lett. V34, (1299)1975        */

#include <stdio.h>
#include <math.h>

#include "rcs.h"
float gm(int j);

float cj(int j);
/* 3 J coefficient for j to j transition */
float cj(int j)
{
        double x;

        x = j*(j+1.)*(2.*j+1.)/((2.0*j+3) *(2*j-1.))*Rpopul(j);

        return(x);
}


/* function to calulate the rotational population probability of level J
at temperature T (kT in units of wavenumber), one M level only */

float partition_fxn(void)
{
        int j, spn;
        float x;

        x = 0;
        spn = espin;
        for(espin=-spn; espin<=spn; espin++) {
                for (j=jo; j<maxj; j+=even)
                        x += Rpopul(j)*(2.*j+1);
                }
        if (spin != 0) {
                x *= parity0;
                for(espin=-spn; espin<=spn; espin++) {
                        for (j=jo+1; j<maxj; j+=even)
                                x += (parity1 * Rpopul(j)*(2.*j+1));
                        }
                }

        espin = spn;
        return (x);
}
```

```
double Rpopul(int j)
{
        return (exp(-energyj(j)/kt));
}

/* function to calculate the Raman coupling coeficient Tj
        J.P.Heritage et.al, Phys. Rev. Lett. V34, (1299)1975 */

double Tj(int j)
{
        double x;

        x =(j+2.)*(j+1.)/(2.0*j+3) * (Rpopul(j) - Rpopul(j+2));

        return(x);
}

/* function to calculate the f(t0, t) where
        f(t0, t) = SUM {sin[wj*(t0-t)]*Tj(j)}, j=0,maxj,even;
        t0 is used for the upper bound of integral in qromb()
*/
float rcs_sum(float t0, float t, int maxj)
{
        int j, spn;
        float x;

        x = 0;
        spn = espin;
        for(espin=-spn; espin<=spn; espin++) {
                for (j=jo; j<maxj; j+=even)
                        x += Tj(j) * exp(-gm(j)*(t0 - t))*(sin(omegaj(j)*(t0 - t))+
                                gm(j)* cos(omegaj(j)*(t0 - t))/omegaj(j));
                }
        if (spin != 0) {
                x *= parity0;
                for(espin=-spn; espin<=spn; espin++) {
                        for (j=jo+1; j<maxj; j+=even)
                                x += parity1 * Tj(j) * exp(-gm(j)*(t0 - t)) *
                                (sin(omegaj(j)*(t0 - t)) +
                                        gm(j)*cos(omegaj(j)*(t0 - t))/omegaj(j));
                           /* modified to include cos decay 9-7-94
                                remove the cos term for sin decay only */
                        }
                }

        espin = spn;
        return (x);
}

/* energy difference between J+2 and J */
#define PI2C 0.1883655                  /* 4PI*Speed of light (cm/ps) */
float omegaj(int j)
```

```
{
        return(PI2C*(energyj(j+2) - energyj(j)));

}

/* program designed for o2 */
/* constants from Astro. Phys. J., v108, p167, 1948 H.D.babcock, L. Herzberg */
float energyj(int j)
{
        float j2;
        float wo, fspin;
        float lambda=1.984;             /*added by mike 3-15-93*/

        j2 = j*(j+1.0);
        wo = brot*j2 - drot*j2*j2;
        if (espin==0)
                return(wo);
        else if (espin==-1) { /* for o2 only */
                fspin = (2.*j-1)*brot;
                fspin = wo - fspin-lambda+sqrt(fspin*fspin+lambda*lambda
                                -2*lambda*brot)+ 0.00837*j;
                }
        else {
                fspin = (2.*j+3)*brot;
                fspin = wo+fspin-lambda-sqrt(fspin*fspin+lambda*lambda-
2*lambda*brot)
                        -0.00837*(j+1.);
                }
        return(fspin);
}
#undef PI2C

/* Delta_K0  function to calculate the nonlinear polarizaiont induced
   by transient Raman excitation.  Data is saved in file "rcs.dat".
   Program calculates the response fxn, smooth it with a pulse width using
   finesse.exe to see the change of shape w.r.t pulse duration */

#include <stdio.h>
#include <math.h>
#include <conio.h>
#include <ctype.h>
#include <stdlib.h>
#include <string.h>
#include <dos.h>
#include "rcs.h"

extern float gammaq;
extern float *rcsdat;
extern FILE *fpar;

void smooth_with_gaussian(float *smt_data, float *rawdata,
                float pts, int ndat);
float cj(int j);
```

```
float gm(int j);
#define MINT -1
#define MAXT 20

void delta_k0(void)
{
        float dk, t, tstep, tmax, tjump, tjumpsize, twidth;
        float  x, y, z, dkc, p2, wj, temp, cs;
        float taup,taud,*rcsdat,*rcssmt;

        char c, *str, *smtstr;

        FILE *fp, *fppop, *fpsmt;
        int spn, smtyes;
        int j, tdir=1, savepop, count=0;

        if (!(fp=fopen("rcs.dat", "w"))) {
                printf("Error open rcs.dat for write");
                exit(1);
                }
        if(!(str = (char *)calloc(120, sizeof(char)))) {
                printf("Out of memory for str");
                exit(1);
                }

        t = MINT;
        tmax = MAXT;
        printf ("\nTmin = %f, Tmax = %f.  Any change (y/n)? ", t, tmax);
        while ((c=tolower(getch())) !='y' && c != 'n');
        tjumpsize = 0.;
        twidth = tmax;
        if (c == 'y') {
                printf ("\nEnter new Tmin, Tmax please: ");
                scanf("%f%f", &t, &tmax);
                printf ("\nEnter the Tjump Twidth please: ");
                scanf("%f%f", &tjumpsize, &twidth);
                }
        if (t>tmax) {
                temp = t;
                t = tmax;
                tmax = temp;
                }
        printf ("\nSave the population and Tj? ");
        while ((c=tolower(getch())) !='y' && c != 'n');
        if (c =='y') {
                if(!(fppop = fopen("popul.dat","w"))) {
                        printf("\nFailed to open poplu.dat");
                        exit(1);
                        }
                fprintf(fppop, "  J   E(J)   pop                  Tj\n");
                fprintf(fppop, "#-----------------------------#\n");
                savepop = 1;
                }
```

```
else savepop = 0;

tstep = .01;
printf ("\nStepsize = %.3fps. Any change (y/n)?", tstep);
while ((c=tolower(getch())) !='y' && c != 'n');
if (c=='y') {
        printf("\nPlease enter the new stepsize in ps: ");
        scanf("%f",&tstep);
        if (tstep<0) {
                tdir = -1;
                tjumpsize *= -1;
                twidth *= -1;
                temp = t;
                t = tmax;
                tmax = temp;
                }
        }


printf("\nCalculation working ---\n");

spn = espin;
tjump = t+twidth;
part_fxn = partition_fxn();     /* old /1000.*/
cs = kt/5.31;                           /* normalization coef. for P2,
                                                5.31=H-bar in (ps/cm) */


fprintf(fp, "B=%f, D=%e, kT=%f\ngamma = %f, coef = %f\n",
                brot, drot, kt, gamma, coef);
fprintf(fp,"  gamma_q = %f\n", gammaq);
fprintf(fp, "   partition function (temp) = %20.17f\n", part_fxn);
fprintf(fp, "   t      ki(t)    p2(cos(t))  g*ki_cos  ki_dj0\n");
fprintf(fp, "#-------------------------------------------------#\n");


while (tdir*t < tdir*tmax) {
        count++;
        if (t<-1.e-10) {
                if (smtyes) rcsdat[count] = 0.;
                fprintf(fp,"%f\t%f\t%f\t%f\t%f\n", t, 0., 0.25, 0., 0.);
                }
        else {
          dk = 0.;
          dkc = 0;
          p2 = 0;
          for (j=jo; j<maxj+jo; j+=even) {          /* even J levels */
                for(espin=-spn; espin<=spn; espin++) {
                  wj = omegaj(j);
                  temp = gm(j);
/* rcs */                       x = exp(-temp*t)*Tj(j)*cs*
/*DJ!=0 */                  (sin(wj*t)+ temp/wj * cos(wj*t))
/* DJ=0 */       + gammaq * exp(-gammaq*t)*cj(j)*cc;
```

```
/* P(2) */          y = exp(-temp*t)* cos(wj*t)
                                *(Rpopul(j)+Rpopul(j+2))*
                                        1.5*(j+2)*(j+1)/(2*j+3)*cc
                                        +exp(-gammaq*t)*cj(j)*cc;
                        z = exp(-temp*t)*Tj(j)*cs*temp/wj * cos(wj*t);

                        /* modified to include cos decay 9-7-94, old one was
                        x = Tj(j)*exp(-a*wj*wj-gm(j)*t)*sin(wj*(t-gm(j)*2*a));
                        */

                        dk += x;
                        p2 += y;
                        dkc+= z;
                        if(savepop&&count<2) {
                                fprintf(fppop, "%d\t%8.5f\t%8.5f\t%8.5f\n",
                                j,energyj(j),(2*j+1)*Rpopul(j)/part_fxn,Tj(j));
                                }
                        }
                }
        if (spin != 0) {
                dk *= parity0;  /* Mult. by nuc. spin degen. of even levels */
                p2 *= parity0;
                dkc*= parity0;
                for(espin=-spn; espin<=spn; espin++) {
                        for (j=jo+1; j<maxj+jo; j+=even) {  /* odd J levels */
                                wj = omegaj(j);
                                temp = gm(j);
/* rcs */                       x = exp(-temp*t)*Tj(j)*cs*
/*DJ!=0 */              (sin(wj*t)+ temp/wj * cos(wj*t))
/* DJ=0 */               + gammaq * exp(-gammaq*t)*cj(j)*cc;
/* P(2) */              y = exp(-temp*t)* cos(wj*t)
                                *(Rpopul(j)+Rpopul(j+2))*
                                        1.5*(j+2)*(j+1)/(2*j+3)*cc
                                        +exp(-gammaq*t)*cj(j)*cc;
                                z = exp(-temp*t)*Tj(j)*cs*temp/wj * cos(wj*t);

                        /* modified to include cos decay 9-7-94 */
                    /*  x = Tj(j)*exp(-a*wj*wj)*sin(wj*t)*parity1; */
                                dk += parity1*x;
                                p2 += parity1*y;
                                dkc+= parity1*z;
                        if(savepop&&count<2) {
                                fprintf(fppop, "%d\t%8.5f\t%8.5f\t%8.5f\n",
                                j,energyj(j),(2*j+1)*Rpopul(j)/part_fxn,Tj(j));
                                }
                                }
                        }
                }
        fprintf(fp,"%f\t%f\t%f\t%f\t%f\n", t, dk/part_fxn,p2/part_fxn,
                dkc/part_fxn,0.25*gammaq*exp(-gammaq*t));
        if (smtyes)
                rcsdat[count] = dk/part_fxn;
        }
```

```
        printf("          \r%f", t);
        t += tstep;
        if (tdir*t>=tdir*tjump) {
                t+= tjumpsize-tstep;
                tjump = t+twidth;
                }
}

fclose(fp);
if(savepop)
        fclose(fppop);

if (smtyes) {
        if(!(rcssmt = (float *)calloc(count, sizeof(float)))) {
                printf("Out of memory for rcssmt");
                exit(1);
                }
        if(!(smtstr = (char *)calloc(20, sizeof(char)))) {
                printf("Out of memory for str");
                exit(1);
                }
        if (!(fpsmt=fopen("rcs.smt", "w"))) {
                printf("Error open rcs.smt for write");
                exit(1);
                }
        if (!(fp=fopen("rcs.dat", "r"))) {
                printf("Error open rcs.dat for read");
                exit(1);
                }
        smooth_with_gaussian(rcssmt, rcsdat, tdir*taup/tstep, count);
        smooth_with_gaussian(rcsdat, rcssmt, tdir*taud/tstep, count);

/* remove the file header from fp to fpsmt */
        do {
                if (fgets(str, 80, fp) == NULL) {
                        printf("\nUnexpected EOF reached in rcs.dat\n");
                        exit(1);
                }
        fputs(str, fpsmt);
        } while (!strstr(str,"---#"));

        j=0;
        while (fgets(str, 120, fp) != NULL) {
                sprintf(smtstr,"%8.5f\n",rcsdat[j]);
                str[strlen(str)-1] = '\t';
                strcat(str,smtstr);
                fputs(str, fpsmt);
                j++;
                }

        free(smtstr);
        free(rcssmt);
```

```
                free(rcsdat);
                fclose(fp);
                fclose(fpsmt);
                system("del rcs.dat");
                system("ren rcs.smt rcs.dat");
                }
        free(str);
        return;
}

/* function to calculate the decay constant assuming energy-gap law */
float gm(int j)
{
        if (coef<1.0e-10 && coef >-1.0e-10)
                return(gamma);
        else
                return((float)(gamma*exp(-(double)coef*(double)j)));
}

% MATLAB Program "mkjdiff"
% calculates P2 orientational corr function using j
% diffusion model
% dt is in ps
% rotational constants B, D are in wavenumbers, as is kT
% c = speed of light in cm/ps


function mkjdiff();

tau = input('Enter decay time in ps:  ');
n = input('Enter number of steps:  ');
dt = input('Enter step size in ps:  ');
t=[0:dt:n*dt];


maxj = 70;
B = 0.3902;
D = 13.5e-8;
kT = 203;
c = 3e-2;

j = [0:2:maxj]';

% Energy of J state

e = B*j.*(j+1)-D*(j.*(j+1)).^2;

% Rotational freq.

w = 4*pi*B*c*(j+1.5);


partfun = sum((2*j+1).*exp(-B*j.*(j+1)./kT));
```

```
weight = (2*j+1).*exp(-e/kT);
% calc free rotor autocorr. function
for i=1:n+1
  gfr(i) = sum(0.5*(3*(cos(w*t(i))).^2-1).*(weight/partfun));
end
gfr = gfr/gfr(1);
% calc derivative of free rotor autocorr. function
for i=1:n+1
  dgfr(i) = sum(-3*cos(w*t(i)).*sin(w*t(i)).*w.*weight/partfun);
end
% 2nd deriv. of a.c. function
for i=1:n
 ddgfr(i) = sum(-3*w.*w.*(2*((cos(w*t(i))).^2)-1).*weight/partfun);
end
% free rotor memory function
kfr(1) = -ddgfr(1);
kfr(2) = -(2/dt)*dgfr(2)-gfr(2)*kfr(1);
for i=3:n+1

        temp = -2*gfr(i-1:-1:2)*kfr(2:i-1)';
  kfr(i) = -(2/dt)*dgfr(i)-gfr(i)*kfr(1)+temp;
end
% J diffusion memory function
 k = kfr.*(exp(-t/tau));

% set g=gfr initailly, so g is correct sized array
g = gfr;
% J diffusion a.c. function and derivative, dg
```

```
g(1) = 1;
g(2) = (1-.25*dt^2*k(2))/(1+.25*dt^2*k(1));

dg(1) = 0;

for i=2:n

    dg(i) = -dg(i-1)+(2/dt)*(g(i)-g(i-1));

        temp2 = g(2:i)*k(i-1:-1:1)';


  g(i+1) = (g(i)+.5*dt*dg(i)-.25*dt^2*k(i+1)-.5*dt^2*temp2)...
                /(1+.25*dt^2*k(1));

end

dg(n+1) = -dg(n)+(2/dt)*(g(n+1)-g(n));

denom = 1+2*dg(1)*dt;
ddg(1) = -k(1);
ddg(2) = -k(2)*denom-(dt/2)*k(1)*dg(2);

for i=3:n+1

        temp3 = 2*k(2:i-1)*dg(i-1:-1:2)';


  ddg(i) = -k(i)*denom-(dt/2)*(temp3-k(1)*dg(i));

end


dgfr(n+1) = [];

% save and plot data

sim1= [t(1:n)', g(1:n)', dg(1:n)', ddg(1:n)'];
sim2 = [t(1:n)', gfr(1:n)',dgfr(1:n)', ddgfr(1:n)'];
sim3 = [t(1:n)', k(1:n)', kfr(1:n)'];

save 'c:\data\rcs\jdiff\jdifg3.dat' sim1 -ascii;
save 'c:\data\rcs\jdiff\jdifgfr3.dat' sim2 -ascii;
save 'c:\data\rcs\jdiff\jdifk3.dat' sim3 -ascii;

plot(t(1:n), gfr(1:n), t(1:n), g(1:n),':')
```